Towards Measuring the Electron Electric Dipole Moment Using Trapped Molecular Ions

by

R.P. Stutz

B.S., University of Kansas, 1998

A thesis submitted to the

Faculty of the Graduate School of the

University of Colorado in partial fulfillment

of the requirements for the degree of

Doctor of Philosophy

Department of Physics

2010

This thesis entitled:
Towards Measuring the Electron Electric Dipole Moment Using Trapped Molecular Ions
written by R.P. Stutz
has been approved for the Department of Physics

Eric Cornell

Jun Ye

Date

The final copy of this thesis has been examined by the signatories, and we find that both the content and the form meet acceptable presentation standards of scholarly work in the above mentioned discipline.

Stutz, R.P. (Ph.D., Physics)

Towards Measuring the Electron Electric Dipole Moment Using Trapped Molecular Ions

Thesis directed by Prof. Eric Cornell

Permanent electric dipole moments have been the subject of experimental investigation for the past sixty years, as they entail the breaking of fundamental symmetries and provide a sensitive probe for physics beyond the Standard Model. This thesis describes an experiment aimed at measuring the electron electric dipole moment (eEDM) using trapped molecular ions. The $^3\Delta_1$ level of certain diatomic ions are desirable in eEDM searches due to their high polarizability, large eEDM enhancement factor, and relative insensitivity to magnetic fields. Ions allow for simple trapping and long interrogation times, but require a time-varying electric bias field in order to probe the eEDM.

I will discuss the criteria for molecular ions in our experiment and our current candidates. A laser-ablation supersonic-expansion beam source has been developed to create and cool molecular ions. These ions have been loaded into a linear rf Paul trap and alternative photoionization methods for state-selective ion creation have been tested. Various experimental methods for performing the necessary spin resonance measurement are discussed. Sources of both decoherence and systematic errors have been identified and estimated. The experiment described in this thesis should be capable of a factor of 30 improvement on the current limit of the eEDM.

Dedication

To my brothers, Christopher and Curtis.

Acknowledgements

I would first like to thank my advisor, Eric Cornell. His enthusiasm for physics was contagious and he always seemed to have the most powerful way to view any physics problem in front of him. Unfortunately, Eric was dealt a large dose of adversity during my studies here. Abraham Lincoln once said,"Nearly all men can stand adversity, but if you want to test a man's character, give him power." Well, I've also observed Eric with power. In fact, I can think of few better ways to observe someone having power than to be their graduate student. In dealing with both adversity and power, Eric's true character was revealed. I found him to not only be an amazing scientist, but also a thoroughly decent human being. I couldn't have asked for a better advisor.

Carl Wiemen and Debbie Jin have both been exceedingly helpful during the course of my studies. Carl stepped into the role of advisor during those difficult days of 2004. His advice on topics from experimental techniques to improving the way I presented work was always useful. Debbie had a tendency to always ask the right question that kept us thinking about the important issues in our experiment.

John Bohn and his graduate student Ed Meyer provided a great deal of theory support. Their insights were crucial in finding credible molecular ion candidates for our experiment. They performed many calculations and a lot of the ideas of how the experiment will ultimately be performed came from discussions with them. The group from St. Petersburg, Anatoly Titov, Mikhail Kozlov, Alexander Petrov and Timur Iseav, also did many calculations that helped guide our way. Also, many thanks to them for showing me St. Petersburg.

The community of scientists within JILA is truly impressive, and no matter what issue came

up an expert was always down the hall. Jun Ye has been involved with the experiment from the beginning, and has given much helpful advice on everything from lasers to molecular beams. I would also like to thank Jun and his group for allowing us to win so many of those JILA Cup challenges, although it is with great shame that I will likely be leaving JILA without the cup being possessed by its rightful owners, the Cornell and Jin groups. I would like to thank Carl Lineberger, David Nesbitt and their students for teaching us so much about molecular spectroscopy and molecular beams. Heather Lewandowski, a.k.a. Coach Lew, and her group have been a great resource on all things molecules as well.

Thanks to Robert Field for teaching us everything we know about autoionization of Rydberg states. He has been very gracious in providing us advice and his trips to Boulder were always greatly anticipated.

I've had the great pleasure of working with so many talented graduate students and postdocs during my time at JILA. Thanks to Aaron Leanhardt who helped with a great deal of the work in this thesis. He has an amazing drive to do physics and his tireless work rate and great gifts as a scientist were inspiring to observe. I'd also like to thank him for road trips to Kansas to watch opening day baseball and other such distractions. Laura Sinclair was here from almost the very beginning of the experiment and has been a great lab mate and friend. Patrick Maletinsky visited JILA for only a short time, but he made a big impact and was crucial in the first ion trapping experiments. Herbert Loser visited us on a sabbatical and was a great help in making our LabView code much more professional and also with photoionization experiments. Huanqian Loh has been an absolute joy to work with, a great young scientist and a really nice person to be around. Matthew Grau has made an impact right from the start and has a great future ahead of him. Tyler Yahn has been an undergraduate researcher on the experiment and a great help.

I'd like to thank all the members of the "tri-group" for the helpful suggestions throughout the years and for some great friendships. In particular, I would like to thank Josh Zirbel and Scott Papp for being my surrogate lab mates during my first year. It was invaluable having them there to bounce ideas off of or to ask the truly stupid questions you'd rather not take to your advisor as

a first-year student. Thanks to all of the students and post-docs who I shared lab space with in B224/228, especially my roommate Giacomo Lamporesi and my good friend Shih Kuang "Zeke" Tung. Thanks to Juan Pino, Jason Stewart, and John Gaebler for useful discussions, most of which were happily not about physics.

The amount of support we receive as graduate students in JILA is exceptional. Thanks to all the folks in the machine shops, electronic shops, computing staff, supply office, and the office staff. Special thanks to Hans Green, Todd Asnicar, Blaine Horner, Terry Brown, and Carl Sauer for producing so much of the experimental apparatus described here. Also, Pam Leland was always amazing in helping make things run smoothly.

I would have never made it to JILA without the help of many people along the way. Kenneth Dinndorf and Harold Miller were my supervisors at Kirtland AFB and taught me all about lasers and optics. They were also great mentors and friends and always encouraged me to pursue graduate school. David Besson, my undergraduate advisor at KU, taught me a great deal about how experimental science is done. He was a great mentor and friend. Thanks to the "fab five physics majors" at KU who I learned so much from during my undergraduate days while doing homework, performing research, and enjoying life with them.

I couldn't have done this without the love and support from all of my family. My mother and father have always supported me, even when I decided to do crazy things like join the Air Force or even crazier things like go to physics graduate school. I dedicate this thesis to my brothers, who were always there for me and who taught me so much about life.

My greatest accomplishment during my graduate school career was convincing my loving and lovely wife Oraya to marry me. She has been a constant source of support throughout the writing of this thesis. I can't wait for life's next adventure knowing my best friend will be by my side.

Contents

Chapter

Tables

Table

Figures

Figure

Chapter 1

Introduction [1]

1.1 Motivation for Electric Dipole Moment Searches

At first glance, the electron appears to be a trivial physical system to study. An elementary particle in modern physics, it has only a handful of measureable properties, including mass, charge, and spin. Perhaps the most interesting property, due to its historical impact on modern physics, is the magnetic g-factor, g_e. The prediction of $g_e = 2$ was a major triumph of the Dirac equation, and thus aided in the development of relativistic quantum mechanics. In order to account for slight deviations of g_e from 2, QED is needed. Fig. 1.1 shows a one-loop correction in QED to g_e, where a virtual photon interacts with the electron, adding a factor of α/π to the electrons g-factor. The current measurement of the electron's magnetic moment is accurate to 14 digits [7] and agrees with theory out to eighth-order corrections [8]. At this level of precision, hadronic and weak corrections must be included. In fact the value of g_e will be influenced by the properties of all particles that interact with the electron. This is true of not only g_e, but also of other properties of the electron, including its mass and charge. This illustrates how a precision measurement of the electron can in principle give information about less well understood particles, for instance the Higgs Boson. In practice, measurements of g_e are not very sensitive to exotic massive particles, due to the small electron mass. For this reason, measurements of the muon g-factor can offer better constraints on exotic particle physics [9], even though the accuracy of these measurements are far worse than similar measurements on the electron. Extracting information from these measurements is difficult since the Standard Model hadronic corrections are uncertain [10].

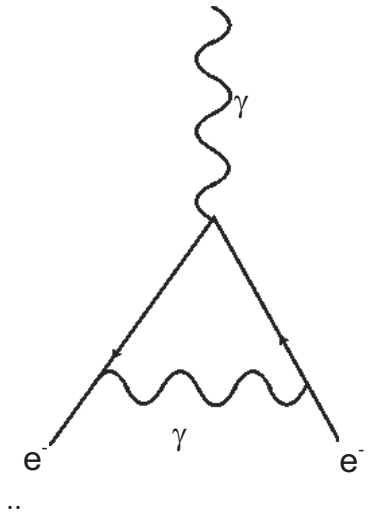

Figure 1.1: One-loop diagram that leads to a correction of the electron g-factor. The electron interacts with a photon (γ) from an external field as well as a "virtual" photon.

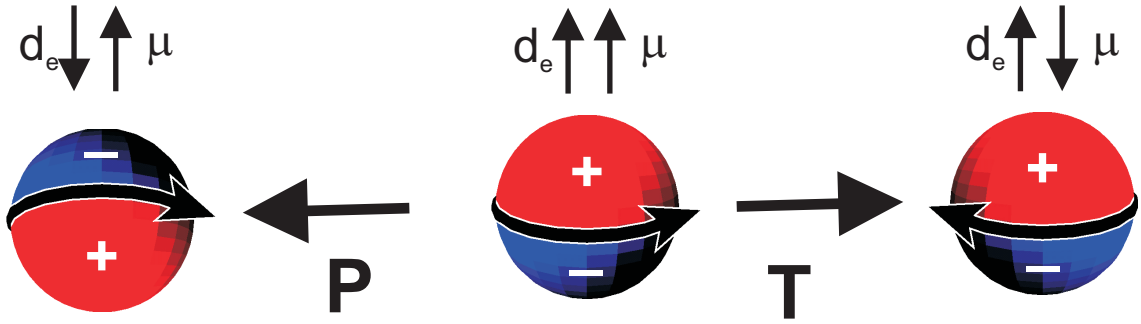

Figure 1.2: If an electron EDM exists, the orientation between the electron's electric (d_e) and magnetic (μ) dipole moments will change under a parity (P) or time-reversal (T) transformation.

Measurements of the electron electric dipole moment (eEDM) are a sensitive probe to new physics as it violates time-reversal (T) and parity (P) symmetries. This is seen by first assuming the eEDM lies along the same axis as the electron's magnetic dipole moment, an assumption that will be discussed below. The magnetic moment is T-odd and P-even, while an electric moment would be T-even and P-odd. This means that parity or time-reversal transformation would change the relative orientation between the electron's magnetic and electric moments and an inversion of space or reversal of time would be observable by measuring the orientation of electron moments. This is illustrated schematically in Fig. 1.2. The P and T violation of an electron EDM implies CP violation if the widely held CPT conservation theorem is assumed correct.

CP violation has been experimentally observed in both Kaons [11] and B mesons [12, 13]. The observed CP violation is accounted for in the Standard Model through a CP violating phase in the Kobayashi-Maskawa (KM) quark-mixing matrix. This leads to an electron EDM through Feynman diagrams that include electroweak couplings to quarks, but at higher orders of perturbation than for quark systems. Hoogeveen [14] attempted to estimate d_e from three-loop diagrams, an example of which is shown in Fig. 1.3 and obtained a value of $\sim 10^{-38}$ e cm. It was later shown that diagrams even at the three-loop level will cancel [3] and Khriplovich and Lamoreaux estimate the Standard Model electron EDM as $< 10^{-40}$ e cm [15].

Another possible source of CP violation is in the strong nuclear interaction where another

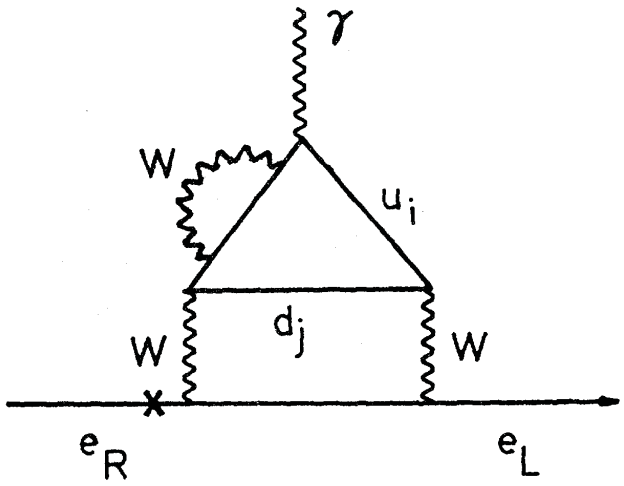

Figure 1.3: Feynman diagram from Ref. [2] for a three-loop contribution to the eEDM. The sum of three-loop diagrams cancels to zero [3] and four-loop diagrams are needed to produce a non-zero eEDM in the Standard Model.

CP violating phase $\Theta_{\rm QCD}$ is found. This phase would give rise to a very large neutron EDM given its "natural" size $O(1)$. The current experimental limit on the neutron EDM requires $\Theta_{\rm QCD}$ to be $O(10^{-10})$ [16], giving rise to the strong CP problem in particle physics. This source of CP violation is unimportant when determining the size of the electron EDM.

Observations of neutrino oscillations and their implication of neutrino masses gives rise to a third possible mechanism for an electron EDM in the Standard Model. Massive neutrinos give rise to a lepton mixing matrix analogous to the KM matrix, with the possibility of CP violating phases. Contributions to an electron EDM from this source tend to be smaller than for the KM mechanism, although an estimates of $d_e \lesssim 10^{-33}$ e cm is found with two "extra" massive neutrinos and fine-tuning of neutrino masses [17].

Many extensions to the Standard Model predict far greater values for the eEDM [2]. This is perhaps not surprising, since a major failing of the Standard Model, that these extensions wish to correct, is the fact that it does not contain enough CP violation to explain the matter-antimatter asymmetry in the Universe. Extensions to the Standard Model predict a value for the eEDM as high as the current experimental limit of 1.6×10^{-27} e cm, many orders of magnitude above the Standard Model background. With the range of theoretical predictions starting at the experimental limit, and Standard Model backgrounds orders of magnitude below this limit, an improved measurement of the eEDM is a tempting goal. This thesis describes an experiment that hopes to achieve a factor of thirty improvement on the experimental upper limit for an eEDM.

1.2 Schiff's Theorem

In general, an electron EDM measurement is made by applying an electric field to an electron and looking for a response. Applying large electric fields to bare electrons results in a rapid acceleration of the electrons out of the experimental apparatus. Using an unpaired electron in a neutral atom or molecule seems problematic. Naively, one would assume that the electrons inside the atom would just arrange themselves such that the average electric field on any charged particle in the atom would time average to zero, as the neutral atom is not accelerated by the external

field. This principle is known as Schiff's theorem [18, 19] and is largely the reason why the first experiments specifically designed to measure a T-violating EDM were made on neutrons [20]. A similar thing occurs when an external electric field is applied to an ion in an rf Paul trap, moving the ion to a new position where the time-averaged electric field is zero.

Loopholes in Schiff's theorem include finite-size effects of the nucleus and relativistic corrections. The latter tends to dominate for electron EDM measurements and is discussed in Ref. [21]. The time-averaged electric field $\langle \boldsymbol{\mathcal{E}} \rangle$ on an atomic electron, even when relativistic effects are taken into account, is zero. However, due to length contraction, the time-averaged value of $\mathbf{d_e} \cdot \boldsymbol{\mathcal{E}}$ will in general not equal zero. The interaction energy with an electric dipole moving at a velocity $c\boldsymbol{\beta}$, as observed in the laboratory frame, will be

$$W_e = -\mathbf{d_e} \cdot \left(\boldsymbol{\mathcal{E}} - \frac{\gamma}{1+\gamma} \boldsymbol{\beta} \cdot \boldsymbol{\mathcal{E}} \boldsymbol{\beta} \right), \tag{1.1}$$

with $\gamma = (1\text{-}\beta^2)^{1/2}$. Ref. [21] shows it is essentially the second term in Eq. 1.1 that gives rise to an interaction energy between an atomic or molecular valence electron EDM and an external electric field. Despite the average electric field seen by an atomic electron being zero, it is customary to define an effective electric field, $\mathcal{E}_{\text{eff}}$, such that $\mathrm{E_{edm}} = -\mathbf{d_e} \cdot \mathcal{E}_{\text{eff}}$.

1.3 Direction of d_e

Earlier, the assumption was made that the eEDM lies along the same axis as the electron's magnetic dipole moment. To test this, let us assume that the eEDM is not at a fixed angle relative to the electron's spin axis. If that were the case, an extra quantum number would be required to describe the state of an electron and more than the experimentally observed two electrons would be allowed in a 1S atomic orbital. Clearly, an eEDM must have a fixed orientation with respect to the electron's spin axis.

It is less clear if $d_{e\perp}$, a component of d_e perpendicular to the spin axis, is allowed. Certainly, a fundamental spin-1/2 particle has only one vector, the spin axis, available to orient the particle. The situation is less clear if the electron is allowed internal structure. An experiment sensitive to

a $d_{e\perp}$ is beyond the imagination of this author, and certainly our experiment will only be sensitive to a d_e component parallel or anti-parallel to the spin axis. If our experiment yields a non-zero d_e the symmetry breaking arguments made above will therefore be valid.

1.4 Overview of Ongoing Experimental Work

For 20 years the most stringent limits on the eEDM have been the atomic-beam experiments of Commins' group [22, 23, 24]. That work set a standard against which one can compare ongoing and proposed experiments to improve the limit. Here is a brief survey of ongoing experiments of which we are aware.

For evaluating the sensitivity of an eEDM experiment the key figure-of-merit is $\mathcal{E}_{\rm eff}\tau\sqrt{N}$, where $\mathcal{E}_{\rm eff}$ is the effective electric field on any unpaired electrons, τ is the coherence time of the resonance, and N is the number of spin-flips that can be counted in some reasonable experimental integration time, for instance one week. We will discuss these three terms in order.

In practice all eEDM experiments involve heavy atoms with unpaired electron spins, and most involve measuring the atomic spin-flip frequency ω_d. An applied laboratory electric field distorts the atomic wavefunction, and the eEDM contribution to the atomic spin-flip frequency ω_d is enhanced by relativistic effects occurring near the high-Z nucleus [25, 26], so that $\omega_d = d_e\mathcal{E}_{\rm eff}$ [27], where the effective electric field $\mathcal{E}_{\rm eff}$ can be many times larger than the laboratory electric field $\mathcal{E}_{\rm lab}$. The enhancement factor is roughly proportional to Z^3 although details of the atomic structure come into play such that the enhancement factors for thallium ($Z = 81$) and cesium ($Z = 55$) are -585 [28] and $+114$ [29], respectively. Practical DC electric fields in a laboratory vacuum are limited by electric breakdown to about 10^5 V/cm. The Commins experiment used a very high-Z atom, thallium, and achieved an $\mathcal{E}_{\rm eff}$ of about 7×10^7 V/cm [22]. There have been proposed a number of experiments in cesium [30, 31, 32] that expect to achieve $\mathcal{E}_{\rm eff}$ of about 10^7 V/cm. A completed experiment by Hunter [33] achieved $\mathcal{E}_{\rm eff} = 4.6\times10^5$ V/cm in Cs by using $\mathcal{E}_{\rm lab} = 4$ kV/cm.

It was pointed out by Sandars [34] that much larger $\mathcal{E}_{\rm eff}$ can be achieved in polar diatomic molecules. In these experiments, the atomic wavefunctions of the high-Z atom are distorted by the

effects of a molecular bond, typically to a much lighter partner atom, rather than by a laboratory electric field. One still applies a laboratory electric field, but it need be only large enough to align the polar molecule in the lab frame. The Hinds group [35] is working with YbF, for which the asymptotic value of $\mathcal{E}_{\text{eff}}$ is 26 GV/cm [35, 36, 37, 38, 39, 40, 41]. DeMille's group [42, 43, 44] uses PbO, with an asymptotic value of $\mathcal{E}_{\text{eff}} \simeq 25$ GV/cm [45, 46, 47]. Shafer-Ray's group [48] has proposed to work with PbF, which has a limiting value of $\mathcal{E}_{\text{eff}} \simeq 29$ GV/cm [49, 50]. The ACME collaboration [51] will use ThO, with $\mathcal{E}_{\text{eff}} \simeq 100$ GV/cm [52]. The Leanhardt group is working with WC, with $\mathcal{E}_{\text{eff}} \simeq 54$ GV/cm [53]. We will discuss candidate molecules for our experiment in Chapter 2.2; we anticipate having an $\mathcal{E}_{\text{eff}}$ of around 25 to 90 GV/cm [52, 54].

After $\mathcal{E}_{\text{eff}}$, the next most important quantity for comparison is the coherence time τ, which determines the linewidth in the spectroscopic measurement of ω_d. In Commins' beams experiment, τ was limited by transit time to 2.4 ms. Future beams experiments may do better with a longer beam line [48], or with a decelerated beam [55]. Groups working in laser-cooled cesium anticipate coherence times of around 1 s, using either a fountain [30] or an optical trap [31, 32]. The PbO experiment has τ limited to 80 μs by spontaneous decay of the metastable electronic level in which they perform their ESR. Coherence in ThO experiment will be limited by the excited-state lifetime to 2 ms [51]. A now discontinued experiment of Hunter [33] achieved $\tau = 15$ ms in a vapor cell with coated walls and a buffer gas. The JILA experiment will work with trapped ions. The mechanisms that will limit the coherence time in our trapped ions are discussed in Chapters 6, 7, and 8. We anticipate a value in the vicinity of 300 ms.

The quantity $\mathcal{E}_{\text{eff}}$ converts a hypothetical value of d_e into a frequency ω_d, and τ sets the experimental linewidth of ω_d. The final component of the overall figure-of-merit is $\sqrt{N}$, which determines the precision with which the resonance line can be determined. Vapor-cell experiments such as those of Hunter or DeMille can achieve very high values of effective N, atomic beams machines are usually somewhat lower, and molecular beams usually lower yet (due to greater multiplicity of thermally occupied states.) Atomic fountains and atomic traps have still lower count rates, but the worst performers in this category are ion traps. The JILA experiment may

trap as few as 100 ions at a time, and observe only 10 transitions in a second.

The discussion above is summarized in Table 1.1. To improve on the experiment of Commins, it is necessary to do significantly better in at least one of the three main components of the figure-of-merit. The various ongoing or proposed eEDM experiments can be sorted into categories according to the component or components in which they represent a potential improvement over the Commins' benchmark. The prospects of large improvements in both τ and $\mathcal{E}_{\text{eff}}$ put JILA's experiment in its own category. This combination means that our resonance linewidth, expressed in units of a potential eEDM shift, will be 10^5 times narrower than was Commins'. Splitting our resonance line by even a factor of 100 could lead to an improved limit on the eEDM. This is an advantage we absolutely must have, because by choosing to work with trapped, charged molecules, we have guaranteed that our count rate, $\dot{N}$, will be far smaller than those of any of the competing experiments.

We note that there are in addition ongoing experiments attempting to measure the eEDM in solid-state systems [56, 57, 58, 59]. These experiments may also realize very high sensitivity, but because they are not strictly speaking spectroscopic measurements, it is not easy to compare them to the other proposals by means of the same figure-of-merit.

1.5 Overview of Thesis

Chapter 2 of this thesis will be a brief walk through of the general spectroscopic idea behind our experiment. The next four chapters are dedicated to experimental progress and the many pieces of technology that needs to come together to make an eEDM measurement with trapped molecular ions possible. Along the way we were faced with many alternative visions of how to make this experiment work, and I will in general discuss some of the alternatives we investigated. Chapter 3 focuses on ion trapping basics. Also included in this chapter is discussion of our first generation ion trap, some experiments done in this first trap, and a brief description of our next generation trap. One challenge of our experiment is efficient read-out of our spin populations after the Ramsey experiment is completed. This will be covered in Chapter 4. The process of creating,

Table 1.1: Figure-of-merit comparison between several recently completed and ongoing eEDM experiments. For ongoing experiments these numbers are subject to change and are often order-of-magnitude estimates.

Group	Species	$\mathcal{E}_{\text{lab}}$ [V/cm]	$\mathcal{E}_{\text{eff}}$ [V/cm]	τ [s]	$\dot{N}$ [s^{-1}]	Refs.
Commins	Tl	1.23×10^5	7×10^7	2.4×10^{-3}	10^9	[22]
Hunter	Cs	4×10^3	4.6×10^5	1.5×10^{-2}		[33]
Gould	Cs	10^5	10^7	1	10^9	[30]
Heinzen	Cs	10^5	10^7	1		[32]
Weiss	Cs	10^5	10^7	1		[31]
DeMille	PbO	10	2.5×10^{10}	8×10^{-5}		[42, 43, 44, 45, 47]
Hinds	YbF	8.3×10^3	1.3×10^{10}	10^{-3}		[35, 60]
Shafer-Ray	PbF	7×10^4	2.9×10^{10}			[48, 49, 50]
ACME	ThO	10^2	10^{11}	2×10^{-3}	10^5	[51, 52]
Leanhardt	WC		5.4×10^{10}	10^{-3}		[53]
JILA	HfF^+, ThF^+, etc.	5	$2 - 8 \times 10^{10}$	0.3	10	

cooling and loading into a trap our molecular ions is covered in Chapter 5. This will include our laser-ablation supersonic-expansion source, a brief discussion of alternative cooling methods, and photoionization techniques for state-selective trap loading. Chapter 6 will discuss some of the issues of performing precision spectroscopy in time-varying, inhomegenous fields. Ion-ion and ion-neutral collisions will be discussed in Chapter 7. Things will get wrapped up in Chapter 8 with conclusions and an estimate of sensitivity to the eEDM.

Chapter 2

Molecular Structure and the Basic Spectroscopic Idea [1]

2.1 Molecular Notation

A final decision as to which molecule we will use has not been made. For reasons discussed below, the main candidates are diatomic molecular ions Mx^+, where M = Hf, Pt, or Th and x = H or F. In the case of molecules such as HfF^+, *ab initio* methods [4, 54] enable us to determine that the $^3\Delta$ state is well described by a set of Hund's case (a) quantum numbers: $J, S, \Sigma, \Lambda, \Omega, M_J, e/f$. Here J is the sum of electronic plus rotational angular momentum, S the total electronic spin angular momentum, Σ the projection of S onto the molecular axis, Λ the projection of L, the electronic orbital angular momentum, onto the molecular axis, and Ω the projection of J onto the molecular axis. In a case (a) $^3\Delta$ molecule $|\Omega|$ can take the values one, two or three. M_J is the projection of J along the quantization axis and the labels e/f specify the parity of the molecular state.

In addition to these quantum numbers, the experiment will be concerned with the nuclear spin quantum number I, the total angular momentum quantum number F, given by the vector sum of J and I, and m_F the projection of F along the quantization axis. Throughout this thesis a total nuclear spin of $I = 1/2$ is assumed, the nuclear spin of fluorine or hydrogen.

2.2 Choosing a Molecule

In selecting a molecular ion for this experiment we have several criteria. First, we want a simple spectrum. Ideally, we would like the supersonic expansion to be able to cool the molecules

into a single internal quantum state so that every trapped molecule could contribute to the contrast of the spectroscopic transition. Failing that, we want to minimize the partition function by using a molecule with a large rotational constant, most likely a diatomic molecule with one of its atoms being relatively light. Small or vanishing nuclear spin is to be preferred, as are atoms with only one abundant isotope. Second, we need to be able to make the molecule. This requirement favors more deeply bound molecules and is the main reason we anticipate working with fluorides rather than hydrides. Third, the molecule should be polarizable with a small applied electric field, i.e. it should have a relatively small Λ-doublet splitting, ω_{ef}, a quantity that is described in Chapter 6.1. Fourth, and most important, the molecule should have unpaired electron spin that experiences a large value of $\mathcal{E}_{\mathrm{eff}}$.

These latter two requirements would appear to be mutually exclusive: a small Λ-doublet splitting requires a large electronic orbital angular momentum, which prohibits good overlap with the nucleus required for a large $\mathcal{E}_{\mathrm{eff}}$. Fortunately, working with two valence electrons in a triplet state allows us to satisfy our needs. One valence electron can carry a large orbital angular momentum making the molecule easily polarizable, while the other can carry zero orbital angular momentum giving it good overlap with the nucleus and generating a large $\mathcal{E}_{\mathrm{eff}}$. This concept was detailed by Bohn and Meyer in Ref. [4] and for the $^3\Delta_1$ state of interest here, the two valence electrons occupy molecular σ and δ orbitals. Calculations [54, 52] indicate that in the $^3\Delta_1$ state of HfH^+ and HfF^+ $\omega_{\mathrm{ef}} \lesssim 2\pi \times 1$ MHz and $\mathcal{E}_{\mathrm{eff}} \approx 30$ GV/cm should be expected. ThF^+ has $\mathcal{E}_{\mathrm{eff}} \approx 90$ GV/cm [52].

2.3 $|\Omega| = 1$ vs. $|\Omega| = 3$

One final valuable feature to look for in a candidate molecule is a small magnetic g-factor, so as to reduce the vulnerability to decoherence and systematic errors arising from magnetic fields. To the extent that spin-orbit mixing does not mix other $|\Omega| = 1$ states into a nominally $^3\Delta_1$ molecular level, it will have a very small magnetic moment, a feature shared by PbF in the $^2\Pi_{1/2}$ state [48]. This is because $\Sigma = -\Lambda/2$, and because the spin g-factor is ~ 2 times the orbital g-factor. Under these conditions, the contributions of the electronic spin and orbital angular momentum to the net

molecular magnetic dipole moment nominally cancel. In HfF^+, the magnetic moment of a stretched magnetic sublevel level of the $^3\Delta_1,\ J = 1$ rotational ground state is about 0.05 μ_B [61]. This is a factor of 20 less than the magnetic moment of ground state atomic cesium. In the $^3\Delta_3$ level, on the other hand, the magnetic moment in the stretched Zeeman level is 4.0 μ_B. The $|\Omega| = 3$ state may nonetheless be of scientific interest. The $^3\Delta_1$ and $^3\Delta_3$ levels have $\mathcal{E}_{\text{eff}}$ equal in magnitude but opposite in sign. If one could accurately measure the science signal, ω_d, in the $^3\Delta_3$ level despite its larger sensitivity to magnetic field background (and despite its shorter spontaneous-decay lifetime), the comparison with the $^3\Delta_1$ result would allow one to reject many systematic errors.

2.4 $|\Omega| = 1,\ J = 1$ Λ-doublet

Since we have not made a final decision as to which molecule we will use, and also because we have yet to measure the hyperfine constants of our candidate molecules, the discussion of level schemes in this section will be qualitative in nature, usually emphasizing general properties shared by all the molecules we are investigating. To simplify the discussion, it will be specialized to discussing spectroscopy within the $J = 1$ rotational manifold of a molecular $^3\Delta_1$ level.

For Hunds' case (a) molecular levels with $|\Lambda| \geq 1$, each rotational level is a Λ-doublet, that is, it consists of two closely spaced levels of opposite parity. We can think of the even (odd) parity level as the symmetric (antisymmetric) superposition of the electronic angular momentum lying predominantly parallel and antiparallel to the molecular axis [Fig. 2.1(a)]. The parity doublet is split by the Λ-doubling energy ω_{ef}. A polar diatomic molecule will have a permanent electric dipole moment, $\vec{d}_{\text{mf}}$, aligned along the internuclear axis $\hat{n}$, but in parity eigenstates, there will be vanishing expectation value $\langle\hat{n}\rangle$ in the lab frame. An applied laboratory electric field, $\mathcal{E}_{\text{rot}}$, will act on d_{mf} to mix the states of good parity. In the limit of $d_{\text{mf}}\mathcal{E}_{\text{rot}} \gg \omega_{\text{ef}}$, energy eigenstates will have nonvanishing $\langle\hat{n}\rangle$ in the lab frame. More to the point, Ω, a signed quantity given by the projection of the electron angular momentum on the molecular axis, $(\vec{L} + \vec{S}) \cdot \hat{n}$, can also have a nonzero expectation value [Fig. 2.1(b)]. Heuristically, it is the large electric fields developed internal to the molecule, along $\hat{n}$, that gives rise to the large value of $\mathcal{E}_{\text{eff}}$ that the electron spin

can experience in polar molecules. In the absence of the Λ-doublet mechanism for polarizing the molecule, a much larger field would be necessary, $d_{\rm mf}\mathcal{E}_{\rm lab} \gg 2B_e$, to mix rotational states with splitting typically twice the rotational constant B_e. For HfF^+, it is estimated $\omega_{\rm ef}$ will be something under $2\pi \times 50$ kHz, whereas B_e will be about $2\pi \times 10$ GHz. For a dipole moment $d_{\rm mf} = 4.3$ D, mixing the Λ-doublet levels will take a field well under 1 V/cm, whereas "brute force" mixing of rotational levels would require around 10 kV/cm. For an experiment on trapped ions, the smaller electric fields are essential.

In the context of their eEDM experiment on the $a^3\Sigma_1$ level in PbO, DeMille and his colleagues have explored in some detail [42, 43, 44] the convenient features of an $|\Omega| = 1,\ J = 1$ state, especially with respect to the suppression of systematic error. Our experiment liberally borrows from those ideas. In a molecule with at least one high-Z atom, $^3\Delta_1$ states will be very similar to the $a^3\Sigma_1$ state of PbO, but with typically smaller values of $\omega_{\rm ef}$ and much smaller values of magnetic g-factor. Singly charged molecules with spin triplet states will necessarily have an odd-Z atom, and thus the unavoidable complication of hyperfine structure, not present in PbO.

In Fig. 2.1 the $^3\Delta_1$, $J = 1$ state with hyperfine splitting due to the fluorine I = 1/2 nucleus is presented. A key feature is the existence of two near-identical pairs of m_F-levels with opposite parity due to Λ-doubling. As seen in Fig. 2.1(b), an external electric field, $\mathcal{E}_{\rm rot}$, mixes these opposite parity states to yield pairs of m_F-levels with opposite sign of $\mathcal{E}_{\rm eff}$ [44] relative to the external field. Fig. 2.1(c) shows the effect of a rotating magnetic bias field, parallel with the electric field, applied to break a degeneracy as described in Chapter 6.4. Note that any two levels connected by arrows in Fig. 2.1(c) transform into each other under time reversal. Time reversal takes $m_F \to -m_F$, $\Omega \to -\Omega$, and $\mathcal{B} \to -\mathcal{B}$, where $\mathcal{B}$ is the magnetic field. If we measure the resonant frequency for the transition indicated by the solid (or dashed) line once before and once after inverting the direction of the magnetic field, time reversal invariance tells us the difference between the two measurements should be zero. In the presence of an eEDM, which violates time-reversal invariance, this energy difference $W^u(\mathcal{B}) - W^u(-\mathcal{B})$ will give $2d_e\mathcal{E}_{\rm eff}$. As well, under the same magnetic field the transitions indicated by the solid and dashed lines should be degenerate, if the magnetic g-factors are identical

for the states involved [62]. With non-zero eEDM the energy difference $W^u - W^l$ also gives $2d_e\mathcal{E}_{\text{eff}}$.

Potential additional shifts, due predominantly to Berry's phase [63], are discussed in Chapter 6 but for now note only that in the absence of new physics (such as a nonzero eEDM) the energy levels of a molecule in time-varying electromagnetic fields obey time-reversal symmetry. Reversing the direction of the electric field rotation while chopping the sign of the magnetic field amounts to cleanly reversing the direction of time, and will leave certain transition energies rigorously unchanged if $d_e = 0$. These are our "science transitions", which we will measure with our highest precision.

2.5 Electronic Level Structure

There are $\sim 10^4$ possible diatomic molecules and one might hope that humanity has knowledge of all their spectra. Alas, that is not the case. It appears that too many people have been at home watching American Idol instead of being in the laboratory late at night taking molecular spectra. In general, diatomic molecules containing atoms as heavy as hafnium, thorium, or platinum have very little known spectra. Diatomic molecular ions are less known still and no previous experimental studies existed for our most promising eEDM molecular ion candidates.

We identified a handful of candidates that might posses low-lying $^3\Delta_1$ states, mostly by looking at known or theoretically predicted spectra of isoelectronic neutral molecules. These molecules typically have low-lying $^1\Sigma$ and $^3\Delta_1$ states with the energy splitting between them predicted to be small enough that either might be the ground state. *ab initio* calculations have been performed [4, 54, 64, 61] that give us a picture of what to expect for states from $0 \sim 14{,}000$ cm^{-1} above the ground state for many of our candidate molecules. Theoretical curves are shown in Fig. 2.2 for the case of HfF^+. There are several states in this energy range of potential interest for state preparation and read-out purposes in our experiment. Spin-orbit mixing between states of identical $|\Omega|$ are enhanced by relativistic effects in the high-Z Hf atom. The b(1) and c(1) states are well-mixed combinations of $^1\Pi_1$,$^3\Pi_1$, and $^3\Sigma_1^-$ states, allowing for electric dipole transitions to and from these states that do not respect spin selection rules. The $^1\Sigma_0$ state, on the other hand,

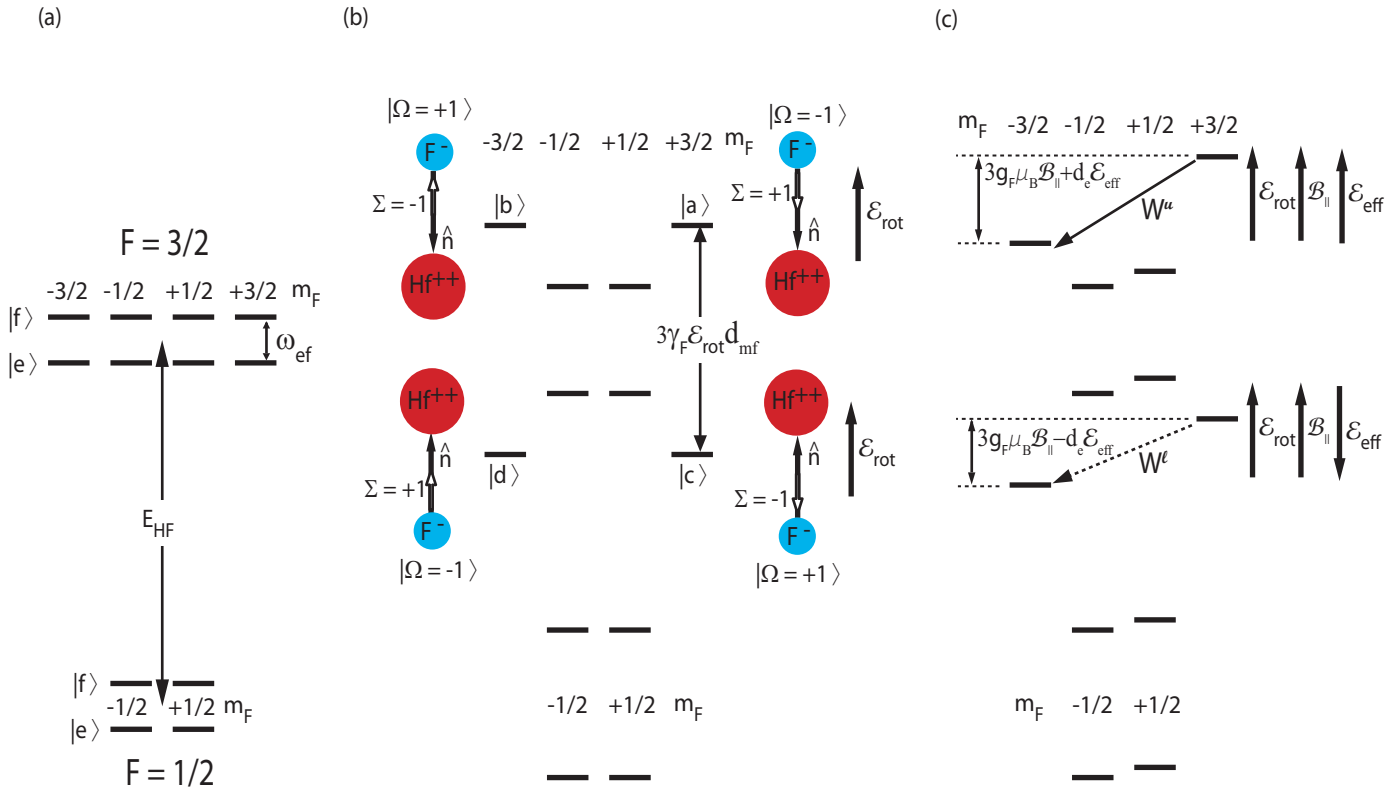

Figure 2.1: Energy levels of HfF^+ in the $^3\Delta_1$, $J = 1$ state including hyperfine structure associated with the fluorine $I = 1/2$ nucleus. Λ and Σ are defined as the projection along the molecular axis of the electronic orbital angular momentum, and spin, respectively. $\Omega = \Lambda + \Sigma$. (a) In zero electric field, the eigenstates of the system are states of good parity, $|e\rangle = (|\Omega = +1\rangle - |\Omega = -1\rangle)/\sqrt{2}$ and $|f\rangle = (|\Omega = +1\rangle + |\Omega = -1\rangle)/\sqrt{2}$, separated by a small Λ-doublet splitting. (b) An electric field, $\mathcal{E}_{\rm rot}$, mixes the parity eigenstates yielding states with well defined Ω. (c) A small magnetic field lifts the degeneracy between states with the same value of $m_F\Omega$. A permanent electron electric dipole moment further breaks this degeneracy, but with opposite sign for the upper (solid arrow) and lower (dotted arrow) transition. Energy splittings not to scale.

has no nearby $|\Omega| = 0$ state with which to mix, and thus Σ and Λ are good quantum numbers. Similarly, the $^3\Delta_1$ state has so little contamination of $^1\Pi_1$ in it that a rough calculation indicates that it is metastable against spontaneous decay, with a lifetime of order 300 ms [4, 54]. Levels in HfF and HfF^+ that are relevant to material throughout this thesis are shown in Fig. 2.3.

We have spent considerable effort attempting to measure the energy of these excited states in HfF^+. This work was complicated by the one difference between our group and molecular spectroscopists; we were not molecular spectroscopists. Laura Sinclair [65] has since measured one electronic transition in HfF^+, an $(\Omega = 1) \leftarrow {}^1\Sigma$ transition, likely to either the b(1) or c(1) state, at 13,000 cm^{-1}. This transition could be used to link the $^1\Sigma$ ground state with the $^3\Delta_1$ state we wish to use for eEDM spectroscopy. Laura and her co-workers are currently working on measuring more spectra in HfF^+ and potentially other candidate molecules. Rumor is they don't even like American Idol, so progress should be swift.

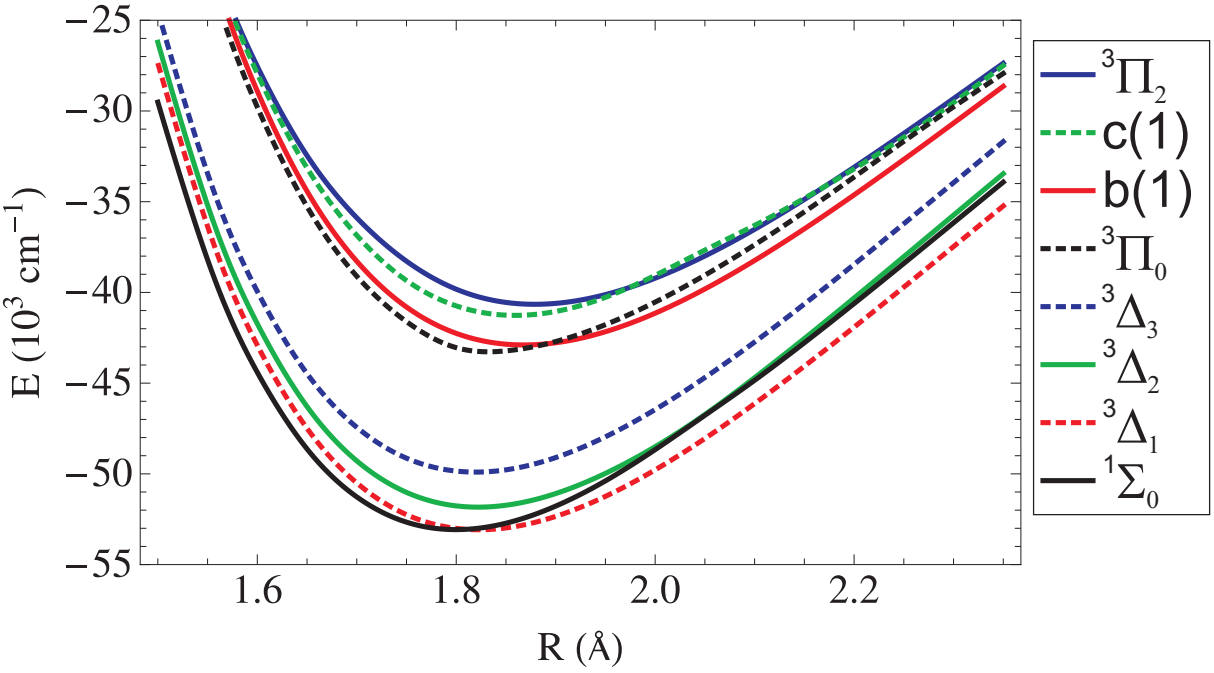

Figure 2.2: Potential energy curves for select states of HfF^+ [4]. The b(1) and c(1) states are well-mixed combinations of $^1\Pi_1$,$^3\Pi_1$, and $^3\Sigma_1^-$ states.

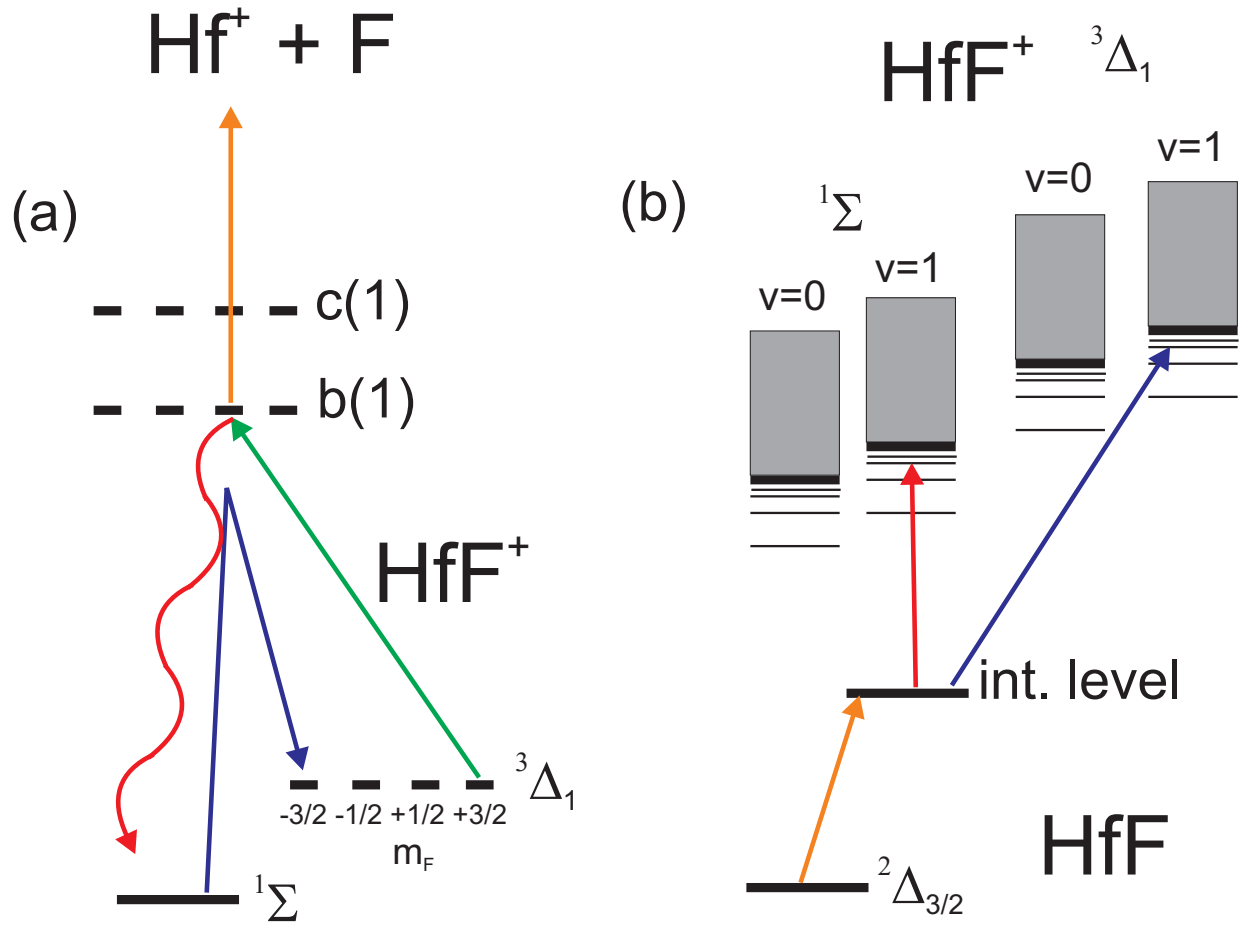

..

Figure 2.3: Molecular levels in HfF and HfF^+ discussed throughout this thesis. (a) A schematic of levels in HfF^+ useful in measuring the eEDM are shown. Ion population in the $^1\Sigma$ ground state might be transferred, using STIRAP (blue), to the $^3\Delta_1$ level where precision Ramsey spectroscopy is performed to search for the eEDM. After the Ramsey sequence, a spin-dependent transition (green) using σ-polarized light can be used to measure spin populations, either through fluorescence (red) decay or by making a photo-dissociation transition (orange) to $Hf^+ + F$. (b) A schematic of levels useful in creating HfF^+ via photoionization of HfF are shown. A transition (Orange) to an intermediate state of HfF is followed by a transition to a Rydberg state with a vibrationally excited HfF^+ core in the $^1\Sigma$ (red) or $^3\Delta_1$ (blue) state, which can then autoionize to the v=0 continuum (grey boxes) of the respective states. This process is discussed in Chapter 5.7. Energy splittings not to scale.

Chapter 3

Ion Trapping

In a charge free region, electric potentials obey Laplace's equation,

$$\nabla^2 V = 0 \tag{3.1}$$

Solutions to this equation allow no local extremum, *i.e.* all maximums and minimums must occur at the boundaries. Therefore, it is impossible to produce a three-dimensional trapping potential in free space from static electric fields alone. Two solutions to this problem are found in the Penning trap and the rf Paul trap. In a Penning trap [66], the combination of static electric and magnetic fields allows for 3-D confinement. In an rf Paul trap [67, 68], time-varying electric fields are used to create a time-averaged potential with a minimum at the trap center. In our eEDM experiment, the energy difference we wish to precisely measure is, to a very good approximation as discussed in Chapter 6, independent of the electric field, while being quite sensitive to magnetic fields. For this reason, an rf Paul trap seems the better choice here.

3.1 Ions in Two-Dimensional Time-Varying Quadrupole Fields

A general three dimensional quadrupole field has a potential,

$$\Phi(x, y, z) = \Phi_0(\lambda x^2 + \sigma y^2 + \gamma z^2) \tag{3.2}$$

where Φ_0 is an externally applied, position independent electric potential and λ, σ, and γ are constants depending on the nature of the field. With this potential, the three dimensions are not

coupled, and motion along these three directions can be treated independently. Laplace's equation requires

$$\lambda + \sigma + \gamma = 0 \tag{3.3}$$

When $\lambda = -\sigma$ and $\gamma = 0$, we obtain a two-dimensional quadrupole field. This field is utilized in quadrupole mass spectrometers, and is convenient to discuss first before tackling three-dimensional ion trapping fields. Using four rods with a hyperbolic structure, as seen in Fig. 3.1, and applying a potential of $(U - V_{\rm rf}\cos\omega_{\rm rf}t)/2$ to one pair of oppositely placed rods and $(-U + V_{\rm rf}\cos\omega_{\rm rf}t)/2$ to the other pair, the following potential is achieved [5, 69],

$$\Phi(x, y, t) = (U - V_{\rm rf}\cos\omega_{\rm rf}t)\frac{x^2 - y^2}{2r_0^2} \tag{3.4}$$

with $2r_0$ the smallest distance between opposite hyperbolic rods. Using

$$M\frac{d^2x_i}{dt^2} = \frac{-e\partial\Phi}{\partial x_i} \tag{3.5}$$

we obtain the following equations of motion,

$$\frac{d^2x}{dt^2} + \frac{e}{Mr_0^2}(U - 2V_{\rm rf}\cos\omega_{\rm rf}t)x = 0 \tag{3.6}$$

$$\frac{d^2y}{dt^2} - \frac{e}{Mr_0^2}(U - 2V_{\rm rf}\cos\omega_{\rm rf}t)y = 0 \tag{3.7}$$

$$\frac{d^2z}{dt^2} = 0 \tag{3.8}$$

Making substitutions to dimensionless variables, we can rewrite the above equations for x- and y-motions as

$$\frac{d^2x}{d\zeta^2} + (a - 2q\cos 2\zeta)x = 0 \tag{3.9}$$

$$\frac{d^2y}{d\zeta^2} - (a - 2q\cos 2\zeta)y = 0 \tag{3.10}$$

with

$$a = \frac{4eU}{Mr_0^2\omega_{\rm rf}^2}; q = \frac{2eV_{\rm rf}}{Mr_0^2\omega_{\rm rf}^2}; \zeta = \frac{\omega_{\rm rf}t}{2} \tag{3.11}$$

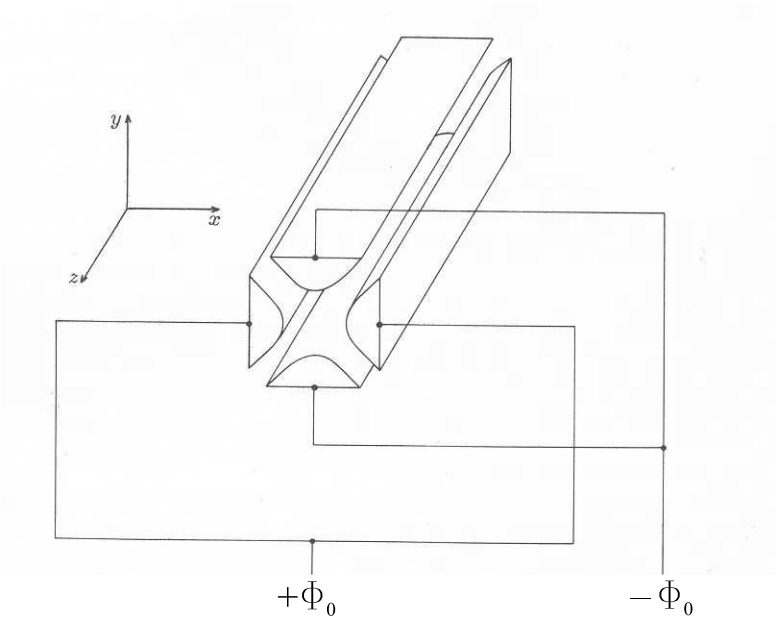

Figure 3.1: Electrodes used to produce a two-dimensional quadrupole field. For a quadrupole mass spectrometer, $\Phi_0 = (U - V_{\mathrm{rf}} \cos \omega_{\mathrm{rf}} t)/2$. Adapted from [5].

Eqn. 3.9 is the canonical form of the Mathieu equation, a well studied equation used in many areas of physics. Floquet's Theorem guarantees solutions of the form,

$$x = \alpha' e^{i\beta\zeta} \sum_{n=-\infty}^{\infty} C_{2n} e^{2in\zeta} + \alpha'' e^{-i\beta\zeta} \sum_{n=-\infty}^{\infty} C_{2n} e^{-2in\zeta} \tag{3.12}$$

Here, α' and α'' are constants whose values depend on the initial conditions of the ions. The C_{2n} constants and the characteristic exponent, β, depend on the parameters a and q. From this we see that periodic solutions exist if β is purely real, otherwise x increases without bound as $\zeta \to \infty$. If β is a real integer, the solution is periodic, but unbounded. The β = n contours in the a-q plane, with n a real integer, serve as the boundaries between stable and unstable regions. Eqn. 3.10 has identical solutions with a replaced by $-a$. The four contours of $\beta = 0$ and $\beta = 1$ for both the x and y directions bounds the first stability zone as seen in Fig. 3.2. This is the region in which almost all ion quadrupole traps and guides are operated.

From Eqn. 3.12, when β is real, the ion motion frequencies are,

$$\omega_n = \frac{(2n \pm \beta)\omega_{\mathrm{rf}}}{2} \tag{3.13}$$

This shows the frequency spectrum is the same along contours of constant β in the stability diagram, with the weighting factors of the various frequencies, the $C'_{2n}s$, being determined only by the parameters a and q. However, the exact trajectory of the ions depends on their initial position and velocity, and the initial phase of the rf. Along the $\beta = 0$ line, the lowest order frequencies are 0 and ω_{rf}. Along the $\beta = 1$ line, the fundamental frequency of ion motion is $\omega_{\mathrm{rf}}/2$. As discussed in Chapter 3.3 the rf voltage V_{rf} can be viewed as giving a time-averaged psuedo-potential that is focusing in both the x- and y-directions. The DC potential U breaks the symmetry between the x- and y-directions, with a positive U creating a focusing potential in the x-direction and a defocusing potential in the y-direction. The $\beta = 0$ contours in the stability diagram (Fig. 3.2) then correspond to values of U and V_{rf} such that the focusing potential from the rf fields is exactly cancelled with the defocusing caused from the DC fields in either the x- or y-directions, leading to unstable ion motion. The $\beta = 1$ contours have trapping frequencies due to the combination of rf

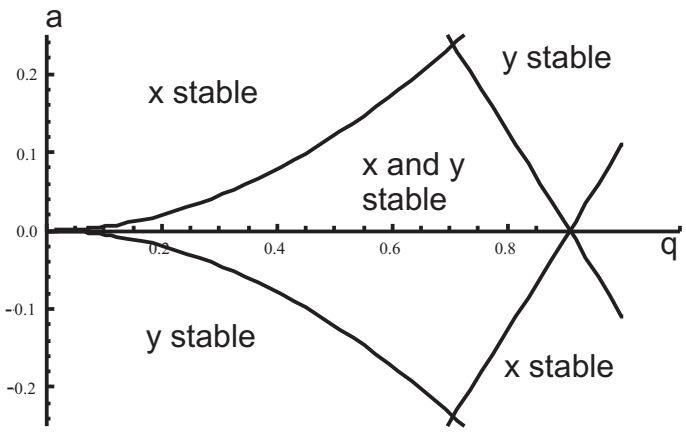

Figure 3.2: Ion stability diagram in terms of the dimensionless trapping parameters $a = \frac{4eU}{Mr_0^2\omega_{\rm rf}^2}$ and $q = \frac{2eV_{\rm rf}}{Mr_0^2\omega_{\rm rf}^2}$. The bounds of stability are the $\beta_{x,y} = 0$ and $\beta_{x,y} = 1$ contours.

and dc voltages that are exactly $\omega_{\rm rf}/2$, here the rf drive resonantly excites the trapping motion and leads to unbounded ion motion.

Since the parameters a and q depend on the mass-to-charge ratio, M/e, of the ions being trapped, the rf quadrupole can be used to measure M/e of an ion sample. This is most readily accomplished by utilizing the narrow tip of stability at q ≈ 0.706 and scanning along a line of constant $U/V_{\rm rf}$ as seen in Fig. 3.3. Here, we plot the stability diagram as a function of U and $V_{\rm rf}$ at a fixed rf drive frequency $\omega_{\rm rf}$ for ions with different values of M/e. As seen in the figure, as $U/V_{\rm rf}$ is scanned only a small range of mass-to-charge ratios are stable. This method of mass filtering has the advantage of simple tuning of the resolution, at the expense of sensitivity, by picking a slightly different constant for the $U/V_{\rm rf}$ scan. Sensitivity is decreased at higher values of $U/V_{\rm rf}$ due to the lower trapping potential as you approach the unstable region and the lower phase space of ions that will make it through the quadrupole. This utilization of the rf quadrupole as a mass filter inspires the choice of applying a potential U to one set of opposing rods, thus breaking the x-y symmetry of the ion guide.

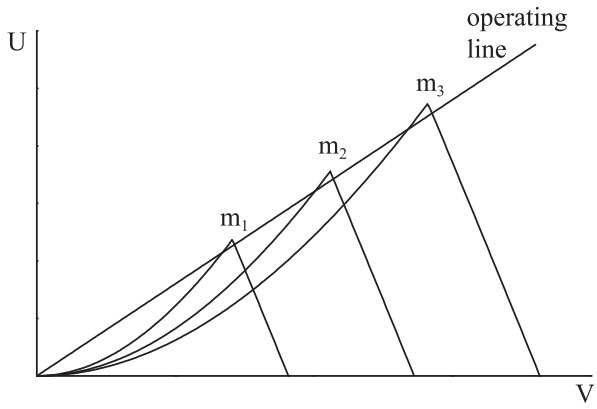

Figure 3.3: Ions of different masses will have different stability regions when graphed in terms of the DC (U) and rf (V_{rf}) trapping voltages. This graph is for a constant rf frequency ω_{rf}. By scanning along a line of constant U/V_{rf} and recording ion signal, a mass spectrum is produced. Greater resolution is achieved, at the expense of sensitivity, by increasing the slope of the scan line.

3.2 3-D Ion Trapping, the Linear Paul Trap

One way of achieving a three dimensional trapping potential is the linear rf Paul trap. The previously discussed four-rod geometry is used with the addition of a DC potential that is axially focusing and radially defocusing,

$$\Phi_{ax} = \frac{kU_z}{2r_0^2}(z^2 - \frac{x^2}{2} - \frac{y^2}{2}) \tag{3.14}$$

with U_z an applied potential and k a dimensionless geometric factor. This potential is achieved by applying a DC voltage to end-caps. The geometry of these end-caps depends on trap design, but can entail needle electrodes or segmenting each quadrupole rod into two end-caps and a central electrode. The radial focusing from the rf induced pseudo-potential must then overcome the radial defocusing from the DC potentials. Since the fields in the three dimensions are de-coupled, we can treat each direction separately. The z-direction is trivial, with a DC harmonic potential well leading to simple harmonic motion. In the x- and y-directions, the defocusing from this new DC potential can be quantified by modifying the a parameter,

$$a_{\text{eff}} = \frac{4e}{Mr_0^2\omega_{\text{rf}}^2}(U \mp \frac{kU_z}{2}) \tag{3.15}$$

with the -(+) corresponding to the x(y) direction. This leads to a shift in the first stability region to higher q values as seen in Fig. 3.4.

Another often used geometry is commonly referred to as the 3-D Paul trap. Here, a ring electrode with hyperbolic cross-section is used in conjunction with two end-cap electrodes which are hyperboloids of revolution around the z-axis and complementary to the intermediate ring electrode. The potential is then,

$$\Phi = \Phi_0(\frac{x^2 + y^2 - 2z^2}{4z_0^2}) \tag{3.16}$$

with $r_0^2 = 2z_0^2$. This leads to a similar stability diagram as the two dimensional case, except there is an asymmetry between the r and z directions.

Historically, this has been the more common geometry. However, the linear Paul trap has been adopted for many AMO experiments due to several advantages. Its initial interest was due to

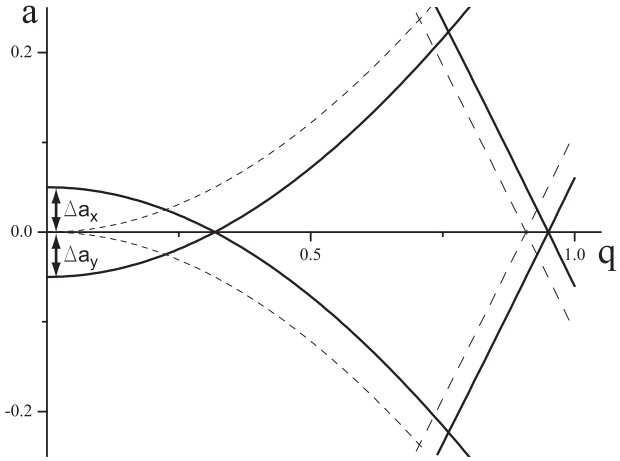

Figure 3.4: The a_x and a_y trapping parameters are shifted in the case of the linear Paul trap due to an axial trapping potential, U_z, and also from space charge effects due to a trapped ion density of ρ. $a_{\text{eff}} = \frac{4e}{2Mr_0^2\omega_{\text{rf}}^2}\left(U \mp \frac{kUz}{2} \mp \frac{\rho r_0^2}{\epsilon_0}\right)$.

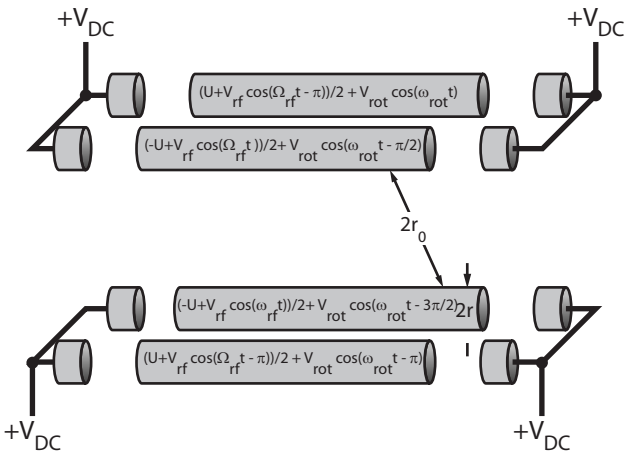

Figure 3.5: Our ion trap design. Potentials are shown that create the necessary fields for trapping, mass spectrometry, and applying $\mathcal{E}_{\rm rot}$.

its smaller second order doppler shift in frequency standards applications [70]. The linear geometry gives a line down the axial center of the trap where the rf voltage is zero as opposed to a single point in the earlier geometry. This allows for a greater number of ions to be stored at low rf voltage when space charge effects are taken into account. Heating in the trap occurs due to collisions that dephase the ion motion from the applied rf fields. Therefore, the lower the rf fields the ions are stored in, the lower the heating rates. Linear traps also offer greater optical and ion access for loading the trap and manipulating and detecting the stored ions. The linear trap is especially suited to our experiment due to the rotating bias field that we require. The four rods in our ion trap can be driven 90° out of phase, as seen in Fig. 3.5 in order to produce the rotating field. This also means that all of the time-varying fields are in the radial plane, which greatly simplifies analysis of our experimental systematics.

3.3 Pseudo-Potential Well

Although the stability diagram of Fig. 3.2 is quite useful, it does not tell the whole story. Whether an ion will remain within the physical confines of the trap depend not only on the a and q trapping parameters, but also on the ion's initial position, velocity, and the initial rf phase. In general, the ion motion will be a complicated sum of several motional frequencies, all with similar

weighting. A complete description requires numerical methods, and methods based on phase-space dynamics have been developed [69]. However, if the trap is operated in a region of small q and smaller still a, analytic methods [5] are useful. We will operate in this regime, with typical experimental values as seen in Appendix A, giving $a = 0.01$ and $q = 0.2$.

In this limit of small q and smaller a, and thus small β, we see from Eqn. 3.13 that the lowest order frequencies are well separated, with $\omega_0 = \beta\omega_{\rm rf}/2$ and $\omega_1 \sim \omega_{\rm rf}$. We then expect a slowly varying, large amplitude motion X (the secular motion) and a rapidly varying, small amplitude motion, δ (the micromotion),

$$x = \delta + X \tag{3.17}$$

Then, Eqn. 3.9 can be re-written as,

$$\frac{d^2\delta}{d\zeta^2} + (a - 2q\cos 2\zeta)X = 0 \tag{3.18}$$

Since a is assumed to be smaller than q, and X is assumed to be slowly varying compared to the rf drive frequency, we integrate Eqn. 3.18 to obtain,

$$\delta = -\frac{qX}{2}\cos 2\zeta \tag{3.19}$$

Substituting in Eqn. 3.17 and Eqn. 3.19 to Eqn. 3.9 we obtain,

$$\frac{d^2x}{d\zeta^2} = -aX + \frac{aqX}{2}\cos 2\zeta + 2qX\cos 2\zeta - q^2X\cos^2 2\zeta \tag{3.20}$$

Taking the average acceleration of X to be the acceleration of x over one rf cycle we obtain,

$$\left\langle \frac{d^2X}{d\zeta^2} \right\rangle = \frac{1}{\pi}\int_0^\pi \frac{d^2x}{d\zeta^2}d\zeta = -\left(a + \frac{q^2}{2}\right)X \tag{3.21}$$

This shows, averaged over an rf cycle, that we have simple harmonic motion with a frequency of $(a+q^2/2)^{1/2}\omega_{\rm rf}/2$. Knowing that this is equal to $\beta\omega_{\rm rf}/2$, we see that $\beta \approx (a+q^2/2)^{1/2}$ in the limit of small a and q. This approximation is good at the 5% level for $q < 0.4$. We can associate a trap depth to this simple harmonic potential, and for $a = 0$ we obtain,

$$D_x = \frac{1}{2}\omega_x^2 r_0^2 = \frac{q^2\omega_{\rm rf}^2 r_0^2}{8} = \frac{eV_{\rm rf}^2}{4Mr_0^2\omega_{\rm rf}^2} \tag{3.22}$$

The separation of the ion motion into a slow secular motion and a fast micromotion is strong motivation to work in the limit of small a and q during our eEDM measurement.

3.4 Trapping Multiple Ions

To this point, we have discussed the trapping of a single ion with an idealized quadrupole electric field. The situation becomes considerably more complex when multiple ions are trapped simultaneously. When considering neutral-neutral collisions, satisfactory results are usually found by assuming hard sphere collisions described by a single scattering length. For 1/r interactions, hard collisions that entail momentum transfer on order of the average thermal momentum are but a small part of the story. The distance over which long range collisions are important is approximately the Debye length, or Debye shielding distance,

$$\lambda_D = \left(\frac{\epsilon_0 kT}{n_i (Ze)^2} \right)^{1/2} \tag{3.23}$$

where ϵ_0 is the permittivity of free space, k is the Boltzmann constant, T is the ion temperature, n_i is the ion density, and Ze is the ion charge.

In the case of a 10 K cloud of 1000 trapped ions, and an ion cloud diameter of 1 cm, λ_D will be $\sim$ 7 mm, or about the ion cloud size. The ion-ion interaction energy at a distance of 1 cm is $\sim$ 1 mK. This means that a single ion will be in constant collision with $\sim$ 1000 ions, all with collision energies of 1 mK or above. An individual ion motion, even in the absence of collisions with ions or neutrals, can be quite complicated with at least the two frequency components of rf micromotion and trapping secular motion. It is easy to imagine that the combination of these complicated motions, with a thousand ion-ion interactions at an appreciable energy compared to the ion temperature, will lead to chaotic motion in the trap and a very broad frequency spectrum. This broad frequency spectrum will likely include components that are resonantly excited by the rf drive, thus extracting energy from the rf field and heating the ions. This is one component of what is broadly referred to as rf heating. Other components can include the effect of ion-neutral collisions and hard ion-ion collisions that dephase the ion motion from the rf drive. The latter

effect is sometimes referred to as instability heating and can be viewed as a momentary increase in the q parameter such that the ion temporarily falls into an unstable region where the ion motion increases with time.

If the initial ion velocity distribution is anisotropic or non-Maxwellian, ion-ion collisions will redistribute the ions. The rate at which this is done can be estimated using the self-collision time [71],

$$t_c = \frac{11.4 M^{1/2} T^{3/2}}{n_i (Ze)^4 ln\Lambda} \tag{3.24}$$

where M is the ion mass in amu, T the ion temperature in Kelvin, n_i the ion density in cm^{-3}, and Λ is a shielding parameter related to the Debye length. This has been confirmed for the case of protons trapped in a 3-D quadrupole ion trap [72]. For our case of a 10 K ion cloud with 1000 ions in a 1 cm ion cloud, and assuming singly charged ions of mass 200 amu, $t_c = 640$ ms.

Outside of collisions, ion-ion interactions will also add another term to the electric potential. For simplicity, take the case of a spherical symmetric trapping potential such that $\omega_x = \omega_y = \omega_z$. In the limit of space charge energy less than the thermal energy of the ions, the limit we will likely perform our experiment in, the ion cloud will have a Gaussian shape. The situation is easier to evaluate in the opposite limit, where the space charge energy is much greater than the thermal energy of the ions and, assuming a harmonic pseudo-potential well, where the ion cloud will be a sphere of uniform density. The potential due to space charge will then be,

$$\Phi_{sc} = \frac{-\rho}{\epsilon_0} \left(\frac{x^2}{2} + \frac{y^2}{2} + \frac{z^2}{2} \right) \tag{3.25}$$

where ρ is the charge density of the ions. This will modify the a trapping parameter which will now read,

$$a_{\text{eff}} = \frac{4e}{M r_0^2 \omega_{\text{rf}}^2} \left(U \mp \frac{kU_z}{2} \mp \frac{\rho r_0^2}{\epsilon_0} \right) \tag{3.26}$$

with the -(+) corresponding to the x(y) direction. The situation is more complex at values of a and q such that the motion cannot be approximated as a fast micromotion and a slow secular motion. In this case, the ion cloud can be significantly distorted from a uniform, spherical object during a trapping period.

3.5 Our Ion Trap, v0.0

Often quadrupole construction is done with cylindrical rods in place of hyperbolic rods due to the relative ease of construction of the former. Denison [73] has investigated the optimum electrode size and spacing for cylindrical electrodes. The symmetry of the problem requires that the lowest order terms are a quadrupole and then a 12-pole term. Denison looks for a minimum in the 12-pole coefficient as r/r_0, the ratio of the electrode radius to half the spacing between opposite rods (see Fig. 3.5), is varied. This was done with the ground potential at infinity and at 3.54 r_0 (the smallest practical radius for a grounded cylinder placed around the quadrupole), yielding optimum ratios for r/r_0 of 1.146 and 1.1468 respectively.

An image of our trap is shown in Fig. 3.6. We utilized a grounded wire mesh at R = 3.54 r_0, non-magnetic 316 stainless steel electrodes of 25 mm diameter, with a spacing $2r_0$ = 21.8 mm, yielding the above stated optimum ratios. Each rod was segmented into three pieces, with the axially confining DC voltages applied to the eight end-pieces. The length of the center electrodes, l_c, was 88 mm, and the length of the end electrodes, l_e, was 25 mm. Vespel spacers were used to electrically isolate the three segments of the electrodes, chosen for vespel's ease of machining, as well as its vacuum, electrical, and mechanical characteristics. Two stainless steel end-plates were used to define the electrode spacing, with threaded rods running down the center of the hollow electrodes held by washers at the end-plates providing rigidity to the whole structure. The threaded rods extended into a 6" CF vacuum flange that contained all of the electrical feedthroughs for the trapping voltages as well as supporting a channeltron ion detector. The openings at the axial ends of the the trap were covered by a 75% visibility wire mesh, making the entire trapping volume well isolated from external electric fields.

The axial trapping potential was simulated using the electrostatic program SIMION. Fig. 3.7 shows the axial potential at the radial trap center for various ratios of the center electrode to end-cap electrode length. The choice of an 88 mm center rod length gives rise to an approximate square well potential. If a harmonic axial potential is desired, a fit to the potential over the range

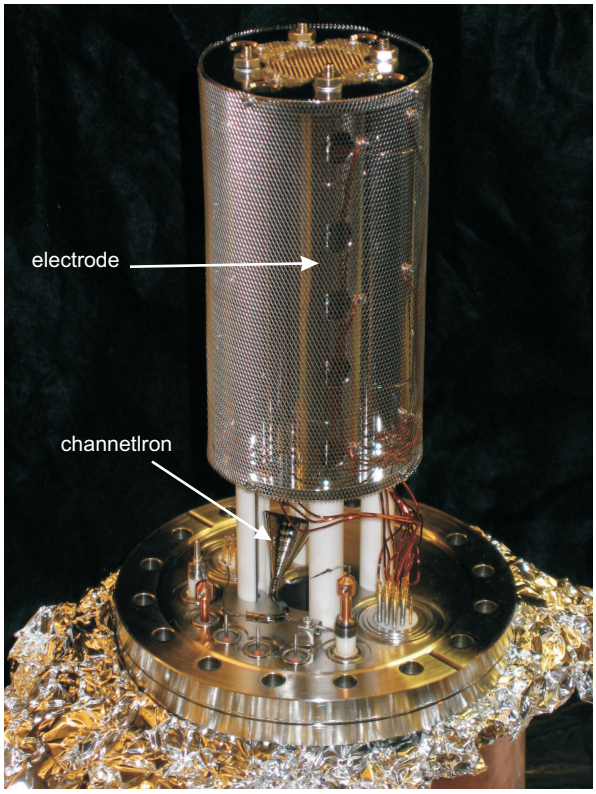

Figure 3.6: Image of our first ion trap. The electrodes are obscured by the grounded wire mesh at R = 3.54 r_0. Note the channeltron ion detector mounted below the trap.

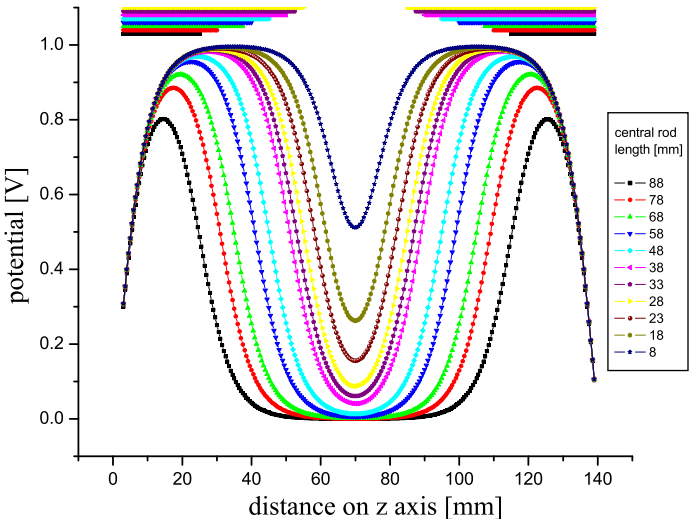

Figure 3.7: Axial trapping potentials for different central rod lengths, l_c, holding the overall trap length constant. Our first trap was built with $l_c = 88$ mm.

of its full width half maximum yields an optimized center rod length of $\approx$ 25mm for our value of 21.8 mm for r_0. However, for a 10 K ion cloud, only 2 V must be applied to the end-caps in the case of $l_c = 88$mm in order to confine the ions to a 1cm length along z. In this case, the trapping potential seen by the ions is extremely harmonic.

3.6 Trap Drive Electronics

We wish to apply rotating electric fields with the trap electrodes at frequencies $\omega_{\rm rot} \sim 2\pi\times100$ kHz, and superimpose rf trapping fields that oscillate at frequencies $\omega_{\rm rf} \sim 2\pi\times15$ kHz. This gives wavelengths on the order of 1 km, much larger than the distance between the source electronics and the trap. Therefore, impedance matching was of no concern in designing our drive electronics. Flexibility was essential, as we desired to operate the trap with different ion species and at very different trapping frequencies and trapping parameters a and q, depending on the nature of the experiment being performed. We chose to use a system of op-amps as opposed to more traditional methods of ion trap drivers such as resonant LRC circuits or quarter-wave resonators [74].

We used buffers/pre-amplifiers with standard $\pm$ 15 Volt op amps (OPA627) and their outputs were used as inputs to simple summing amplifiers. In order to achieve relatively high trapping

Table 3.1: Electrical inputs to ion trap driver box.

Name of input	Purpose of applied voltage	Electrode segments
RF	Oscillating trapping voltage for radial confinement	phase: A and D rods antiphase: B and C rods
DC A rod DC D rod	Radial defocussing voltage, seperate to move trap center radially	A rod D rod
DC bottom	axial confinement, ability to load trap	A,B,C,D bottom end-caps
DC A,B top DC C,D top	axial confinement, ability to steer ions into detector	A, B top C, D top
DC center rods	alternative axial confinement	A,B,C,D center

potentials, high voltage OPA98 op-amps were used for the summing amplifiers. These have the ability to drive up to $\pm$ 225 Volts, with maximum slew rates of 1000 V/μs. Radial trapping potentials, for Hf^+ ions, as high as 16 eV were achieved with rf trapping voltages of 190 Volts and a trap frequency of 250 kHz. At these high trapping voltages and frequencies, forced air cooling was found to be insufficient, and the OPA98 op-amps were mounted on water-cooled copper heat sinks. The summing amplifiers included a trim input used to reduce DC offsets to $\sim$ 5 mV, with drifts over the course of 10 hours of similar magnitude.

Each electrode segment was driven by a separate OPA98, and several inputs were available, listed in Table 3.1, for applying rf and DC voltages. These inputs allowed us to manipulate the ions in many ways, including ejecting ions from the trap, moving the axial and radial trapping center, and performing mass spectrometry. The DC voltages were supplied by an NI6733 DAQ board, with eight sixteen bit analog outputs and with maximum update rates of 1000 kS/s. We buffered the output of this board in order to source more current and to separate the computer ground from the experiment ground. The rf voltages were obtained from an Agilent 33220A waveform generator, capable of being AM or FM modulated. The rf was AC coupled to inverting (A,D rods) and non-inverting (B,C rods) pre-amplifiers to produce the π phase delay between adjacent electrodes. Both the DAQ and the waveform generator were computer controlled via LabView code.

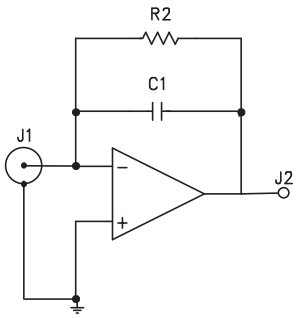

Figure 3.8: Schematic of an integrator used to sum and amplify our ion signal when dumping our ion trap into a channeltron detector. Gains of either 10^{10} or 10^{8} were typically used.

3.7 Ion Detection

Detection of ions can be highly efficient with the use of a channeltron, a form of electron multiplier. Here an ion is accelerated to 1000's of eV before striking the detector, with close to unit probability of dislodging an electron from the surface. This primary electron is then accelerated down the detector where it again collides with the detector walls and is amplified in an electron avalanche, in the same way a primary electron is amplified in a photomultiplier tube. This can result in ion detection efficiencies of ~ 1, and gains of 10^6 or more.

Our initial ion trapping experiments utilized a channeltron, placed after the axial opening of the trap, with the input of the detector biased at -2000 Volts and the output at ground potential. Ions were ejected from the trap by dropping the end-caps nearest the detector to 0 V or to a slight negative voltage, while the end-caps farthest from the detector remained at a positive bias. A simple electronic integrator was used (Fig. 3.8) in order to further amplify the signal, and to reduce saturation effects due to the channeltrons inability to source much voltage. Two gain settings were typically used of 10^{10} and 10^{8} V/A with corresponding time constants of 30 μs and 10 ms respectively. Dark count rates on the order of 1/s were achieved when operating in pulse counting mode.

In order to attempt an absolute calibration of ion number, we employed a Faraday cup. This is simply a metal can that collects the positive ions. A commercial CR-110 charge sensitive pre-

amplifier was placed directly after the vacuum electrical feedthrough that connected the Faraday cup. This configuration produced a minimum noise equivalent to 300 ions per trap "dump".

A device similar to the channeltron is the microchannel plate detector, or MCP. An MCP can be viewed as a 2-D array of micro-channeltrons. Typical dimensions are a plate thickness of 500 μm, with hole diameters of 10 μm, and an open area of 60%. Each hole acts as a channeltron, as incoming ions are accelerated and collide into the hole walls they create primary electrons that are themselves accelerated into the walls creating an electron avalanche. Gains of a single plate tend to be 10^4, with higher gains achieved by placing two or more plates in series. Two main types of MCPs were used during this experiment, an imaging MCP and a "fast" MCP.

In the imaging MCP a phosphor screen is placed behind the output of the MCP, and is biased at a large positive voltage. The electrons output from the MCP are accelerated onto the phosphor screen and a CCD camera records the resulting fluorescence. This detector is obviously helpful in determining the spatial profile of the ion cloud, but is poor at recording arrival times. In order to get some information on arrival times, we typically pulsed on the negative bias voltage to the MCP. This was limited to a time resolution of ~ 1 μs by the 5 mm distance between the MCP and a grounded wire mesh placed in front of the MCP.

For the "fast" MCP, a single electrode, at ground potential, is placed at the output. This can lead to much faster detection times than with a channeltron, since the electron transit times are much smaller in the extremely thin MCP. This device gives no ion position information, other than the fact the ion fell somewhere on the device, but the time resolution can be as fast as 100 ps, although typically the read-out electronics limits this to slower values. These devices are often used in time-of-flight mass spectrometers due to their time resolution and we utilized them in this capacity as discussed in Chapter 5. A fast transimpedance amplifier was used in conjuction with these MCPs. This reduced the time resolution to ~ 20 ns, but this was still sufficient for our needs.

3.8 Early Ion Trapping

We loaded ions into our trap using electron impact ionization in our earliest ion trapping experiments. A solenoid driven pulsed valve was opened typically with a 200 Volt, 300μs drive pulse and 1 Torr of Xe backing pressure. The gas pulse was intersected by a 200 ms electron gun pulse, both being directed through the center of the ion trap. This was done while rf trapping voltages of $\sim$ 20 Volts were applied at 100kHz, and the end-caps were biased at 15 Volts DC. Trapping times on the order of minutes were achieved after an initial ion decay that was due to increased background pressure from the xenon gas pulse. Xenon was used since it had a similar mass to our leading eEDM molecules at the time, HI^+. Xenon has seven naturally occurring isotopes, five of them have greater than 5% abundance, and they are spaced by one or two amu. This isotope structure allowed us to test our ability to perform mass spectrometry in our trap. As discussed in Chapter 4, mass spectrometry could possibly be used to read-out the electron spin in our eEDM measurement. Therefore, demonstrating mass spectrometry in our ion trap with 1 amu mass resolution and high sensitivity was one of our first ion trapping objectives.

Mass spectrometry was done by loading the ion trap with the voltage $U = 0$, and then ramping U to obtain a set value of U/V_{rf}, the voltage U was ramped back to zero and then the ions were ejected from the trap using the end-cap voltages and sent into a channeltron for detection. The rf Voltage V_{rf} was then stepped to a higher value and the experiment was repeated. In this way we probed the typical U/V_{rf} operating line of a quadrupole mass spectrometer. One initial difficulty in achieving sensitive mass spectrometry at good resolution was higher order resonances in our ion trap. Due to details of the electronics and DAQ boards used, the ramp of U was done in discrete steps with 1 ms between steps. As we stepped across the $\beta = 2/3$ contour, ions would be lost from the trap. The data showing at what rf voltage ion loss began, for different U ramp values, is shown in Fig. 3.9. Plotting these points out on the a, q stability graph, we see that the loss was indeed associated with the $\beta = 2/3$ line. This problem was circumvented simply by increasing our U voltage ramp speed, but it is worth pointing out that the next generation ion trap, discussed

below, will likely be driven in such a way as to increase these higher order resonances that arise due to imperfections of the trapping fields. It will likely be important to operate the trap at values of a and q that are far removed from these resonances. Discussion of these trap resonances can be found in the literature [75].

Resolution of the mass spectrometer tended to improve at higher trapping frequencies. Data for Xe^+ and Hf^+ showing ~ 1 amu mass resolution can be seen in Fig. 3.10. The trapping frequencies used were 100kHz for the Xe^+ data and 250 kHz for the Hf^+ data. Typical rf frequencies for commercial quadrupole mass spectrometers are 1-3 MHz. In order to reach higher resolution, the scan line should be increased to higher values of U/V_{rf}. This pushes you closer and closer to the edge of the stability region, where the trap depth is close to zero for the x direction and close to the $\beta = 1$ contour in the y direction, were the trapping frequency is one-half the rf drive frequency and resonant excitation occurs. Many factors come into play in this region that are not contained in the analytical approach of this chapter that lead to the ion stability diagram. These include the finite size of the trap, patch charge potentials on the electrodes, ion-ion and ion-neutral collisions, and field imperfections due to the cylindrical rods.

3.9 Second-Generation Ion Trap and Fields in eEDM Measurement

The first-generation trap was designed to minimize errors in our quadrupole trapping field, largely driven by our desire for ~ 1 amu mass resolution. Since building our first trap, the requirements for mass spectrometry in our ion trap have been greatly reduced, as we now will likely use a fluoride instead of a hydride for the eEDM measurement. Mass spectrometry in our next generation trap will be performed using time-of-flight, and the necessary resolution of 19 amu should be trivial to achieve. Time-of-flight mass spectrometry has the advantage of measuring multiple charge-to-mass ratio ions for a single trap loading at efficiencies close to unity. This also means that the uniformities in the trapping fields can be sacrificed for uniformity in the rotating electric field. The first trap suffered from non-uniformities in the rotating electric field of $\approx 20\%$ over a 1 cm diameter ion cloud. The next generation trap will have six electrodes instead of four, and

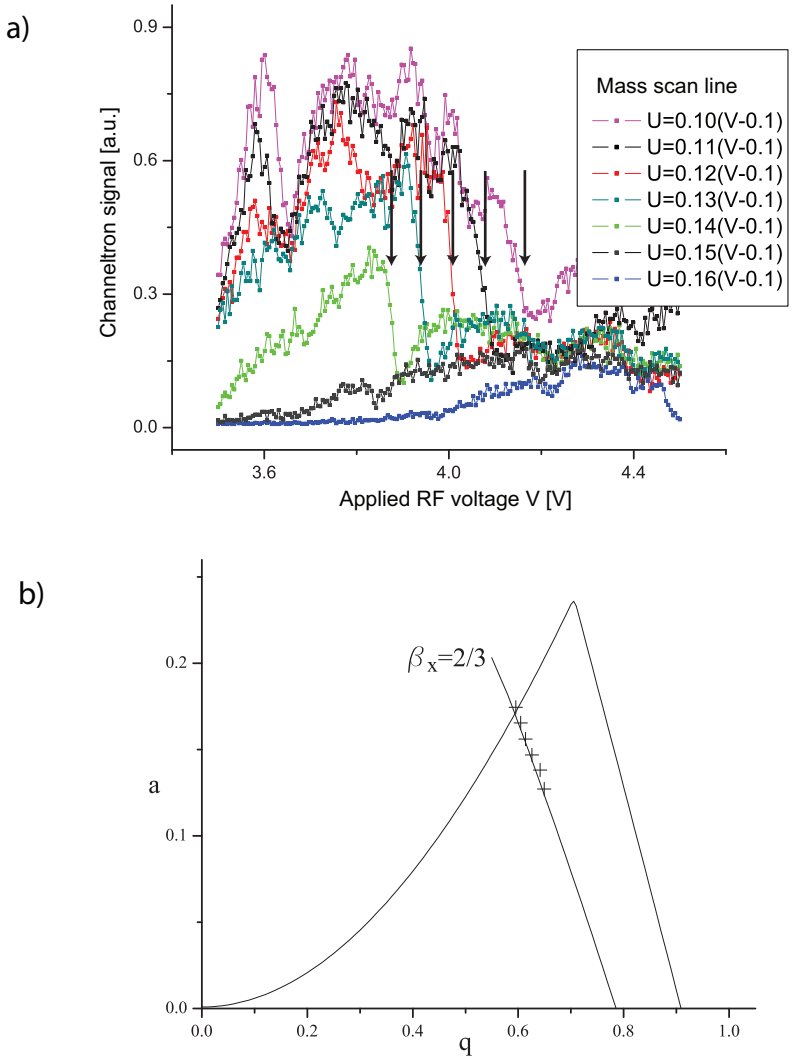

Figure 3.9: a) Ion number in trap after trap potential U has been ramped to various values as a function of rf voltage. b)Plotting the onset of loss in the a, q stability diagram shows the ion loss was associated with a $\beta = 2/3$ resonance, implying imperfections in our trapping fields.

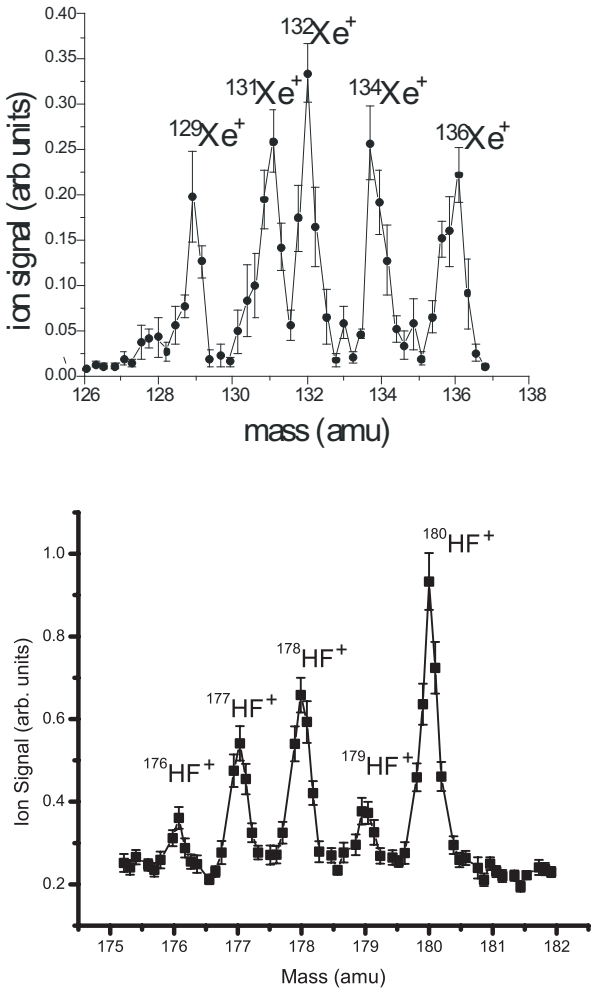

Figure 3.10: Mass spectrometry performed in our ion trap showing a) the five dominant isotopes of xenon, data taken at an rf frequency of 100 kHz, with $U/V_{\mathrm{rf}} = 0.16$ and b) the five naturally occurring isotopes of hafnium, data taken at an rf frequency of 250 kHz, and $U/V_{\mathrm{rf}} = 0.1695$. Mass resolutions of better than 1 amu allowed us to distinguish Hf^+ from HfH^+.

will be spaced farther apart ($r0 = 4.0$ cm). Numerical modelling shows the rotating electric field uniformity should be better than 0.5% over a 1 cm diameter ion cloud.

Another motivation in designing a new trap is the desire to make ion measurements through laser induced fluorescence. The maximum solid angle for optical detection achievable in our first ion trap design was limited by the large area occupied by the rod electrodes. The new trap design replaces the cylindrical rods with electrodes of thin cross-sections when viewed from the trap center. Two large ellipsoidal mirrors surround the ion trap covering 80% of the solid angle. These mirrors have a bare gold coating, as conducting surfaces are preferred to minimize patch charge effects on the trapping fields. The center sections of the mirrors are electrically isolated from the bulk of the mirrors and act as the end-cap electrodes for z-axis ion confinement.

The perfect ion trap would have idealized electric and magnetic fields as follows

$$\vec{\mathcal{E}} = \mathcal{E}_{\rm rot}\hat{r}' + \mathcal{E}'_{\rm rf}(x\hat{x} - y\hat{y})\cos(\omega_{\rm rf}t) + \mathcal{E}'_z(-z\hat{z} + y\hat{y}/2 + x\hat{x}/2) \tag{3.27}$$

$$\vec{\mathcal{B}} = \mathcal{B}_{\rm rot}\hat{r}' \tag{3.28}$$

where $\hat{r}' = \cos(\omega_{\rm rot}t)\hat{x} + \sin(\omega_{\rm rot}t)\hat{y}$ and $\mathcal{E}'_{\rm rf} \approx -2V_{\rm rf}/r_0^2$.

If we assume $\omega_{\rm rot} \gg \omega_{\rm rf}$, that $\omega_{\rm rot}/\omega_{\rm rf}$ is not a rational fraction, and that $\omega_{\rm rf}^2 \gg e\mathcal{E}'_{\rm rf}/M$, then we can cleanly separate out the ion motion into three components: rf micromotion, circular micromotion, and secular motion.

As discussed above, rf micromotion involves a rapid oscillation at $\omega_{\rm rf}$ whose amplitude grows as the ion's secular trajectory takes it away from trap center. The kinetic energy of this motion, averaged over an rf cycle, is given by

$$\mathrm{E}_{\rm rf} = (x^2 + y^2)\frac{e^2{\mathcal{E}'_{\rm rf}}^2}{4M\omega_{\rm rf}^2} \tag{3.29}$$

where x and y in this case refer to the displacement of the ion's secular motion.

The displacement of the ion's circular micromotion is given by

$$\vec{r}_{\rm rot} = -\frac{e\vec{\mathcal{E}}_{\rm rot}}{M\omega_{\rm rot}^2}. \tag{3.30}$$

The kinetic energy of the circular motion, averaged over a rotation cycle, is given by

$$\mathrm{E}_{\mathrm{rot}} = \frac{e^2 \mathcal{E}_{\mathrm{rot}}^2}{2M\omega_{\mathrm{rot}}^2}. \tag{3.31}$$

The time-averaged kinetic energies of the two micromotions act as ponderomotive potentials that contribute to the potential that determines the relatively slowly varying secular motion:

$$U_{\mathrm{sec}} = \mathrm{E}_{\mathrm{rot}}(x,y,z) + \mathrm{E}_{\mathrm{rf}}(x,y,z) + e\mathcal{E}_z'(2z^2 - y^2 - x^2)/4. \tag{3.32}$$

In the idealized case, the secular motion corresponds to 3-d harmonic confinement with secular or "confining" frequencies

$$\omega_i = \left(\frac{1}{M}\frac{\partial^2 U_{\mathrm{sec}}}{\partial i^2}\right)^{1/2}, \tag{3.33}$$

for $i = x, y, z$. In the idealized case, confinement is cylindrically symmetric, $\omega_x = \omega_y$, and $\mathcal{E}_{\mathrm{rot}}$ is spatially uniform, so the circular micromotion does not contribute to the confining frequencies.

If the density of ions is low enough such that few momentum-changing collisions occur during a single measurement, any given ion's trajectory will be well approximated by the simple sum of three contributions:

(i) a 3-d sinusoidal secular motion, specified by a magnitude and initial phase for each of the $\hat{x}$, $\hat{y}$, and $\hat{z}$ directions. In a thermal ensemble of ions, the distribution of initial phases will be random and the magnitudes, Maxwell-Boltzmannian. For typical experimental parameters (see Appendix A) the secular frequencies ω_i will each be about $2\pi \times 1$ kHz and the typical magnitude of motions, r, will be about 0.5 cm.

(ii) the more rapid, smaller amplitude rf micromotion, of characteristic frequency about $2\pi \times 15$ kHz and radius perhaps 0.05 cm. This rf micromotion, purely in the x-y plane, is strongly modulated by the instantaneous displacement of the secular motion in the x-y plane, and vanishes at secular displacement x=y=0.

(iii) The still more rapid rotational micromotion, purely circular motion in the x-y plane, at frequency ω_{rot} about $2\pi \times 100$ kHz and of radius comparable to the rf motion, around 0.05 cm. In the idealized case, the rotational micromotion (in contrast to the rf micromotion) is not modulated by the secular motion.

As described in Chapters 6.5 and 7.1, for spectroscopic reasons we must operate with trapping parameters such that $\mathrm{E_{rot}} \gtrsim 30 k_B T$. Under that condition, relatively small imperfections in $\mathcal{E}_{\mathrm{rot}}$, say a spatial variation of 1.5%, can give rise to contributions to U_{sec} of the same scale as the ions' thermal energy, and thus significantly distort the shape of the trapped ion cloud or even deconfine the ions.

Chapter 4

Electron Spin Read-Out

As mentioned previously, spectroscopic eEDM measurements perform an electron spin resonance in the presence of electric and magnetic fields. Of course, a crucial component of a spin resonance experiment is measuring the final spin populations. Typically, this is done by making a spin dependent electronic transition and then collecting fluorescence from the subsequent decay (LIF). Our trapped molecular ion experiment is limited to low ion numbers due to strong ion-ion interactions (see Chapter 7). Also, since molecules are being used, there are no cycling transitions to increase LIF detection efficiency. With multiple vibrational and rotational levels to decay to, approximately one photon will be scattered from any given molecular ion. With a limited solid angle of collection and photon detection efficiencies of ~ 0.10, LIF could have poor efficiency.

As mentioned in Chapter 3.7, ion detection using channeltron and MCP detectors can approach unit efficiency. It is tempting to leverage this high efficiency of ion detection to read-out the electron spin populations in our experiment. One approach would be to make a spin-dependent electronic transition to an excited state and then photodissociate this excited state. This would map the electron spin information onto the mass-to-charge ratio of the trapped ions. As discussed in Chapter 3, the ion trap can act as a mass filter, either by operating in the a, q stability plane at a point where a narrow range of M/e ions are trapped, or by using the trap as a time-of-flight mass spectrometer. We have also experimented with using a one-dimensional standing wave of intense laser light in order to create a spin-dependent heating of the ion cloud. This technique has also been explored as a method for performing broad survey spectroscopy of our molecular ions.

4.1 LIF Detection

ab initio calculations [4, 54, 64, 61] suggest there are $\Omega = 1$ states $\sim$ 10,000-15,000 cm^{-1} above the $^1\Sigma$ ground state and $\sim$ 7,000-14,000 cm^{-1} above the $^3\Delta_1$ level where we will perform our spin resonance measurement. Using $\sigma^{\pm}$ polarized light, we can excite only the population in the $m_F = \mp 3/2$ level to the $J = 1$ level of one of these higher lying $\Omega = 1$ states. A measurement of the fluorescent decay from this higher lying state will then yield the final spin population of our Ramsey experiment. The efficiency for LIF can be approximated, in the strongly saturated limit,

$$\eta_{LIF} = \frac{1}{2} \times \mathcal{A} \times \mathcal{R}^{N_b} \times \eta_{det} \times \mathcal{T} \tag{4.1}$$

with $\mathcal{A}$ the solid-angle of fluorescence collected onto the detector, $\mathcal{R}$ the mirror reflectivity, N_b the average number of reflections off the mirrors, η_{det} the detector efficiency, and $\mathcal{T}$ the transmission of any filters, windows, or lenses in the imaging system.

Pulsed laser excitation is preferred for several reasons. The quantization axis will be rotating at $\omega_{\rm rot}$, and we wish to make transitions only of $\delta m_F = +1$ or -1. Therefore the laser $\hat{k}$-vector should point along the quantization axis with left- or right-circularly polarized light being used. The excitation pulse must then be short compared to $1/\omega_{\rm rot}$ so the quantization axis can be treated as stationary during the pulse. Also, reaching saturation intensity on the molecular transition could be difficult with a cw laser. We might wish to drive a weaker transition that then decays to the lower $^1\Sigma$ level as this could allow us to frequency filter the signal light from the scattered light of the excitation laser. Also, the decay will then be at higher frequencies and therefore a higher detection efficiency for our PMT can be realized. This, combined with the relatively large ($r \sim$ 5 mm) ion clouds, requires more laser power than could be conveniently achieved with cw lasers. Pulsed excitation also allows time gating of the detector in order to decrease background signal due to light scatter of the excitation beam into our detector.

If the $\Omega = 1$ excited levels around 13,000 cm^{-1} are used, we will require a detector efficient at the corresponding wavelength of 770 nm. Photodiodes have high quantum efficiencies at such wavelengths, but photodiodes are not well suited to measuring the expected low light intensities

due to the inherent electronic noise, *e.g.* it will be difficult to reach shot-noise limited detection. PMTs have extremely low dark count rates, and can reach shot-noise limited detection at very low count rates. The detection efficiencies of PMTs tend to fall off dramatically at near-IR wavelengths since cathodes with low enough work functions are difficult to produce. The highest efficiency PMT in these wavelength regions that we have been able to find are the Hammamatsu R3896. We can expect quantum efficiencies, at best, of 10% in our region of interest, and more likely 1%. Perhaps transitions can be found at higher frequencies, but our current form of survey spectroscopy requires a Ti:Saph laser with minimum wavelength $\approx$ 700 nm.

With the new ion trap allowing for 80% of the solid angle to be imaged onto two photon detectors, the maximum spin detection efficiency we expect is 4% using LIF.

4.2 Photodissociation

4.2.1 Predissociation and CH^+

A process known as predissociation can occur in molecules if the molecular potential undergoes an avoided crossing, giving rise to excited vibrational levels that are allowed to tunnel out to the dissociation continuum as seen in Fig. 4.1. This situation is known to occur in CH^+ and has been subject to several experimental and theoretical treatments [76, 77, 78, 79, 80, 81]. The predissociating states in CH^+ occur due to coupling between the $A^1\Pi$ state and the $c^3\Sigma^+$ repulsive curve. The $A^1\Pi$ state dissociates to the slightly higher energy C^+ ($^2P_{3/2}$) + H(^2S) configuration compared to the $C^+(^2P_{1/2})$ + H(^2S) state that the $c^3\Sigma^+$ level dissociates to. A combination of spin-orbit coupling and nuclei rotation lead to couplings of the two molecular potentials. The potential advantage of using a predissociating state is that the bound-to-bound transition involved will often have a larger cross-section than a bound-to-continuum transition. After building an ion trap capable of 1 amu mass resolution, we decided to perform a proof-of-principle photodissociation experiment using the known CH^+ transitions.

CH^+ was produced and trapped by pulsing in CH_4 gas from a pulsed valve and using electron

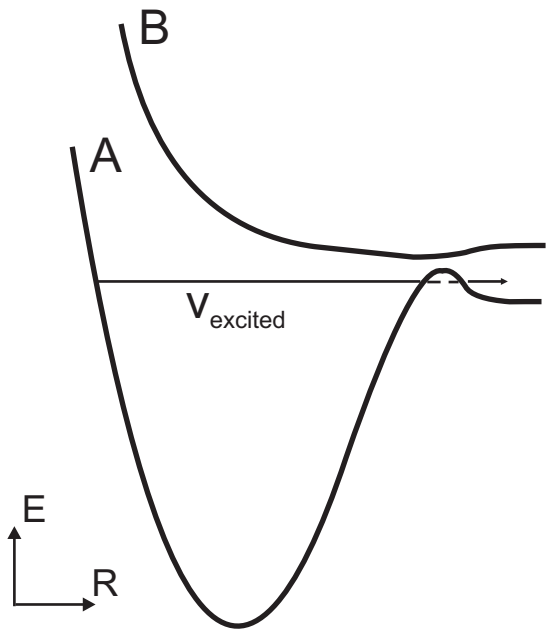

Figure 4.1: Potential energy curves of a molecule containing predissociating states as a function of the internuclear spacing R. The bound energy curve A dissociates to atoms, with at least one atom in an excited state. The repulsive curve B dissociates to atoms at a lower energy. Couplings between states A and B lead to an avoided crossing. An excited vibrational level of state A can tunnel through the resulting potential into the continuum.

impact ionization in an identical set-up to that mentioned in Chapter 3.8. The trap was loaded with trapping parameters only allowing stable trajectories for CH^+ ions. The trap parameters were then ramped to a more stable configuration where both C^+ and CH^+ were stably trapped as a 10 ns laser pulse was sent through the ion cloud. This pulse was frequency doubled to the UV (the relevant transitions were in the range of 33,000 cm^{-1}) and approximately 10 mJ/pulse was available. The trap was then ramped to parameters compatible with only C^+ and then dumped into a channeltron ion detector. Ions would be detected only if CH^+ had been dissociated to C^+ by the laser pulse.

Despite the known transitions of CH^+, we experienced two problems that frustrated our attempts to observe autoionization in our set-up. The first was charge-exchange collisions between CH^+ ions and neutral CH_4 background gas that severely limited our CH^+ trapping lifetime. Fig. 4.2 shows the results of holding CH^+ in our trap for 1 ms and 100 ms. The 100 ms data shows almost no evidence of CH^+ and instead it appears reactions produced C_2^+ ions. C_2H_2 and CHF_3 were also used as sources of CH^+ ions, all with similar effects limiting the ion storage time. The only way we were able to mitigate this problem was by decreasing the backing pressure, but this limited the number of CH^+ ions we were able to load into our trap. The optimum backing pressure of CH_4 was found to be $\sim$ 1 Torr.

The other problem was a misunderstanding of our needed laser pulse intensity. We believed the cross-section for the transition from the ground state to the $A^1\Pi$ predissociating state was a factor of 10^4 higher than what was ultimately measured. Looking at results from [80], we expected cross-sections on the order of 10^{-16} cm^2 for the transitions of interest. This meant for our experiment we should have easily saturated our $\sim$ 1 cm diameter ion cloud with a 10 mJ laser pulse. When a signal was found, we observed that the transition was far from saturated. In the end, CH^+ was trapped for 5-10 seconds as laser pulses at 10 Hz were fired into the cloud, allowing for saturation of the transition. Fig. 4.3 shows data taken in this way. Our results were consistent with other estimates for the cross-section [81, 76, 77] of $\sim 10^{-20}$ cm^{-1}. It appears there was an error in [80] and we chose the wrong reference to help us estimate our needed saturation intensity. Ultimately,

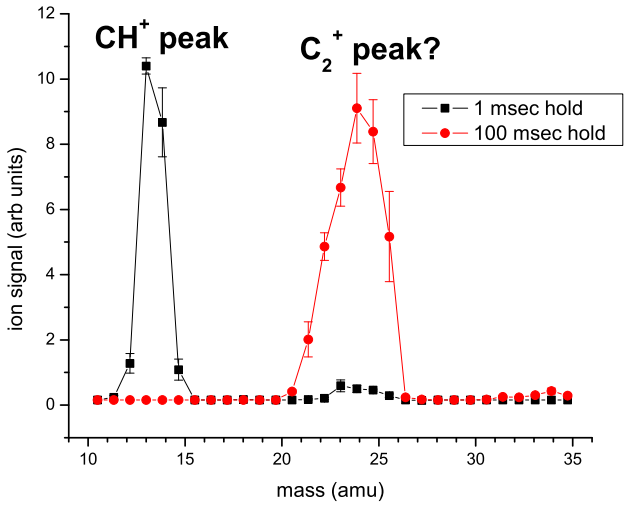

Figure 4.2: CH^+ held in our ion trap appeared to react with CH_4 gas. After trap loading, the ions are initially CH^+, but after a 100 ms hold time there is no evidence of CH^+ in the trap. Instead a mass peak around 24 amu is found. This required trap loading at lower CH_4 pressures and made detection of CH^+ predissociation more difficult.

we were able to dissociate through multiple rotational lines as many ground state rotational levels were populated from the electron-impact ionization process.

4.2.2 Photodissociation to a Repulsive Curve

The experience with CH^+ was not very encouraging in our efforts to readout electron spin information using dissociation. However, the first difficulty in observing the CH^+ dissociation, the charge-exchange collisions limiting our CH^+ lifetimes, should cause no concern for our eEDM measurement using ions such as HfF^+. We have not observed such fast charge-exchange processes to occur in HfF^+. Background pressures when trapping ions such as HfF^+ from our pulsed molecular source discussed in Chapter 5 are made small by differential pumping. As we will see in Chapter 7.2, other considerations require strong enough differential pumping such that ion-neutral collisions are rare during the coherence time of our measurement.

The small photodissociation cross sections are an area of concern. It will not be possible to wait several seconds while multiple laser pulses saturate the transition, as the lifetime of the $^3\Delta_1$ state is not expected to be that long. The CH^+ cross sections are small due to the very poor overlap between the vibrational wave function of the ground state and that of the predissociating state. According to the Franck-Condon principle, the transition moment between two electronic states will be proportional to the overlap integral between the two vibrational levels, $\int \Psi'_v \Psi''_v \, d\mathbf{r}$, with $\Psi'_v(''_)$ the vibrational wave function of the excited (ground) state involved in the transition [82]. The transition strength is proportional to the square of this overlap integral or Franck-Condon factor. The Franck-Condon principle is based on the idea that during an electronic transition, nuclei have no time to respond and therefore will have the same position and momentum immediately before and after the transition. A Franck-Condon matrix will have off-diagonal terms in $v' - v''$ if the two electronic levels have different vibrational energy spacings or bond lengths. However, the Franck-Condon factor between a $v'' = 1$ state and a $v' = 12$ state, the case for our CH^+ predisocciating transition, is typically quite small and might be small enough to negate the advantage of a bound-bound transition. An estimate of the cross section to a repulsive potential curve will reveal to what

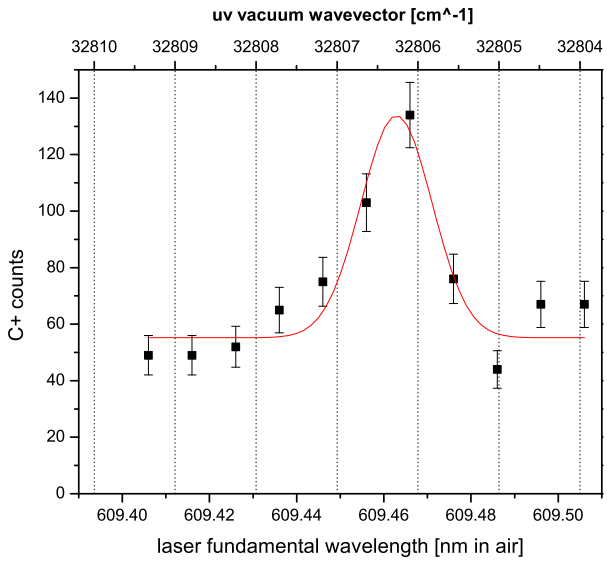

Figure 4.3: Data showing photodissociation of CH^+ to C^+ and H through a predissociation resonance. This data corresponds to a transition to the $J = 3$, $v = 12$, $A^1\Pi$ state of CH^+. This data was taken with a 5 second ion hold time, during which time 50 pulses, with 10mJ/pulse, from a frequency doubled dye laser were incident on the ions.

extent this is true.

The width of a photodissociation resonance in a diatomic molecule involving a repulsive curve will be dominated simply by the Frank-Condon overlap between the initial state vibrational wave function and the repulsive curve. A good approximation is to treat the unbound molecular wave functions as delta functions at the classical turning points [82]. Then, one needs only to know the slope of the repulsive curve at the equilibrium internuclear distance of the initial state and the width of the initial state vibrational wave function. These two numbers will then give the approximate width of the photodissociation resonance.

In order to approximate the slope of a repulsive curve in HfF^+, we look at a repulsive curve in the isoelectronic PtH^+. *ab initio* calculations [61] of PtH^+ electronic levels show a $^3\Sigma$ repulsive state. One could imagine a similar state being easily accessed from the $^3\Delta_1$ level of HfF^+ through an intermediate $^3\Pi$ state. We then simply scale the energy of dissociation for PtH^+ to that calculated for HfF^+ and use that same scaling factor for the energy of the repulsive curve. Doing this gives a $^3\Sigma$ repulsive curve in HfF^+ that is at 71,000 cm^{-1} with a slope of about 80,000 cm^{-1}/Å at the molecular bond length.

A quantum harmonic oscillator wave function is given by:

$$\Psi = (2^n n!)^{-\frac{1}{2}} (\frac{m\omega}{\pi\hbar})^{\frac{1}{4}} e^{-\xi^2/2} H_n(\xi) \tag{4.2}$$

where H_n is a Hermite polynomial of order n, $\xi = \sqrt{\frac{m\omega}{\hbar}}x$, and m is the reduced mass of the two atom system. The ground state vibrational wave function is then just a Gaussian with width $w_{gs} = \sqrt{\frac{\hbar}{m\omega}}$. Using $\hbar\omega \approx 700$ cm^{-1} in HfF^+, we get $w_{gs} = 5.3 \times 10^{-12}$ m or about $0.1a_o$. This gives a width for our photodissociation resonance of w_{pd} =4,200 cm^{-1}.

The cross-section at a given frequency is given by:

$$\sigma(\omega) = \frac{1}{4}\frac{g_2}{g_1}\lambda_{21}^2 g(\omega) A_{21} \tag{4.3}$$

where g_2 and g_1 are degeneracies of the upper and lower levels respectively and $g(\omega)$ is a lineshape function normalized such that $\int_{-\infty}^{\infty} g(\omega)d\omega = 1$.

Using

$$\mu_{21}^2 = A_{21}\frac{3\epsilon_0 hc^3}{2\omega_{21}^3} \tag{4.4}$$

this becomes

$$\sigma(\omega) = \frac{4\pi^3}{3}\frac{g_2}{g_1}\frac{g(\omega)\mu_{21}^2}{\epsilon_0 h\lambda_{21}} \tag{4.5}$$

if guessing a transition dipole moment is preferred to guessing a spontaneous decay lifetime. Now the assumptions come in. Assume λ_{21} =600 nm (more on this later). Looking at transition dipole moments from Petrov *et al.* [64], $\mu_{21} = 0.3$ a.u. seems like a conservative estimate. This is about the smallest μ_{21} for an allowed transition in HfF^+ that Petrov calculated. Note that this corresponds to a spontaneous lifetime of $\approx 1.2\mu$s. We assume that the full dipole moment is realized since all rotational and vibrational transitions will fall within the broad photodissociation resonance. We assume the degeneracy of the intermediate state and the repulsive curve are equal and set $\frac{g_2}{g_1} = 1$.

Using

$$\int_{-\infty}^{\infty} e^{-\frac{x^2}{2\mathrm{w}^2}}dx = \sqrt{2\pi\mathrm{w}^2} \tag{4.6}$$

we obtain

$$g(\omega_0) = \frac{1}{\sqrt{2\pi\mathrm{w}_{pd}^2}} \tag{4.7}$$

at the center of the resonance. This gives $\sigma(\omega_0) = 3.8 \times 10^{-19}$ cm^2. Note that this is an order of magnitude larger than the cross section for the predissociating CH^+ state used in our earlier experiment ($\sigma = 2.4 \times 10^{-20}$ cm^2 was the calculated cross section for the strongest line [81, 76, 77]).

Define a saturation pulse energy

$$E = \frac{hcA}{\lambda\sigma} \tag{4.8}$$

where A is the cross-sectional area of both the laser beam and ion cloud. Assuming a 100 mJ pulse at 600 nm, this gives 0.12 cm^2 as the area that can be saturated. This corresponds to a 1.9 mm beam radius. If the radius of the ion cloud needs to be decreased, it would only have to be done for a very short time, since the laser pulse is only 10 ns long, and heating of the ion cloud should not be a concern once the ions are dissociated. The focusing of the ions would have to be

done while still maintaining a well defined quantization axis. The 0.3 ea_0 transition dipole moment seems very conservative, as long as repulsive states exist. One could imagine that there would be many repulsive states with allowed transitions to the intermediate state within this broad 4000 cm^{-1} window, yielding a larger cross section.

If the dissociating pulse is at 600 nm, we would be able to use the higher pulse energy of the fundamental. However, this would require us to use an intermediate state that is very close to the dissociating limit, which might not be feasible. If you assume the pulse must be at a shorter λ, the saturation energy remains unchanged, but the available pulse energy would decrease by about a factor of four. If 532 nm (doubled Nd:YAG) light could be used for the dissociating photon, an order of magnitude more pulse energy would be available.

It seems the most likely scheme would involve a narrow cw laser operating on a transition that selects the spin using polarization. The second laser would probably have a wavelength longer than the first (decreasing the chance that we photodissociate without the first laser) and might be resonant with another intermediate state that then dissociates. Since the dissociation step is so broad the requirement on the second laser wavelength is mainly determined by the bound-bound resonance.

It seems possible that photodissociation to a repulsive curve could be used to read out the spin information in an efficient way in our experiment.

4.3 Light-Induced Heating

Another possible way of detecting our spin populations is to create a spin-dependent heating of our molecular ions. This was inspired by work on slowing molecular neutrals using a deep ($\approx$ 20 K) optical lattice potential. In the work from Ref. [83] molecules from a pulsed supersonic beam source interact with a travelling lattice potential given by,

$$U(z,t) = -\frac{2\alpha_a}{\epsilon_0 c}\sqrt{I_1(t)I_2(t)}\cos^2\left[\frac{1}{2}(k_L z - \delta\omega_{rel}t)\right] \tag{4.9}$$

where α_a is the effective polarizability, $I_1(t)$ and $I_2(t)$ are the intensities of two crossed laser beams, $\delta\omega_{rel}$ is the frequency difference between the two laser beams, and k_L is the lattice wavenumber given by $k_L = (4\pi \sin\phi)/\lambda$ with λ the mean laser wavelength on ϕ the half-angle between the two fields. Typical laser pulsewidths for high pulse energy Q-switched lasers used in these experiments are $\sim$ 10 ns. Molecular neutrals were created in a supersonic expansion beam and their initial velocity was slowed from 400 m/s to as low as 270 m/s, with the goal of producing slow cold molecules in the laboratory frame.

Our goals and approach differed from the above work. As will be discussed in Chapter 5, we built a laser ablation supersonic molecular beam source containing both ion and neutral molecules. We wished to use a deep one-dimensional optical lattice to read-out spin populations as well as to perform survey spectroscopy on molecular ions, with HfF^+ as our first target. As molecular ion densities in the beam were quite low compared to neutral densities of the above experiment, we used a much larger diameter laser beam (3 mm diameter vs 60 μm). The scheme was to shine the one-dimensional lattice perpendicular to the beam direction, and attempt to heat the low transverse temperatures of our molecular beam. This heating could be detected simply by using an imaging MCP detector (described in Chapter 3) and measuring the resulting increase in the ion beam width. The AC polarizability of the molecules is strongly frequency dependent near the region of a resonant transition. Scanning the laser wavelength across a transition will therefore show a frequency dependent ion heating and, if $\sigma^{\pm}$-polarized light is used, a potentially spin-state-dependent heating.

Eq. 4.9 is most useful far from resonance, were the polarizability α_a can be well approximated as constant. Close to a two-level resonance, the potential due to the dipole interaction of a standing wave is [84]

$$U_{\text{dip}} = \frac{1}{2}\delta\omega_L \ln\left(\frac{1 + \frac{8\Omega_R^2 \cos^2(k_L z)}{\gamma_n^2} + \left(\frac{2\delta\omega_L}{\gamma_n}\right)^2}{1 + \left(\frac{2\delta\omega_L}{\gamma_n}\right)^2}\right), \tag{4.10}$$

with Ω_R the on-resonance Rabi frequency of each of the standing wave laser beams, $\delta\omega_L$ the laser frequency detuning, and γ_n the natural linewidth of the excited state. The depth of the lattice

potential wells is then $U_l d = |U_{\rm dip}(k_L z = 0)|$. Fig. 4.4 shows the lattice depth in the limit of $\Omega_R \gg \gamma_n$ as a function of the dimensionless ratio $\delta\omega_L/\Omega_R$. The maximum lattice depth of $\approx 0.569 \times \Omega_R$ is at $\delta\omega_L/\Omega_R \approx 0.714$. As seen in the figure, the lattice depth peak is quite broad, with the half-maximum point occurring at a detuning of $\approx 3.2 \times \Omega_R$. The ion heating will depend not only on the lattice depth, but also on the initial ion beam temperature, the velocity of the ions in the direction of the lattice, and the ion's motional period in the trapping potential compared to the laser pulse time. If the trap period is ≈ 4 times the laser pulse length then maximum heating will occur. However, if the ions have an initial velocity such that they travel an appreciable fraction of a lattice wavenumber during the time of the ~ 10 ns pulse, the ion heating will be greatly reduced.

The fundamental advantage for spectroscopy is the large linewidths associated with the technique. Well depths on the order of a few Kelvin are reasonably achieved, making possible linewidths of the heating signal greater than 500 GHz. This is a nice feature when attempting to do survey spectroscopy over several thousand $\rm cm^{-1}$, which is the position we found ourselves in with *ab initio* calculations having uncertainties in this range for molecular ions containing heavy transition metals such as hafnium. The potential advantage for spin read-out is again the leveraging of high detection efficiencies for ions.

We chose to test this technique on Yb^+ ions as they posses a known transition we could easily access with the same frequency-doubled pulsed dye laser that was used for CH^+ dissociation studies and also since Yb^+ was easily produced in our laser-ablation supersonic-expansion source. A collimated Yb^+ ion beam was produced using two beam skimmers, with transverse temperatures < 500 mK observed. The ion beam was ≈ 17 cm long, while the laser beam diameter was 3 mm. In order to maximize the signal-to-noise ratio we gated the MCP voltage on for 1 μs and therefore needed precise timing in order to image the ions that had been subjected to the optical lattice potential. An ion lens was placed in the beam, just before the location of the lattice, in order to minimize the ion beam width on the MCP. This lens could also produce timing information by pulsing the lens on and noting at what time the minimum ion width was achieved. The timing resolution of this method was insufficient and instead we used two small "timing rods" with voltages

pulsed on to deflect the ion beam. Patch charges on these rods caused distortions in the transverse beam profile and the rods were therefore lowered out of the beam when heating data was taken. The dye laser beam was split into two beams that entered our vacuum chamber from opposite directions. This was done because of the short ($\sim$ 10 cm) coherence length of the laser. Placing a retro-reflecting mirror inside the vacuum chamber proved problematic as the laser pulse lead to a slight ionization of the mirror that distorted the ion beam. Fig. 4.5 shows results of Yb^+ heating when the optical lattice laser was tuned across the $^2S_{1/2} \rightarrow^2 P_{1/2}$ resonance at 369.4 nm.

Moving to molecular ions provided several challenges. The production of molecular ions such as HfF^+ in our beam source was accompanied by the creation of many other molecular and atomic species. In order to maximize our signal-to-noise ratio, we wished to separate out the HfF^+ ions in a way that left the transverse temperatures < 500 mK. This was accomplished by placing a large (9 cm diameter) plate electrode at a 45° angle to the ion beam and pulsing a positive voltage on this plate for ≈ 1 μs in order to deflect the ion beam 90° in a mass-dependent way into our imaging MCP. The experimental set up is shown in Fig. 4.6 and mass resolution using the 45° plate is shown in Fig. 4.7. This technique maintained the spatial profile of the ion beam along the direction of the optical lattice and beam temperatures of < 500 mK were maintained. Fig. 4.8 shows MCP images of a Yb^+ ion beam taken with this configuration.

Transition strengths are expected to be significantly lower in the case of HfF^+ compared to Yb^+, leading to smaller lattice well depths. The transition dipole moment for the $^2S_{1/2} \rightarrow^2 P_{1/2}$ transition in Yb^+ is 1.75 a.u. compared to the estimates for transition strengths in HfF^+ of 0.3-0.6 a.u. for transitions of interest from the ground $^1\Sigma$ state [64]. Transition strength is also spread across rotational and vibrational levels in molecules and many rotational levels are thermally populated in our molecular ion beam. Transitions from the thermally populated states that don't change the rotational quantum number, "Q-branch" transitions, will all fall comfortably within the power-broadened linewidth and therefore all ions should be exposed to the lattice potential as the laser frequency is scanned over Q-branch transitions. However, the transition strength will still be spread across all allowed rotational transitions, leading to an approximate factor of three decrease

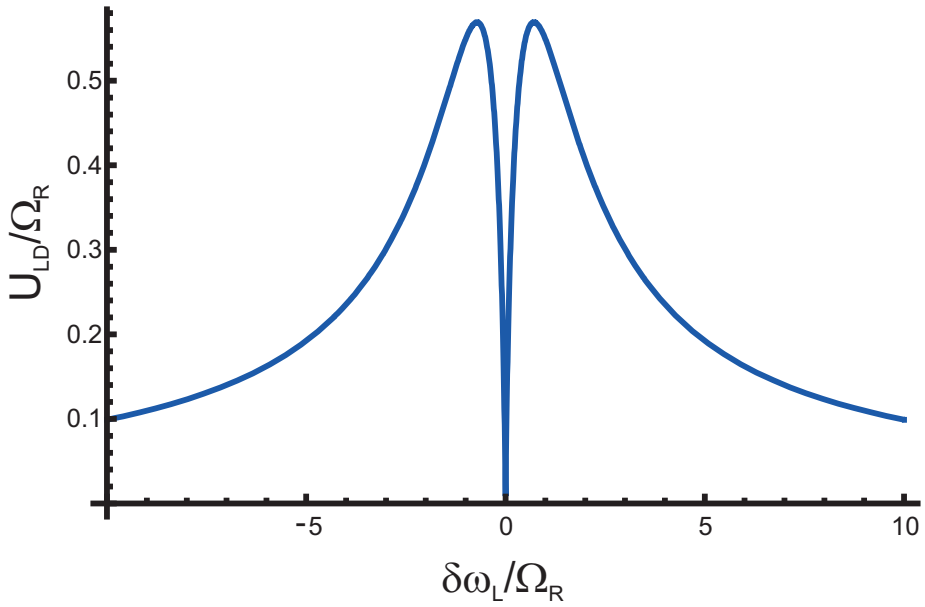

Figure 4.4: Lattice potential depth as a function of the laser detuning $\delta\omega_L$ divided by the on-resonance single beam Rabi frequency Ω_R, in the limit $\Omega_R \gg \gamma_n$, with γ_n the natural linewidth of the transition.

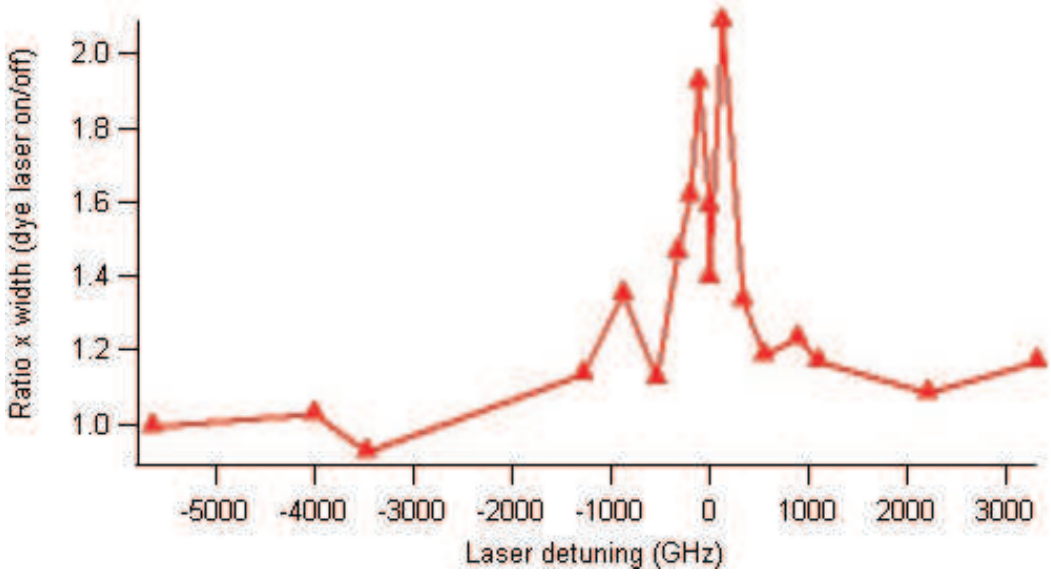

Figure 4.5: Data showing ion heating in a Yb^+ beam as the lattice laser was tuned over a Yb^+ resonance at 27,061.8 cm^{-1} (369.4 nm).

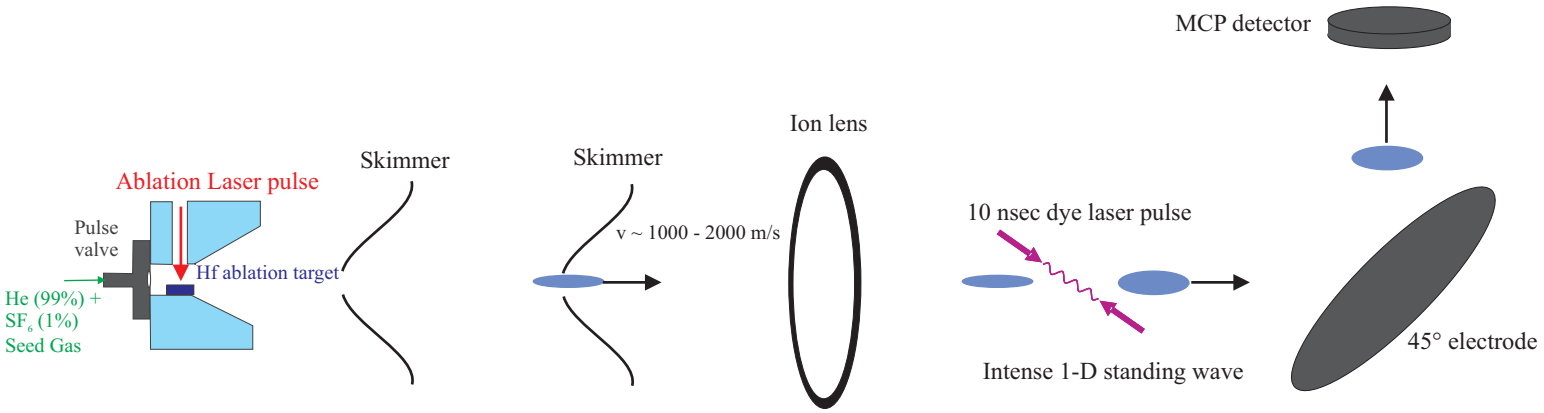

Figure 4.6: Experimental set-up for light-induced heating measurements. Ions are created using laser ablation of a metal target and are swept up in a supersonic expansion (more beam details are found in Chapter 5). The ions are collimated using two skimmers to transverse temperatures < 500 mK. An ion lens is used to minimize the beam width on the imaging MCP detector. An intense 1-D optical standing wave heats ions if the laser frequency is near an ion resonance. A 45° electrode is used to mass-select ions. The heated clouds are detected by an imaging MCP.

in transition strength, as well as a non-diagonal Franck-Condon matrix leading to at least a factor of two decrease in transition strength. It is possible all transitions for the low rotational states will fall under the FWHM of the lattice potential, retrieving some of this lost transition strength. The range we wished to scan in search of HfF^+ transitions was also at a factor of two longer wavelengths, making it more difficult to reach the regime were the lattice trap period is ≈ 4 times the laser pulse duration. The one advantage relative to the Yb^+ case is the laser pulse energy available in the visible wavelengths of interest for HfF^+ was ~ 10 times that available at the UV wavelengths of Yb^+, but this corresponds to only a factor of about 3 in the lattice depth. Certainly the molecular signal was expected to be weaker.

Obtaining a reliable signal, even in the much favored case of Yb^+, proved to be difficult. An ion beam temperature of 500 mK corresponds to an electric potential of only 40 μV. Small patch potentials on components inside the vacuum chamber were capable of wreaking havoc on our ion beams transverse profile. Also, the angle between the lattice laser and the ion beam was critical. If the angle between the two was greater than 5 mrad, the ions would traverse a full lattice spacing during the laser pulse, greatly reducing the signal. Aligning the laser beams to this accuracy is not a problem, but knowing the exact ion beam direction is difficult as small potential gradients will steer the beam. Given these issues we decided to abandon this approach, at least as a means of broad survey spectroscopy. However, performing similar experiments inside the ion trap would have certain advantages. Ion-laser overlap and timing issues would be mitigated. If used as a method of electron spin read-out the ions should have fewer rotational levels populated and a transition with a diagonal Franck-Condon matrix might be used. Another possible technique to salvage this method is to sympathetically cool the molecular ions with laser-cooled atomic ions. This should lead to large improvements in signal-to-noise.

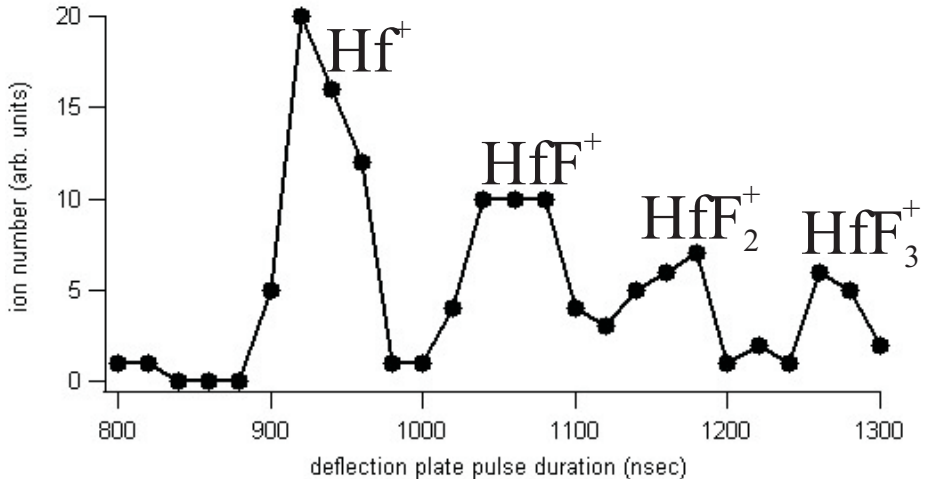

Figure 4.7: Mass spectrometry data using the 45° deflection plate showing the ability to seperate HfF^+ ions from Hf^+ and HfF_2^+. This was achieved while maintaining < 500 mK transverse beam temperatures.

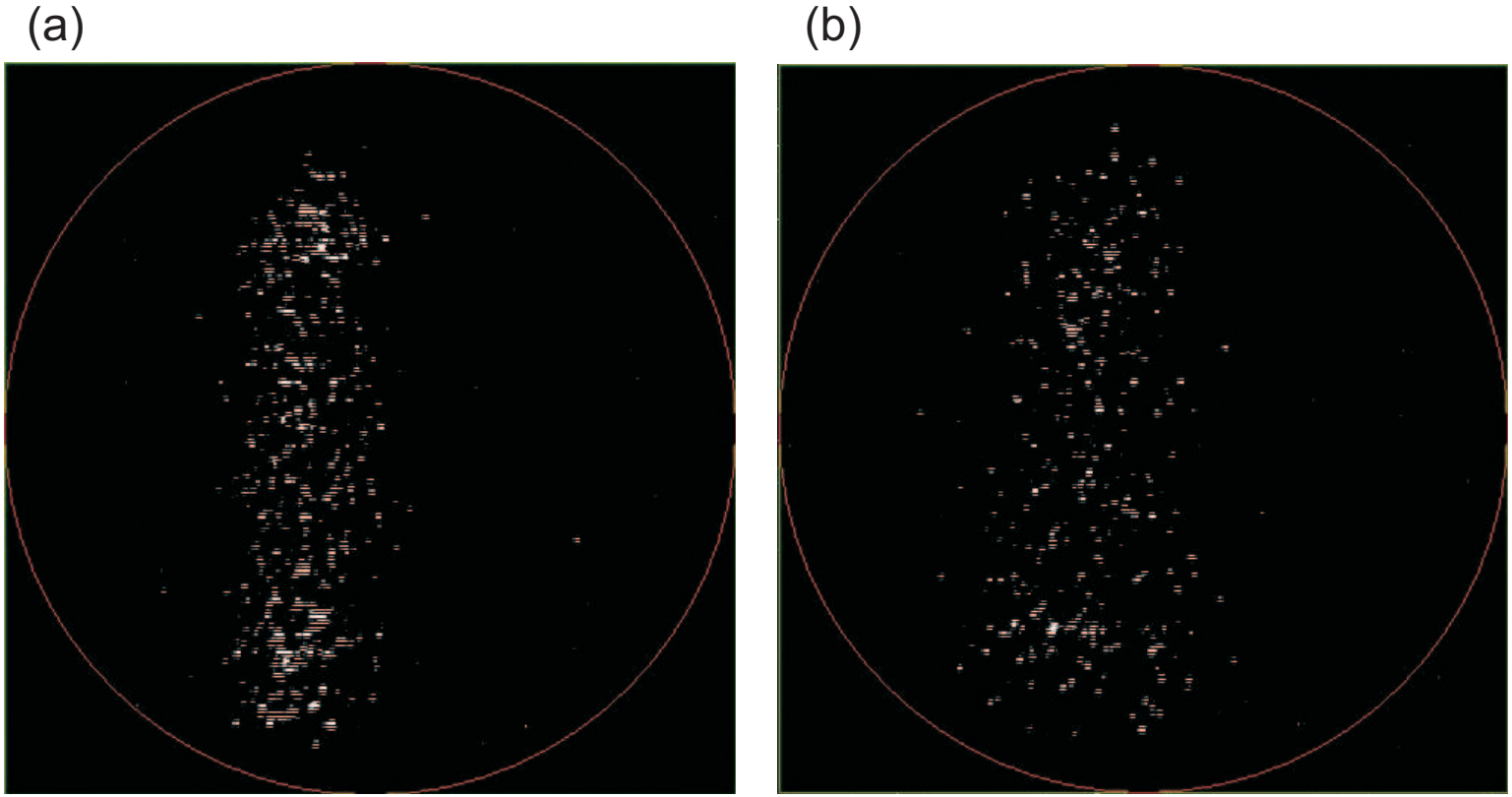

Figure 4.8: Data from the imaging MCP showing a Yb^+ cloud deflected by the mass-selecting 45° plate, with (a) the one-dimensional standing wave off, and (b) the one-dimensional standing wave applied on resonance, causing heating of the ion beam.

Chapter 5

Creation, Cooling, and Trap Loading of Ions

5.1 Ion Cooling Introduction

Our eEDM experiment requires cooling of both the internal (rotational, vibrational) and external degrees of freedom. Internal cooling is needed as we wish to perform the eEDM measurement on only a single ro-vibrational state and we must prepare the ions in only a single m_F-level before performing our measurement. Typical rotational constants of heavy metal fluorides are $\approx$ 0.3 cm^{-1}. This means 0.14% of ions will be in the ground rotational level at 300 K for an $\Omega = 0$ state and 0.43% for an $\Omega = 1$ state. Those percentages increase to 4% and 12% if the ions are rotationally cooled to 10 K (see Fig. 5.1). Working with the ground rotational level is preferable, as it provides the lowest number of m_F levels. If the molecular ions are created at 300 K, with internal and external degrees of freedom in equilibrium, we would expect the ions to occupy almost exclusively the vibrational ground state. Below we will see that is not always the case. Any ion not in the vibrational ground state will not be useful in our EDM measurement.

Low translational temperatures are important in order to maximize our electron spin coherence time. As discussed in Chapters 6 and 7, high ion temperatures can lead to decoherence through ion-ion collisions above a threshold momentum transfer, as well as from inhomogeneous Berry's phase contributions. Below we discuss several cooling schemes we explored; buffer-gas cooling, laser cooling, and supersonic expansion.

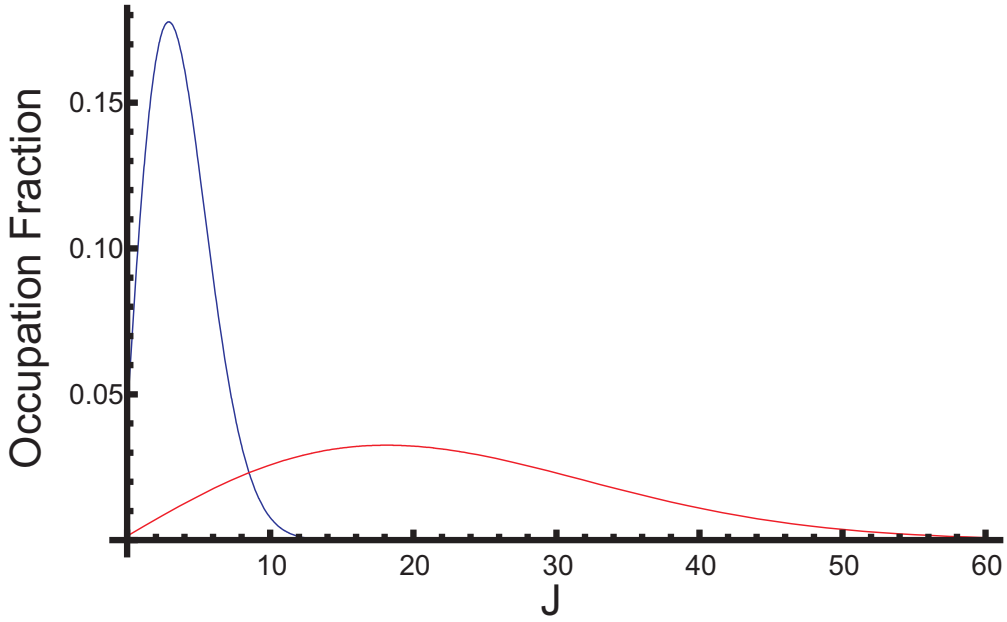

Figure 5.1: Occupation fraction for rotational states with quantum number J, for 300 K (red) and 10 K (blue) rotational temperatures given a typical fluoride rotational constant of $B_e = 0.3$ cm^{-1} in an $\Omega = 0$ state.

5.2 Buffer-Gas Cooling

Although buffer-gas cooling of neutral species is a relatively new field, with pioneering work from Doyle *et al.* [85], it has long been used as a means to cool trapped ions [86]. Trapping depths of thousands of Kelvin are relatively trivial to achieve in ion traps, therefore even room temperature buffer gas can provide dramatic cooling effects for trapped ions. Our initial attempts to demonstrate improved trap lifetimes and mass spectrometry resolution in our ion trap using room temperature helium buffer gas were unsuccessful due to contaminants in the helium. These contaminants were likely coming from the stainless steel tubing of our gas handling system. Once a liquid nitrogen cold trap was used to eliminate these contaminants, we were able to achieve improved trap lifetimes.

As discussed above, ion temperatures of 300 K still leave only a small portion of the molecular ions in the rotational ground state. Therefore, if buffer gas were to be utilized in our EDM measurement, helium cooled in an $\approx$ 4 K liquid helium dewar, or a dilution refrigerator, would be employed. While this scheme would cool both the internal and external degrees of freedom to sufficiently cold temperatures, there are potential issues. Neutral-ion collisions during the Ramsey resonance portion of the experiment would destroy our spin coherence, due to inelastic collisions changing magnetic and rotational levels. Even in the absence of inelastic collision, elastic collisions occurring while $\mathcal{E}_{\mathrm{rot}}$ is applied would have a characteristic energy of $\mathrm{E_{rot}}$, 1800 K for typical experimental parameters listed in Appendix A.

For the above reasons, the ions would have to be cooled in a relatively high pressure of helium and then either moved into a low pressure region, or the helium must be removed, before $\mathcal{E}_{\mathrm{rot}}$ could be applied and the spin resonance performed. The ions are easily moved from one trapping region to another through the use of electric fields. This has been demonstrated [87] on trapped ions for quantum information applications with heating as low as a few quanta ($\sim$ 1 mK). However, in our case differential pumping would require the ions to travel through a small aperture. Patch charges on this aperture, combined with the rf trapping fields, would likely lead to significant heating and ion loss. Quickly removing buffer gas at cryogenic temperatures has been demonstrated [88]. However,

the minimum helium pressure, due to desorption of helium from the cell walls, was measured to be $4.5\times\ 10^8$ cm^{-3}, a value that will likely be problematic (see Chapter 7.2).

5.3 Laser Cooling

Direct laser cooling of molecules is complicated by the added degrees of freedom involved, specifically rotation and vibration. There are several proposals for laser cooling of diatomic molecules [89, 90, 91, 92, 93] but they typically require very diagonal Franck-Condon matrices or complicated cooling schemes. As seen in Chapter 2.2, we already have many constraints in choosing a molecule which discourages us from also adding an extremely diagonal Frank-Condon matrix to that list. Even if possible, direct laser cooling of our molecules would be a significant technical challenge.

Sympathetic cooling with laser-cooled atomic ions has been used for cooling both atomic [94] and molecular [95] ions. The long range nature of ion-ion collisions cool the translational degrees of freedom very well, but the internal states will not be cooled. This has been experimentally verified in Ref. [96], with differences between translational and rotational temperatures of > 2 orders of magnitude, consistent with a zero coupling between the two.

Sympathetic cooling by overlapping laser cooled neutral atoms with trapped molecular ions should cool both the internal and external degrees of freedom. However, charge exchange collisions between the atomic neutrals and molecular ions would destroy ion trapping times. Hudson [97] has proposed to circumvent this problem by selecting molecular ions whose neutral species possess lower ionization potential than the laser-cooled atomic neutrals. This should mitigate the problem of charge exchange collisions. We have measured the ionization potential of HfF to be 59,458 cm^{-1}, higher than most atomic species that are available for laser cooling. Potentially Mg (IP = 75,000 cm^{-1}) or Be (IP = 61,000 cm^{-1}) could be used to cool HfF^+ but these are difficult atoms to laser cool. Also, other reactions beyond simple charge exchange might occur. Again, the large number of requirements on our molecule selection (Chapter 2.2) precludes us from choosing a molecule that would be more amenable to this technique.

5.4 Supersonic Expansion

Molecular-beam experiments are often carried out through the use of supersonic expansions. A reservoir of gas at high pressure, P_0, is separated from a region of lower base pressure P_b, with a small nozzle connecting the two. If the pressure ratio exceeds a critical value, $G \equiv ((\gamma_{\rm SH} + 1)/2)^{\gamma_{\rm SH}/(\gamma_{\rm SH}-1)}$, the mean velocity of the gas exiting the high pressure region will reach the local speed of sound. Here $\gamma_{\rm SH}$ is the ratio of the gas's specific heats of constant pressure and volume. For the noble gases $\gamma_{\rm SH} = 5/3$ and G ≈ 2.05. In the case of $P_0/P_b > G$ the exit pressure at the nozzle will be $P_0/G \approx 1/2P_0$ and the gas will continue to expand. As it expands, the beam velocity will exceed the local speed of sound and downstream of the nozzle shockwaves can occur since the expanding gas is moving faster than information about it can be propagated to the surrounding gas. The distance from the nozzle to the first shockwave is approximately $0.67(P_0/P_b)^1/2$d, with d the nozzle diameter. In modern beams the base pressure is often quite low and the transition from continuum to free-molecular flow is often smooth, without shockwaves present. In our case the distance from the nozzle to the shockwave would be on order 50 meters, much larger than the dimensions of our experiment.

The final velocity can be approximated, for the case of an ideal gas, from energy conservation arguments [98]. For a flow driven by a pressure gradient, the first law of thermodynamics takes the form, $h + {\rm v}^2/2 = h_0$, with h and h_0 being the enthalpy per unit mass of the expanded and initial gas respectively and v the velocity of the expanded gas. Using the relation $dh/dt = C_p$ the velocity can be related to the temperature of the gas,

$$ {\rm v}^2 = 2(h - h_0) = 2\int_T^{T_0} C_p dT \tag{5.1} $$

If C_p can be approximated as constant over the integration, and using the relationship for an ideal gas $C_p = (\gamma_{\rm SH}/(\gamma_{\rm SH} - 1)(R/M)$, with R the universal gas constant, we obtain,

$$ {\rm v_f}(T_{\rm f}) = \sqrt{\frac{2R}{M}\left(\frac{\gamma_{\rm SH}}{\gamma_{\rm SH}-1}\right)(T_0 - T_{\rm f})} \tag{5.2} $$

If there is significant cooling of the gas, the final velocity approaches a limiting value, and higher

initial pressures have very little effect on the final beam velocity. When dealing with a mixture of gases the molar average molecular mass and molar average heat capacity can be used.

The final beam velocity scales as $\sqrt{T_0/M}$, meaning lower beam velocities can be achieved with heavier expansion gases and by cooling the gas reservoir. This is often done in stark decelleration experiments, since much effort is required in order to slow the beam to rest in the lab frame. In comparison, the slowing of molecular ions is trivial as one needs only to apply a modest uniform electric field to the ions in order to stop them. Our choice of expansion gas was therefore dominated by other considerations. In early experiments with trapped atomic ions such as Hf^+, the largest numbers of ions that could be loaded into our trap was achieved using xenon. However, heavier noble gases have the disadvantage of higher polarizabilities that can lead to clusters. Evidence of clusters is seen in Fig. 5.2 where mass spectroscopy reveals strong signals at mass-to-charge ratios corresponding to $NiXe^+$ and Ni_2Xe^+ when nickel ions were introduced into a Xe expansion via ablation. Also, we tended to achieve better rotational cooling using neon and argon as they better matched the reduced mass of our diatomic fluorides.

5.5 Laser Ablation and HV Discharge

An eEDM search generally requires atoms or molecules with unpaired electron spins. The presence of unpaired electron spins make these free-radicals highly reactive. Due to this high reactivity, free radicals must typically first be produced in an experiment before studying them. Two typical approaches are laser ablation and high-voltage discharge. During the course of this work we briefly explored both techniques. A solenoid pulsed valve (General Valve Series 99) was used with an 800 μm opening. Connected to the face plate of the valve was a holder for the "target" metal rod as well as an opening for either a stainless steel electrode for discharge studies or for an ablation laser beam (Fig. 5.3). An expansion cone followed with a 40° full opening angle. As an alternative to the solenoid valve, a home-built valve utilizing a piezo-electric transducer was also used. A schematic of the design can be found in Ref. [99]. These valves seem to be preferred in JILA Stark deceleration experiments [100], with claims of greater pulse-to-pulse and long-term

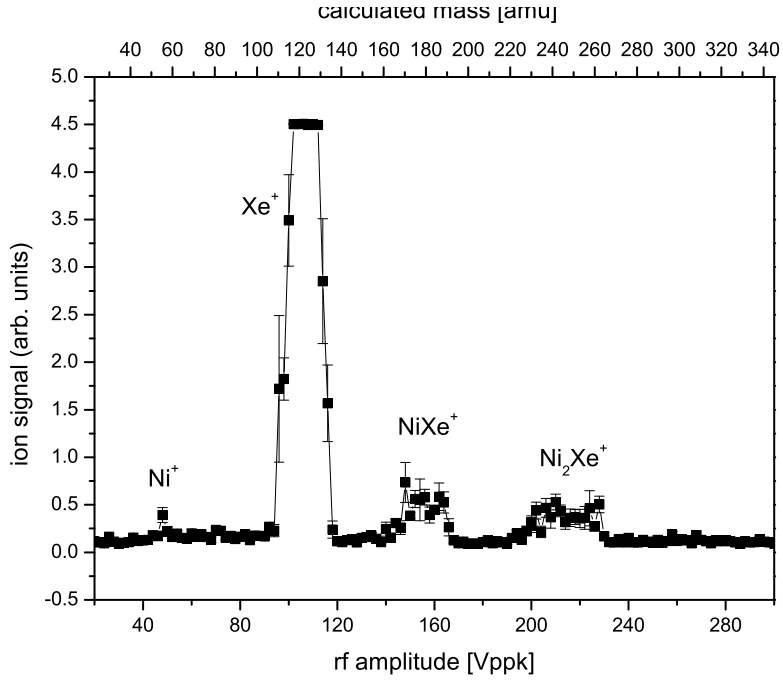

Figure 5.2: Mass spectrum of ablation products from a nickel target in a xenon expansion. Clustering occurs when a Xe atom attaches itself to a Ni^+ or Ni_2^+ ion.

stability. We achieved similar results for both valves and preferred the solenoid valve due to its robustness, as a careless graduate student can easily break the PZT with excess tension. Unlike Stark deceleration experiments, our early experiments were not very sensitive to variations in beam velocities. This might explain the apparent discrepancy in valve preference. In future experiments, beam velocity fluctuations will likely be more important and another investigation of the PZT valve might be appropriate.

The pulsed valve was operated with several noble gases, He, Ne, Ar, and Xe, at backing pressures of 20-100 psig. A 200 μs, +200V pulse was typically sent to the solenoid valve. This was followed by either a laser ablation pulse focused on the metal target, or an electrical discharge between the metal target and stainless steel electrode. The discharge voltage was typically run at DC, with the increase in pressure from the pulsed valve firing acting as the discharge gate, since the higher pressure corresponded to a lower breakdown voltage. An Nd:YAG laser served as the ablation laser. This laser was capable of producing 50 mJ at 1064 nm in a 10 ns pulse, and was focused with a 50 cm focal length lens onto the ablation target to a 230 μm beam diameter corresponding to a 3.8 cm Rayleigh range.

The discharge or laser ablation pulse created both neutral and ionic atoms from the metal target. In order to produce diatomic molecular ions, gas containing hydrogen or fluorine was mixed with the noble gas backing the pulsed valve. We attempted to produce HfH using a mixture of 1% CH_4 with the balance being a noble gas, with the hope of seeing the following reactions,

$$\mathrm{Hf} + \mathrm{CH_4} \longrightarrow \mathrm{HfH} + \mathrm{CH_3}, \tag{5.3}$$

$$\mathrm{Hf^+} + \mathrm{CH_4} \longrightarrow \mathrm{HfH^+} + \mathrm{CH_3}. \tag{5.4}$$

Unfortunately, the bond energy of a hydrogen atom in CH_4 is 36,686 $\mathrm{cm^{-1}}$ compared to *ab initio* calculations that predict a bond energy of 22,000 $\mathrm{cm^{-1}}$ for HfH^+ [4]. Therefore, in order to efficiently produce the intended HfH^+ molecules, large amounts of hydrogen would have to be dissociated from CH_4 during the ablation or discharge process. The failure to produce these molecular species suggests large numbers of atomic hydrogen were not produced.

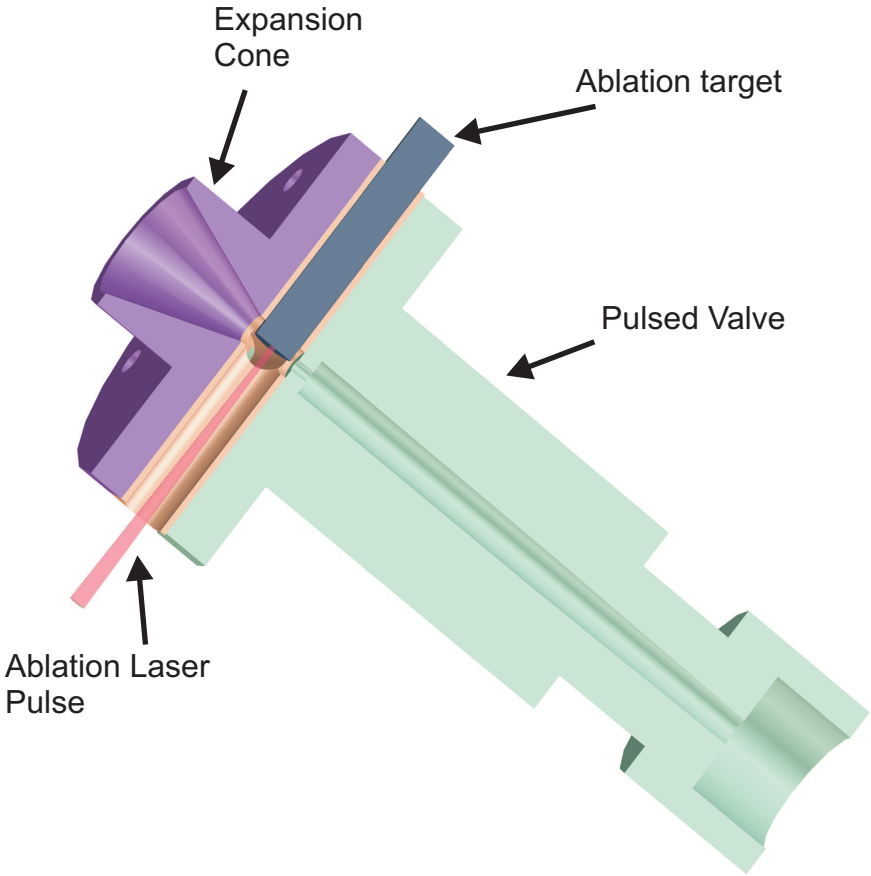

Figure 5.3: Diagram showing the pulsed valve set-up. An ablation target rod was held just outside the pulsed valve opening and was followed by an expansion cone with a 40° opening angle.

The bond energies of fluorine-containing diatomic molecules tends to be higher than those containing hydrogen, while the electronic structure is analogous. HfF has a measured bond energy of 53,966 cm^{-1} [101], and *ab initio* calculations predict a bond energy of 51,107cm^{-1} for HfF^+ [64], compared to a fluorine bond energy of 35,098 cm^{-1} in SF_6. Seeding our noble gas with 1% SF_6, we observed the following exothermic reactions, among others,

$$Hf + SF_6 \longrightarrow HfF + SF_5, \tag{5.5}$$

$$Hf^+ + SF_6 \longrightarrow HfF^+ + SF_5. \tag{5.6}$$

Laser ablation yielded better results for hafnium ion creation than the HV discharge and the discharge was quickly abandoned. The number of Hf^+ and HfF^+ ions created increased with increasing ablation laser energy up to the 50 mJ pulse energy maximum of our ablation laser. We also frequency doubled the ablation laser to 532 nm and obtained a maximum pulse energy of 25 mJ. The ion number achieved with 25 mJ of green light was equivalent to that obtained with 50 mJ of IR light so we chose to use IR light for the rest of our experiments. A larger ablation laser was used in order to look for a maximum in ion creation with ablation energy. The data in Fig 5.4 shows a maximum in Hf^+ ion creation at 135 mJ, and a maximum in HfF^+ ion creation at 200 mJ. In later experiments we were more concerned with maximizing the number of neutral HfF molecules, and we found a much lower optimum ablation energy (Fig. 5.5).

After many ablation pulses, large pits would form on the metal target and ion production would decrease. This required a vacuum break and the pitted end of the metal target would be removed. Highest ion numbers were achieved with a slightly rough metal target surface, and we preferred to use a hacksaw to produce a fresh, fairly rough surface. Often times researchers will use metal ablation targets that rotate and translate, leaving a fresh target surface. This was tried, but it was found that shot-to-shot number variations did not improve, at least in the case of ablating hafnium. Many different metals were used as ablation targets in our experiment, with hafnium yielding the best results for shot-to-shot stability and number of ablation pulses incident on the target before needing to saw the pitted end off. At 50 mJ ablation energies, hafnium targets would

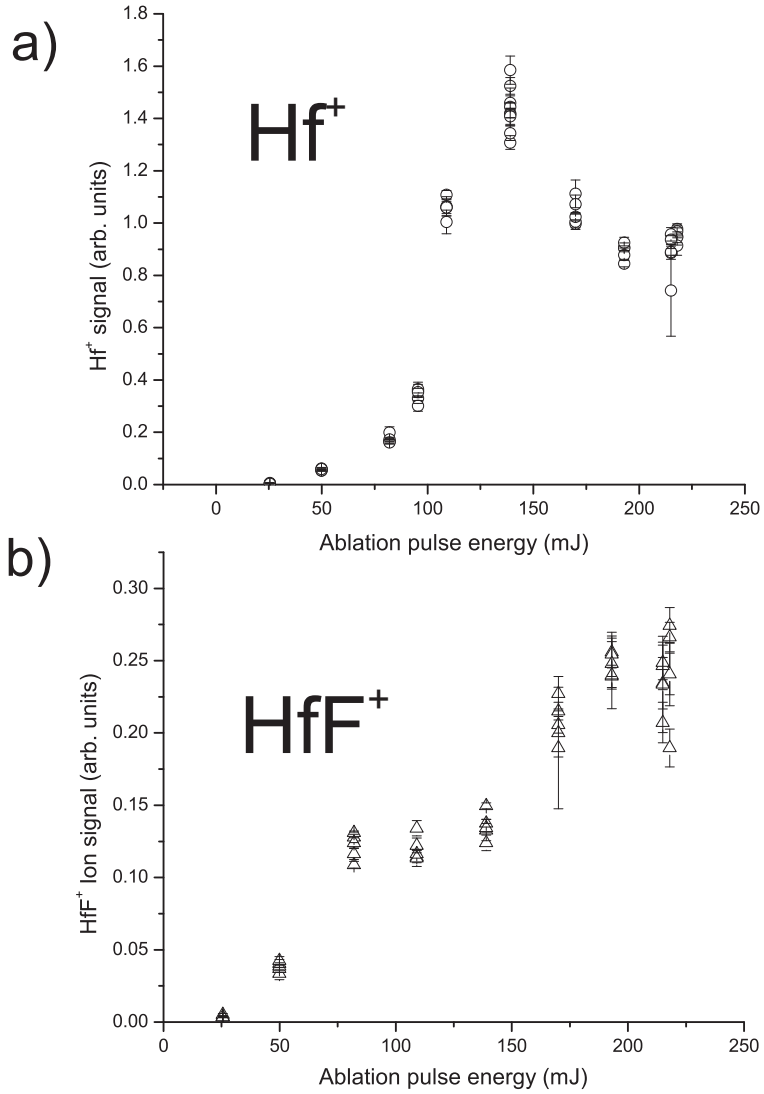

Figure 5.4: Number of a) Hf^+ and b) HfF^+ ions created, as a function of 1064nm laser ablation energy. The channeltron detector was operated at a lower than normal voltage (1,400 V here vs 2,000 V normally) in order to keep the detector response linear.

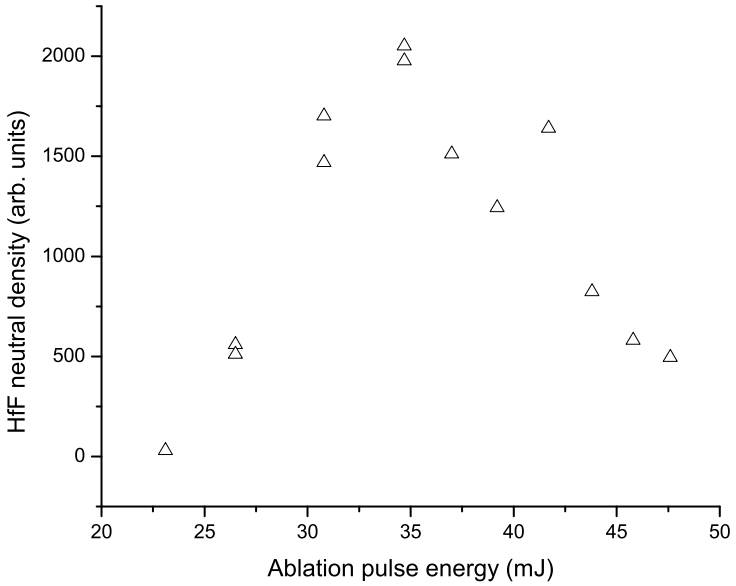

Figure 5.5: The density of HfF neutral molecules created in our molecular beam as a function of 1064 nm laser ablation energy. This data was obtained using photoionization techniques discussed in Chapter 5.7.3 to measure HfF density.

receive millions of ablation pulses before needing to be re-cut. Since our most recent experiments are done at lower pulse energies, even more ablation pulses are possible. Perhaps if thorium or another metal is used in the final experiment a rotating and translating target might become necessary.

5.6 Measuring Beam Temperatures

Collisions with the expansion gas will cool the molecular ions and neutrals created from the ablation process. As mentioned above, we care about cooling of not only the translational degrees of freedom, but also the rotational, vibrational, and electronic degrees of freedom. Below we discuss measurements made of our molecular beam using various methods.

5.6.1 Translational Temperatures

Some of the first measurements of our molecular beam were made using a commercial fast ion gauge (FIG). The FIG was mounted on a linear motion vacuum feedthrough such that it could be scanned across the beam, although it could only scan slightly past the centerline of the beam due to the finite travel of the feedthrough. The FIG is very similar to a traditional vacuum ion gauge, with the main differences being small filament-grid and grid-collector distances and fast electronics mounted to the device inside the vacuum chamber. The response time of the device is < 5 μs, with a sensitivity, 1×10^5 V/(Torr mA), that depends on the adjustable filament emission current.

Early experiments used a 2 mm diameter skimmer to separate the source chamber (a six-way cross with 6" CF flanges) from lower pressure chambers (also 6" six-way crosses) downstream. Differential pumping was employed via turbomolecular pumps attached to each chamber and backed by mechanical scroll pumps. These were used instead of oil diffusion pumps to reduce backstreaming of oil and other contaminants from the pumps into the vacuum chambers. The pulsed valve to skimmer distance was varied while using a channeltron to measure the Hf^+ ion number seen after the skimmer. The ion signal when the valve-to-skimmer distance was scanned showed a broad maximum after the separation was at least 5 cm. We operated most experiments with a pulsed valve to skimmer distance of ≈ 12 cm. The distance between the skimmer and the FIG was ≈ 18

cm. Since the beam is much larger than 2 mm in diameter as it reaches the skimmer, the skimmer position and diameter define an initial beam position and diameter. By measuring the width of the beam at a known distance from the skimmer, the transverse velocity spread can be calculated. Normally the FIG is used to measure neutral signals by ionizing gas from the filament and then collecting and counting those ions. However, if you turn on the detection electronics for the FIG while leaving the filament off, the instrument will be sensitive to ion signals only. Fig. 5.6 shows data taken in this way, for a beam of ions created through ablation of hafnium in the presence of a xenon expansion with 52 psig backing pressure. The data corresponds to a transverse temperature of the ion beam that is ~ 1 K. Similar temperatures were found for the neutral signal when the FIG filament was turned on.

Axial temperatures are more difficult to define and to measure in our beam. The gas pulse width was ~ 400 μs when measured at the FIG position 30 cm downstream from the pulsed valve. The axial velocity of a gas molecule should become strongly correlated to its axial position as the beam travels through the vacuum chamber. Axial temperature is perhaps less important than an axial velocity spread within a given axial slice of the beam. This was measured indirectly when time-of-flight mass spectroscopy was performed as described in Chapter 5.7.3. Simulations of our TOFMS put an upper limit of 20 m/s velocity spread in our beam over a 3 mm axial slice of the cloud, "measured" at a distance of 60 cm after the pulsed valve.

5.6.2 Laser-Induced Fluorescence in the Beam

In hopes of measuring HfF^+ spectrum, laser-induced fluorescence was performed on the molecular beam using the set-up shown in Fig. 5.7. The vacuum chamber after the first skimmer was painted with a vacuum compatible black paint and light baffles with imaging optics integrated into them were installed between the chamber center and a photomultiplier tube (PMT) detector that sat underneath the chamber. Lasers could pass through the center via two long arms mounted to the vacuum chamber with Brewster windows attached and containing baffles to reduce scattered light. Data could be recorded in pulse-counting mode or, for larger signals, in analog mode. For

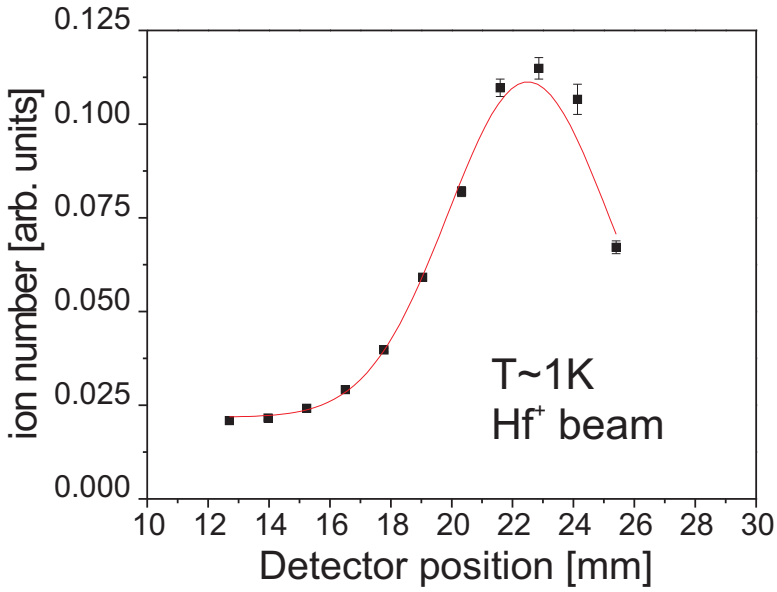

Figure 5.6: FIG data taken with the filament turned off, making the device only sensitive to ions. This data was taken with Hf^+ ions in a xenon expansion and corresponds to an ion beam temperature of approximately 1 K.

large amplitude signals, a transimpedance amplifier was used to reduce PMT saturation effects.

Two different laser systems were generally used. One was a pulsed dye laser, capable of operating throughout the visible and near-IR wavelength ranges. Frequency doubled light could be obtained through simple single-pass frequency doubling with BBO or KTP crystals, depending on the specific operating wavelength. The laser produced 10 ns pulsewidths with typical linewidths less than 0.1 cm^{-1}. Maximum pulse energy was dependent on wavelength but was generally 50-300 mJ in the fundamental and 5-50 mJ of frequency-doubled light. A cw Ti:Saphire ring laser, with a specified linewidth of 100 kHz, was also used. This laser was capable of > 4 W at 800 nm, the center of the gain curve. The laser's tunable range, through the use of three different output couplers, extended from 700 - 1030 nm.

When the pulsed laser was used, we gated the PMT detector on using JILA built electronics in order to limit scattered light backgrounds and PMT "after-pulsing". After-pulsing occurs when positive ions are created due to electron impact ionization of residual gas inside the PMT. These ions are accelerated upstream in the PMT and eventually collide with an electrode, creating electrons that imitate photoelectrons. Delay times between firing the laser and gating the detector were between 150 and 650 ns and the gate was left on for up to 20 μs, though usually useful signal was only obtained for shorter times due to the molecules travelling outside the imaging region of our optics or electronic decay of the molecules. After-pulsing was suppressed by a factor of ~ 40 using the gating circuit. The ultimate limit to light background was dominated by an unknown source of scattered light from the molecular beam. This scattered light background was approximately constant over entire laser dye curves ($\sim$ 30 nm), and only appeared when the LIF laser, ablation laser, and pulsed valve were all operated. Typical background count rates were 4 photons/shot in a 5 μs counting window with a 3 mJ laser pulse and a 150 ns delay between firing the laser and gating on the PMT. Background rates using the cw Ti:Saphire laser were never an issue, which had the advantage that the fluence needed to saturate the transition is lowered by (3 GHz)/(0.05 GHz), the ratio of the pulsed laser linewidth to the typical Doppler-broadened linewidth in our beam. However, the cw laser was not very useful in looking for unknown HfF^+ transitions as step

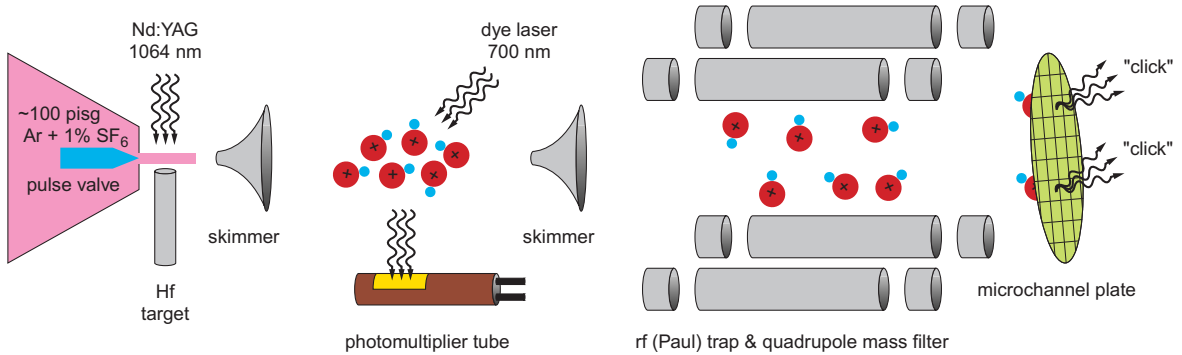

Figure 5.7: Experimental setup. Laser ablation of a metal Hf target creates neutral Hf atoms and Hf^+ ions that react with SF_6 to produce neutral HfF molecules and HfF^+ molecular ions, respectively (Eqns. 5.5 and 5.6). The molecules (both neutral and ionic) are cooled in a supersonic expansion with an Ar buffer gas. The molecular beam is illuminated with a pulsed dye laser beam and the resulting fluorescence is collected with a photomultiplier tube (PMT) yielding laser induced fluorescence (LIF) spectra (Fig. 5.9). At the end of the beamline, the ions can be loaded into an rf Paul trap where the electron spin resonance experiment will be performed. The Paul trap also acts as a quadrupole mass filter and ions of a particular mass/charge ratio are detected with a microchannel plate (MCP) (Fig. 3.10). Additionally, the spatial resolution of the MCP allows for the temperature of the ion cloud to be determined from the detected cloud size.

sizes of 50 MHz would be necessary and the uncertainty in the position of the transitions was on order of 1,000 cm^{-1}.

The first transitions seen in the supersonic beam were neutral atomic hafnium transitions. The ground state of neutral hafnium has $^3F_2$ symmetry with $J = 3$ and $J = 4$ excited states at 2,357 and 4,568 cm^{-1} respectively. Transitions were seen not only from the $J = 2$ ground state, but also from excited fine-structure states. Fig. 5.8 shows LIF data taken for the $^3F_2 \rightarrow {}^3D_1$ transition using the cw Ti:Saph laser for excitation. Similar data on the $^3F_4 \rightarrow {}^3D_3$ transition showed a population ratio of ~ 500. If the fine-structure distribution was in thermal equilibrium with the translational degree of freedom we would expect a ratio of 10^{286}, given the <10K translational temperatures observed in the supersonic beam.

Previously unmeasured transitions in neutral HfF were also detected in the beam, and these allowed us to measure the rotational and vibrational temperatures, although the rotational and vibrational temperatures of HfF^+ could be significantly different due to the different collisional cross sections involved. HfF is known to have a $^2\Delta_{3/2}$ ground electronic level, and transitions to $\Omega = 1/2$ and $\Omega = 3/2$ states were found. The transitions were fit using the same effective Hamiltonians as used in Ref. [6],

$$H = T + B_e[J(J+1) - \Omega^2] - D[J(J+1) - \Omega^2]^2 \tag{5.7}$$

was used for states of $\Omega = 3/2$ character, with B_e the rotational constant, T the band origin, and D a constant characterizing the effect of centrifugal distortion on rotation. Excited states showing Σ character were fit using,

$$H_a = T + B_e N(N+1) - D[N(N+1)]^2 - \frac{\gamma_s}{2}[N+1] \tag{5.8}$$

$$H_b = T + B_e N(N+1) - D[N(N+1)]^2 + \frac{\gamma_s}{2}N, \tag{5.9}$$

with N the rotational quantum number, γ_s a doubling constant, and where a and b denote states of different parity. States that demonstrated $^2\Pi_{1/2}$ character were fit to,

$$H_{a/b} = T + B_e(J+\frac{1}{2})^2 - D\left(J+\frac{1}{2}\right)^4 \mp \frac{1}{2}(p+2q)\left(J+\frac{1}{2}\right), \tag{5.10}$$

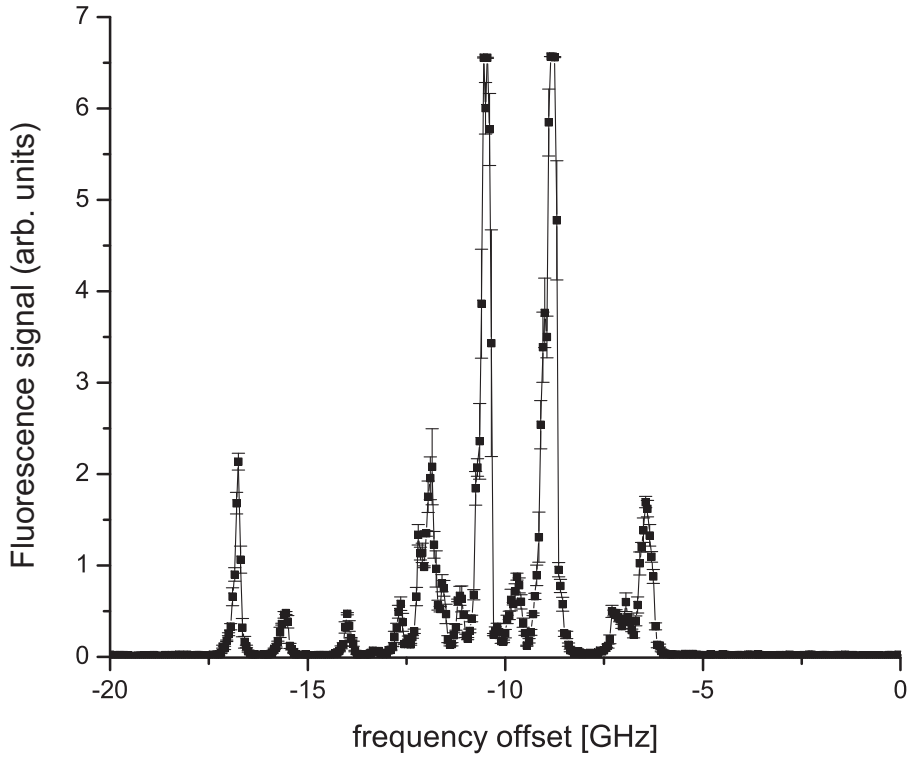

Figure 5.8: LIF data taken with a cw Ti:Saph laser showing hyperfine structure in the $^3F_2 \rightarrow {}^3D_1$ transition of hafnium. Similar data was taken of the $^3F_4 \rightarrow {}^3D_3$ transition as the fine structure was not completely cooled in the supersonic expansion.

with 1/2(p + 2q) a constant describing the Λ-doublet splitting. We typically set D to zero as most of our data involved only low rotational states where the energy term from non-zero D was much smaller than our experimental resolution. The resolution was determined by the laser linewidth and was approximately 0.1 cm^{-1}. Nonlinear least-squares fitting routines were used.

Through the examination of "missing" lines around the band origin, assignments of Ω could be made. In order to find rotational temperatures, the rotational line intensities were fit to the partition function and Hönl-London factors. The typical value of the rotational temperature was 10 K. Several states were found that appeared to be different vibrational transitions between the same electronic states. To test this we carefully fit the rotational lines as follows. First, rotational lines in the "P-branch" (δJ = -1 transitions) and "R-branch" (δJ = +1 transitions) were fit to Lorentzian line shapes, with the peak intensities allowed to float. The "Q-branch" (δJ = 0 transitions) lines were excluded as the resolution was insufficient to resolve them. The line positions were then fit to the model Hamiltonian to determine a value for the ground and excited state B_e. Preliminary assignments of some of these lines are shown in Fig. 5.10, where two electronic states appear to be responsible for eight rotational bands. It appears that vibrational levels are not in thermal equilibrium with the translational and rotational temperatures, as transitions from $v'' = 2$ are observed.

5.7 Loading Ions Into the rf Trap

Our experimental count rate will be limited by space charge effects of the trapped ions. Therefore, any ions trapped that are not used in measuring the eEDM limit the statistical sensitivity of our measurement. In order to maximize our count rate, we would ideally create and trap only HfF^+ ions of a single Hf isotope and in a single internal quantum state. Fig. 5.11 shows a mass spectrum of ions loaded from the laser-ablation supersonic-expansion source into the ion trap. As seen in the figure, many ion species are created, from SF^+ to HfF_3^+ and perhaps beyond as the range of mass-to-charge ratios we were able to trap was limited.

The ions created during the ablation process populate many rotational and magnetic sub-

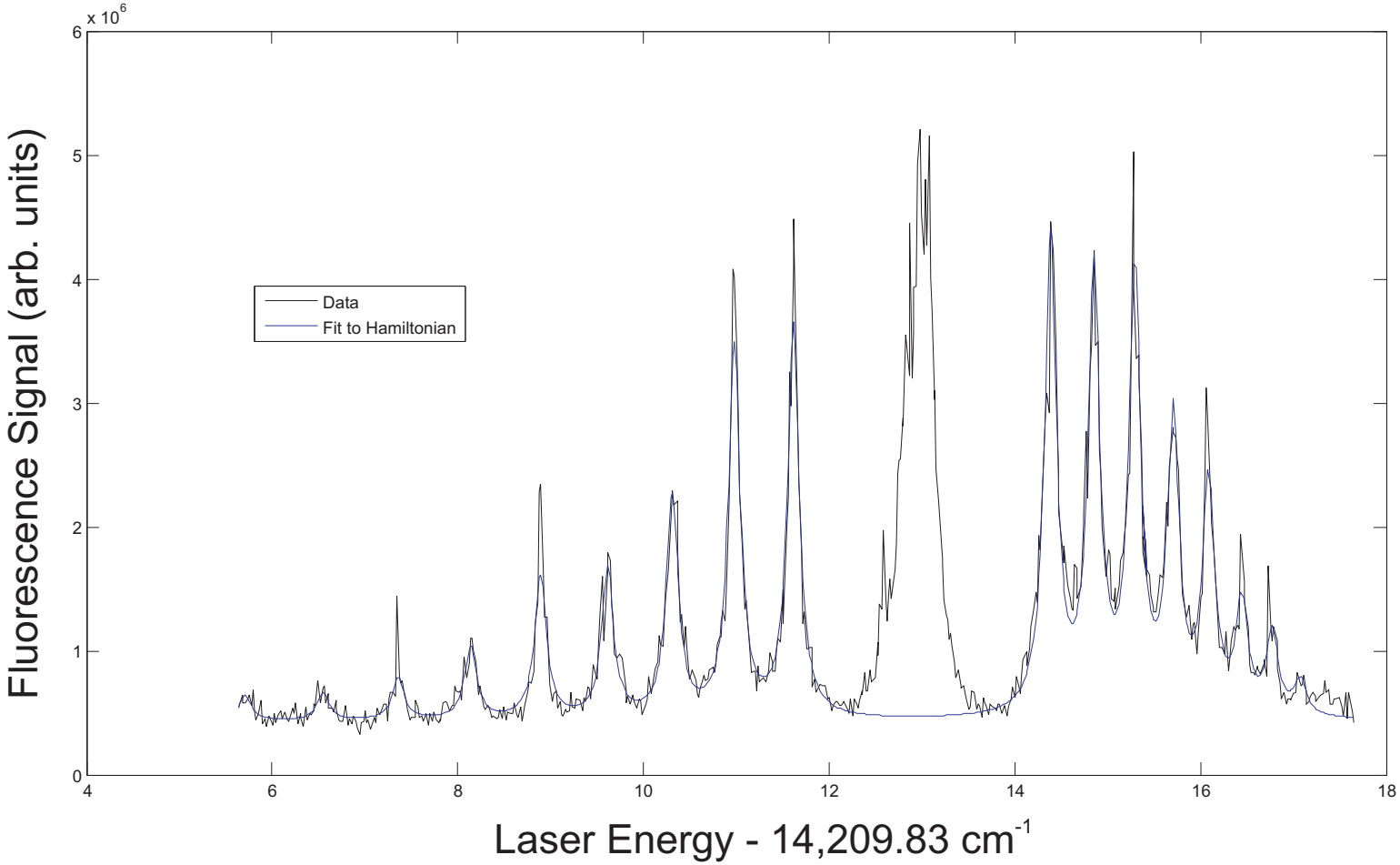

Figure 5.9: Data from an $\Omega = 3/2 \rightarrow 3/2$ transition in HfF. The smooth curve is the fit obtained while ignoring the unresolved Q-branch lines in the 12-14 cm^{-1} region of this graph. Small differences in the rotational constant B_e allowed us to ascribe vibrational states to the levels involved.

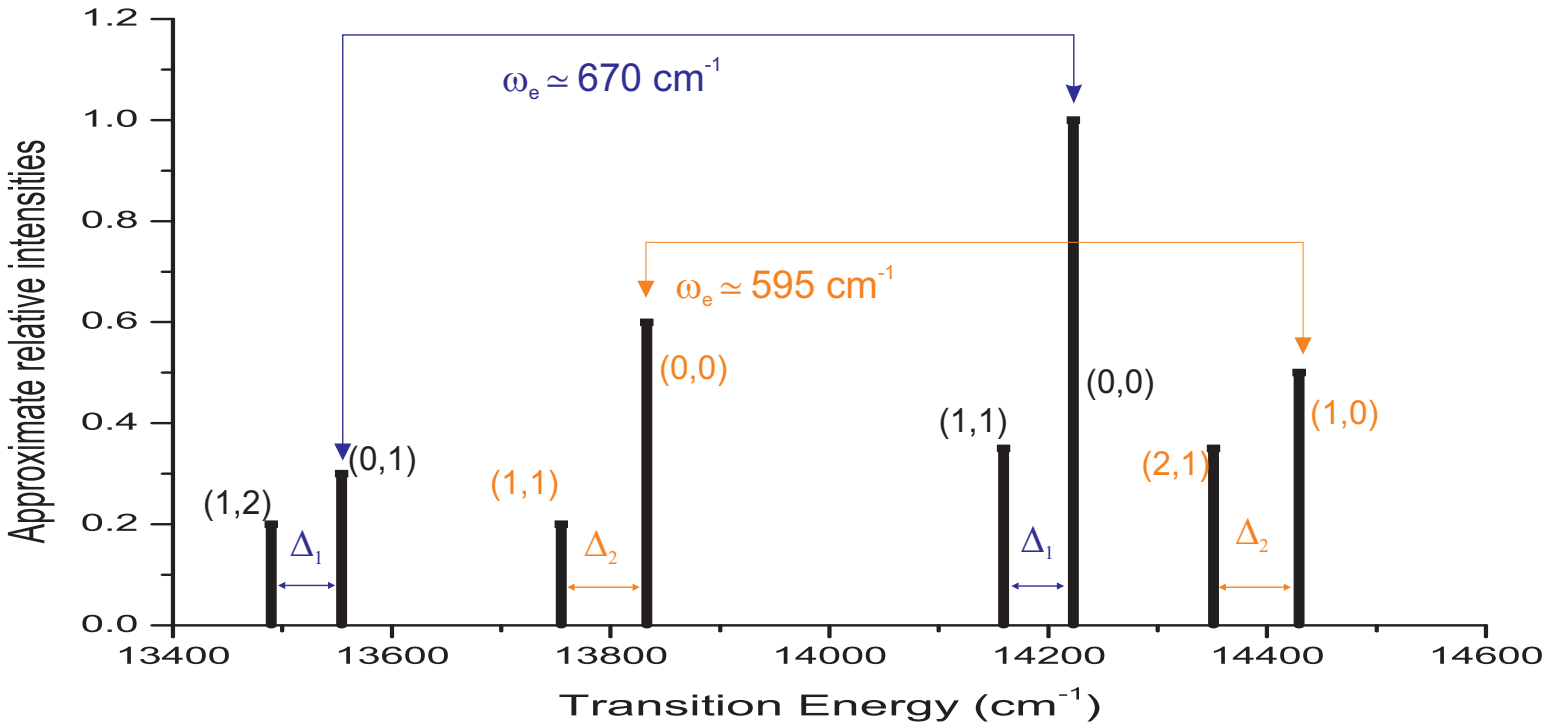

Figure 5.10: Schematic of HfF transitions seen from LIF in our molecular beam showing approximate relative intensities. Lines connected by blue(orange) arrows are believed to be different vibrational transitions between the same $\Omega = 3/2(1/2)$ electronic levels, as suggested by slight differences in B'_e and B''_e, the rotational constants in the upper and lower states respectively. Preliminary vibrational assignments are given as (v',v''), again with the $'('')$ denoting the upper(lower) state. The ground-state vibrational spacing ω_e is measured to be 670 cm^{-1}, consistent with a previous measurement [6], while an excited electronic state has a measured ω_e of 595 cm^{-1}.

levels. Above thermal population of excited electronic levels, such as the $^3\Delta_1$ state in which our eEDM experiment will be performed, might also be present as the supersonic expansion cooling of these levels might be less than complete. However, the likelihood of significant population of the $^3\Delta_1$ level surviving the expansion seems unlikely. It is therefore necessary to find another method to populate our $^3\Delta_1$ "science" level. One potential method is a two-photon stimulated Raman adiabatic passage or STIRAP, utilizing as the intermediate state a spin-orbit mixed $\Omega = 1$ state such as the b(1) and c(1) states of Fig. 2.2.

Theoretical predictions [64] indicate the transition dipole moments should be on the order of 0.3 a.u. for transitions to the $^1\Sigma$ ($^3\Delta_1$) level while the transition dipole moment to the $^3\Delta_1$ ($^1\Sigma$) should be 0.03 a.u., with which transition is stronger depending on which intermediate $\Omega = 1$ state is chosen. The transition strength will be decreased when vibrational and rotational wavefunction overlap is taken into account. Since the ion cloud diameter will be $\sim$ 1 cm, the large laser power necessary for efficient STIRAP with cw lasers will be impractical for these transition strengths. When performing STIRAP using pulsed laser sources, laser bandwidths that are transform-limited yield the minimum required pulse energies. The minimum pulse energy required scales as the square of the ratio of the laser bandwidth to the transform-limited bandwidth [102]. With our HfF^+ states, in the ideal case of a transform-limited pulse, a 10 ns pulse of at least 100 μJ would be required for the weaker of the two transitions involved in the SITRAP. If a pulsed dye laser with a 0.1 cm^{-1} bandwidth is used, the minimum requirement would be $\sim$ 1 J laser pulses.

5.7.1 Ion Lens

As shown in Chapter 3, it is possible to mass-selectively remove ions from our trap by operating at certain a and q trapping parameters. The issue with this approach is that heating of the desired ions tends to occur due to the proximity to the $\beta = 1$ contour of the stability diagram. A potential solution to this is inserting a quadrupole ion lens along the beam path, between the source chamber and the ion trap. As shown in Eqn. 3.13, the lowest order frequencies of ion motion in an rf quadrupole at rf drive frequency Ω_{rf} will be $\omega_{sec} \equiv \beta\Omega_{\mathrm{rf}}/2$, $\Omega_{\mathrm{rf}} - \omega_{sec}$, and $\Omega_{\mathrm{rf}} + \omega_{sec}$. If

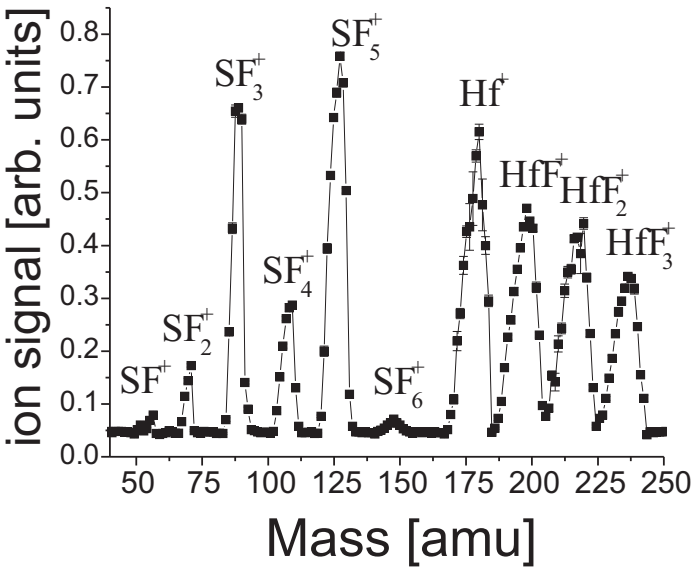

Figure 5.11: Mass spectrum of ions created in laser-ablation supersonic-expansion with a hafnium ablation target and an expansion gas of 1% SF_6 in 99% He. The ion number is a non-linear function of the y-axis value, but a level of 0.4 corresponds to $\sim$ 100,000 ions.

these three frequencies are made to be commensurate for ions of a desired mass-to-charge ratio, and the rf is applied for an integer number of secular periods, the desired ions will be imaged from one end of the lens to the other, while ions of different mass-to-charge ratios will undergo defocusing. If a small aperture is placed between the lens and the ion trap, the desired ions might be separated from the ion ablation soup. Fig. 5.12 shows the frequency spectrum of ion motion at certain values of a and q where our lens conditions are met, as well as results of a numerical simulation of ion motion under these conditions for two different ion masses. The radial velocity change the ions will experience is proportional to $q\Omega_{\mathrm{rf}}R_i|\frac{\delta M}{M}|$ with R_i the initial radial displacement from the center of the lens and δM is the mass difference from the ions that are imaged by the lens.

The ion lens was constructed with solid stainless-steel electrodes of 25 mm radius and spacing $2r_0 = 21.8$ mm, *i.e.* the identical radial dimensions of our first ion trap. Two of the electrodes were grounded by mounting them directly to a vacuum flange with the first skimmer being mounted on the opposite face of this flange. The other two electrodes were attached to similar drive electronics as those described in Chapter 3.6.

We operated the lens over a range of parameters, but satisfactory separation of different massed ions was not achieved. It was discovered that the ion cloud after the first skimmer was best described not as free ions, but rather as being one component of an overall neutral plasma. Experimental evidence of this came from placing electrode plates, parallel to and straddling the molecular beam, after the first skimmer and measuring the ion deflection caused by a potential difference between the plates. Greater voltages were necessary for a given ion deflection than would be required if the ion cloud was strictly composed of positive ions. The voltage required was also a function of ablation pulse energy, and therefore ion density. The fact that negative ions and/or electrons formed a neutral plasma with the ablation ions is likely responsible for us being able to obtain large numbers of translationally cold ions. Had this not been the case, patch charge effects would have likely lead to heating and deflections of our ion cloud at the skimmer. This neutral plasma character of our ion beam would likely also cause complications in any scheme to gently slow ions into our ion trap using the ions from our ablation source.

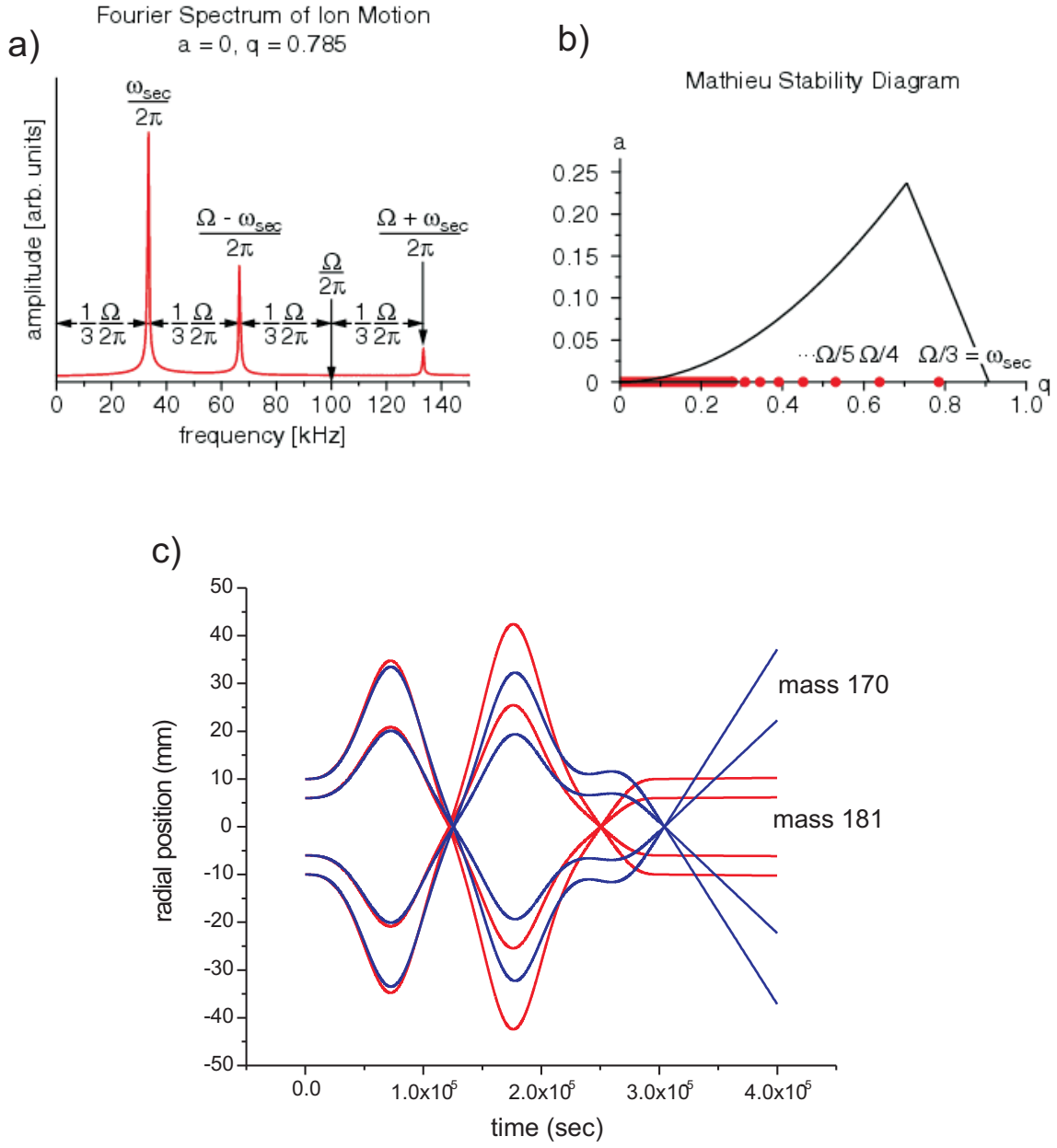

Figure 5.12: a) Spectrum of ion motions for values of trapping parameters $a = 0$ and $q = 0.785$ that can be used for operating an rf quadrupole as a mass-to-charge ratio sensitive ion lens. b) Dots denote values of q, with $a = 0$, that can be used in operating our ion lens. c)Numerical simulation of ion motion for different ion starting positions R_i, and two different singly-charged ions. The simulation was done with $a = 0$ and $q = 0.785$ for the mass = 181 ions.

5.7.2 State-Selective Photoionization

One alternative solution to our selective ion loading problem is to get rid of all of the ions created from laser ablation and use photoionization techniques to ionize neutral HfF in as state-selective a way as possible. Since the density of neutral HfF is much greater than the density of HfF^+ in our molecular beam, even inefficient photoionization could lead to higher densities of trapped HfF^+ than what can be achieved by loading the HfF^+ ions created from laser ablation. We have attempted two techniques, with both involving a transition to a Rydberg state of neutral HfF. Every ro-vibrational state in the molecular ion is the termination of a Rydberg series from the neutral molecule. These Rydberg states can be populated in our molecular beam experiment by first driving a transition from the electronic ground state to some intermediate bound state. This transition can be narrow and allow the excitation of only a single ro-vibrational state, of a single isotope. Another transition can then be made to a high-lying Rydberg level. If that Rydberg state is close enough to the ionization threshold, the application of a pulsed electric field can ionize the molecule while leaving the ro-vibrational level of the ion-core undisturbed. After the excitation laser pulses, a small electric field can be applied to give any molecules that were directly ionized by the lasers an acceleration. After waiting some time, a larger pulsed electric field can then be applied to ionize Rydberg-state molecules. The ions can then be accelerated in a time-of-flight mass spectrometer (TOFMS) and the field-ionized molecules will arrive at a different time compared to the direct ions. This process is referred to as mass analyzed threshold ionization spectroscopy, or MATI. Near the threshold of a molecular ion there will be a near continuum of Rydberg levels with different principle quantum number n and rotational quantum number. In order to populate only one rotational level in the ion, two field-ionizing pulses can be used, separated by some time. The first pulse ionizes all Rydberg states some energy from the continuum given roughly by $E = 4(\mathcal{E}_p)^{1/2}$ with $\mathcal{E}_p$ the magnitude of the pulsed electric field and with the energy in units of cm^{-1} and the electric field in units of V/cm. Those ions then experience an acceleration from a small applied "spoiling" electric field. The second field pulse is slightly larger in magnitude, thus ionizing a small

number of Rydberg states lying in a region $\delta \mathrm{E} = (4F - \delta\mathcal{E}_\mathrm{p})^{1/2} - 4F$, with F the value of the spoiling field [103]. There is a limit to the resolution that can be achieved by this method that depends on the value of the spoiling electric field and can be estimated as $\delta \mathrm{E} = 0.8F^{1/2}$. The resolution is therefore limited by the need of a sizable spoiling electric field in order to separate ions created at different times. For this reason, pulsed-field ionization techniques that measure the electrons as opposed to the ions created tend to have higher resolutions. However, similar resolutions have been demonstrated when measuring ions compared to electrons, when the proper pulse sequences are utilized [104]. The Rydberg states involved in this process can be largely immune from decay processes such as dissociation of the ion core, and electronic decay [103]. They are often referred to as ZEKE states, an acronym used to describe the technique when the free electron is measured instead of the molecular ion.

The second method we explored was a process known as autoionization. Here a neutral molecule is excited to a Rydberg state, in the same two-step process as before, but now the Rydberg molecule has a molecular-ion core that is in an excited state. This can be an electronic, vibrational, rotational or spin-orbit excitation. We will focus on vibrational autoionization, where the excited molecular core can interact with the orbiting Rydberg electron in an inelastic scattering process that leaves the Rydberg electron in the continuum and the molecular ion core in a relaxed vibrational state. This process has been known to leave the molecular ion core's rotational state largely unperturbed [105]. In this way we hope to excite a Rydberg level that corresponds to an excited $^3\Delta_1$ ion core with $v = 1$, $J = 1$. The Rydberg state might then vibrationally autoionize to the $v = 0$, $J = 1$ $^3\Delta_1$ level that will be used to measure the eEDM. Perhaps the Rydberg states involved have a faster decay rate via electronic autoionization to the ground $^1\Sigma$ level than to the $^3\Delta_1$ level via vibrational autoionization. In this case autoionization should still allow the creation of only the molecular ion species we desire in our ion trap, without the worry of imperfect electrostatics anywhere along our entire beam line distorting and heating the ion beam, and with the ion population in far fewer states than possible with molecular ions created from our ablation source.

5.7.3 Photoionization of HfF

A TOFMS was built and placed after two beam skimmers that were used to collimate the molecular beam, and after an electrode that could be biased at high positive voltages in order to reject ions from the ablation process. The TOFMS design involved the competition between simplicity, uniformity of electric fields, and a long drift chamber to allow the separation of ions created at slightly different times in delayed pulse measurements. A compromise was found using 90 mm diameter disk electrodes with 10 mm diameter holes for the ions to travel through, spaced by 52 mm for the MATI drift chamber, with a third electrode placed equidistant from them having a 38 mm diamter hole to create a more uniform field. These plates were followed by two more plates with spacings of 21 mm that allowed for focusing at the MCP detector of the initial spatial and velocity spread in the ion beam (see Fig. 5.13). This TOFMS was designed to be used with both ionization techniques discussed above, and was initially operated in a way consistent with the MATI techniques. For some of the later autoionization experiments the TOFMS was operated in a simpler Wiley-McLaren mode [106]. We were able to achieve better than 1 amu mass resolution when detecting HfF^+ with the isotope structure of Hf well resolved. This allowed us to see isotope shifts of transitions even though our laser resolution would normally have not allowed this. The isotope shifts were very useful in determining the change in vibrational state of the transition, δv. The isotope shift due to a change of vibrational quantum number is very easily estimated, and for HfF it should be ~ 0.16 cm$^{-1}/(\delta v\,\mathrm{amu})$, assuming a 600 cm^{-1} vibrational spacing.

Once the ionization threshold was found, we performed single-color experiments in search of intermediate HfF levels that could be useful in our ionization schemes. Fig. 5.14(a) shows the results of such a scan over an $\approx$ 3,000 cm^{-1} scan range that corresponded to a dye tuning curve. As seen in the figure, a high density of states were found, and many were scanned with single-color photoionization with enough resolution to roughly determine Ω and B_e. A few states were scanned at higher resolution in two-color ionization measurements. The first transition was driven by a cw ring-cavity dye laser that was pulsed amplified using a two-stage home-built dye cell amplifier, and

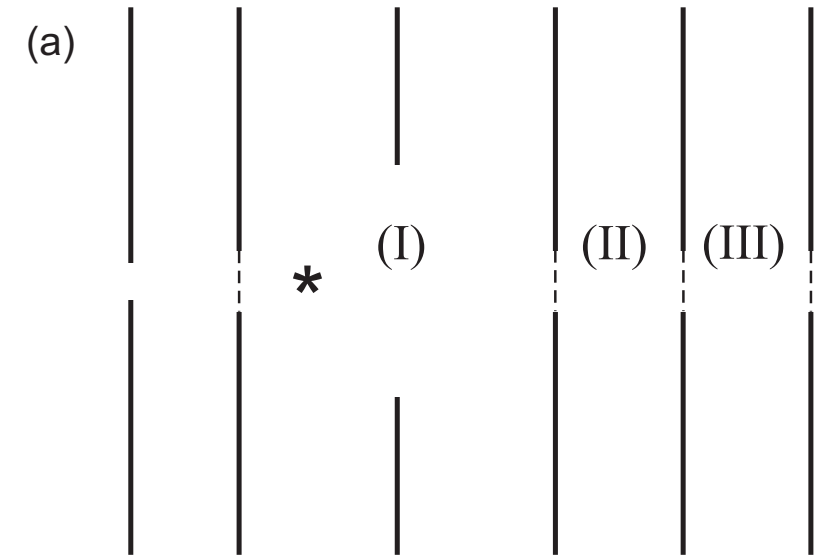

(b)

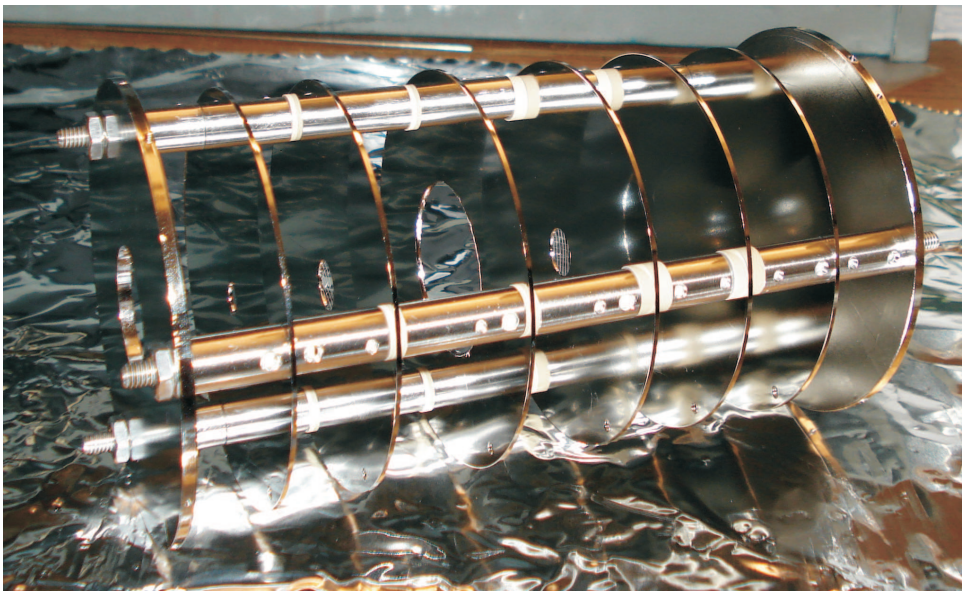

Figure 5.13: (a) Schematic of the time-of-flight mass spectrometer built for our experiment. The first plate is used to further collimate the neutral molecular beam and has a 6 mm diameter opening. Photoionization occurred at the approximate location marked by *. Region (I) could be used in delayed-pulse field ionization experiments to separate prompt ions from pulsed-field ions. Regions (II) and (III) were used to focus initial spatial and velocity spread of the created ions. Dashed lines correspond to high transmission (90%) wire mesh used to improve electric field uniformity. (b) An image of the TOFMS, before a grounded cylinder of wire mesh was placed around the device to shield it from external electric fields.

was then single-pass frequency doubled using a BBO crystal. This laser had a measured linewidth of $\sim$ 100 MHz and frequency-doubled pulse energies of 20-30 μJ in the UV. The second transition was driven by the large-linewidth (0.1 cm^{-1}) pulsed dye laser, with the laser tuned well above the threshold for ionization. Typical data is shown in Fig. 5.14(c).

A better measurement of the ionization threshold was made, taking into account the reduction in threshold energy due to an electric field. The electric field during the ionizing laser pulses was varied through zero while recording the onset of ionization. A value of 59,458 cm^{-1} was obtained for the ionization potential of HfF. Combining this with the published value of the HfF bond energy [101] of 53,966 cm^{-1} and the known value of Hf's ionization potential of 55,048 cm^{-1} gives a value of 49,556 cm^{-1} for the HfF^+ bond energy. *ab initio* calculations have estimated the HfF^+ bond energy at 51,107 cm^{-1} [64]. The measured HfF bond energy and the theoretical HfF^+ bond energy are both likely to have large ($\sim$ 1,000 cm^{-1}) errors, given the nature of their techniques.

Attempts at delayed pulse field ionization were unsuccessful. Although the literature suggests that ZEKE states can be long-lived, even in the presence of otherwise strong relaxation processes, a likely reason for our lack of signal was predissociation of our ZEKE states. It appears in some molecules decay channels simply win out, as many experiments find some molecules posses a delayed ionization signal and others do not (see Ref. [107] for an example).

We focused our efforts on our second scheme, vibrational autoionization. Fig. 5.15 shows data taken with two-color excitation, with the first transition again being driven by our narrow laser, and the second by the broad laser. As seen in Fig. 5.15(a), the spectrum is quite complex. The density of lines is increased by the fact that many large δv autoionization peaks are found, as determined by the isotope shifts associated with them (Fig 5.15(b)). This is surprising as vibrational autoionization is expected to have a strong propensity rule for $\delta v = 1$ transitions [108]. As understanding the autoionization is not necessary for our goals, our current work involves directly measuring the rotational state populations of the molecular ions produced in this process. This is done by performing LIF using the only known electronic transition in HfF^+ at $\sim$ 13,000 cm^{-1}. This work is ongoing and in the future we hope to detect ions created directly in the $^3\Delta_1$

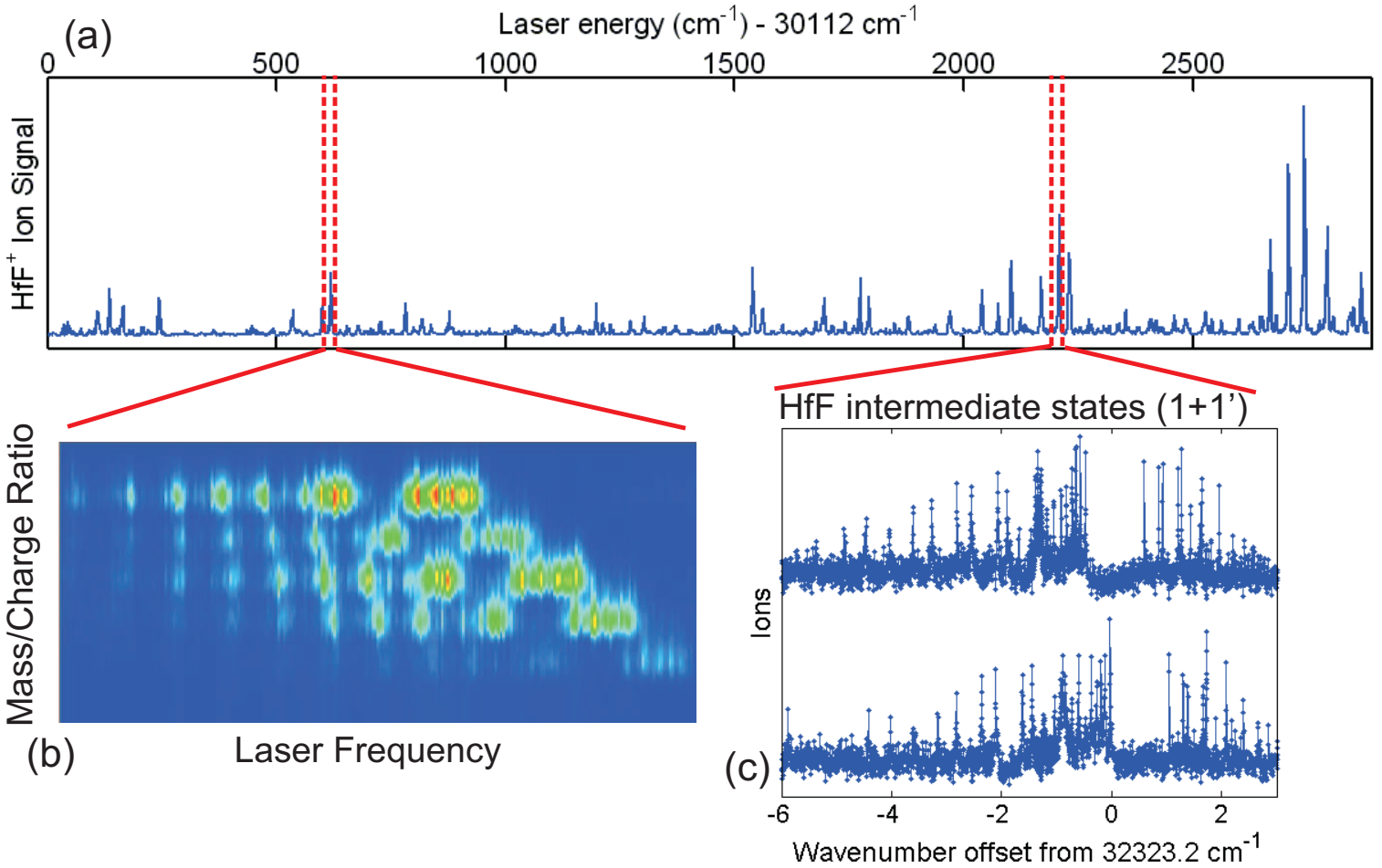

Figure 5.14: (a) Data from a two-photon one-color survey scan, with many UV transitions found in HfF. (b) False-color image showing our ability to separate different isotopes of HfF using our TOFMS, giving us the ability to measure isotope shifts and helping to identify the change in vibrational quantum number in these transitions. (c) Two-color photoionization showing a spectral resolution of approximately 100 MHz. The two traces correspond to the two dominant (m = 178 and m = 180) isotopes of HfF.

level, although that work is awaiting the discovery of a known electronic transition from the $^3\Delta_1$ level that might be used in LIF.

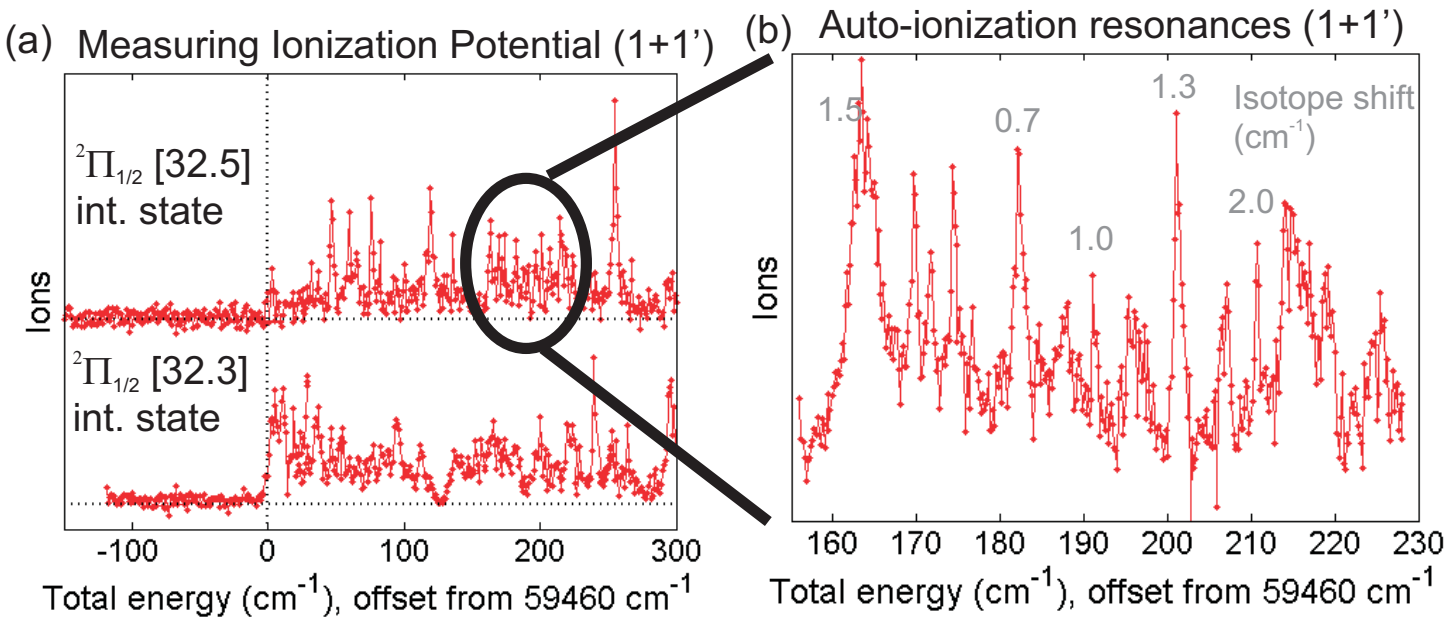

Figure 5.15: Autoionization spectra showing (a) the same ionization threshold for HfF using two different intermediate states and (b) large isotope shifts of the resonant features between $Hf^{178}F$ and $Hf^{180}F$. A change of one vibrational quanta between the intermediate HfF state and the HfF Rydberg state that undergoes autoionization corresponds to an isotope shift between $Hf^{178}F$ and $Hf^{180}F$ of 0.32 cm^{-1}. This data was taken using two-color photoionization, starting in the HfF ground electronic and ro-vibrational state.

Chapter 6

Spectroscopy in Rotating and Trapping Fields [1]

On the face of it, an ion trap, with its inhomogeneous and rapidly time-varying electric fields, is not necessarily a promising environment in which to perform sub-Hertz spectroscopic measurements on a polar molecule. In this section the effects of the various components of the electric and magnetic fields on the transition energies relevant to our science goals will be explored in more detail. The theoretical determination of the energy levels of heavy diatomic molecules in the presence of time-varying electric and magnetic fields is a tremendously involved problem in relativistic few-body quantum mechanics. State-of-the-art *ab initio* molecular structure calculations are limited to an energy accuracy of perhaps 10^{13} Hz, a quantity which could be compared with the size of a hypothetical "science signal", which could be on the order of 10^{-3} Hz or smaller.

Fortunately, we can take advantage of the fact that at the energy scales of molecular physics, time-reversal invariance is an exact symmetry except to the extent that there is a time-violating moment associated with the electron (or nuclear) spin. In this section, except in those terms explicitly involving d_e, it is assumed that time-reversal invariance is a perfect symmetry in order to analyze how various laboratory effects can cause decoherence or systematic shifts in the relevant resonance measurements. The results can be compared to the size of the line shift that would arise from a given value of the electron EDM, which is treated theoretically as a very small first-order perturbation on the otherwise T-symmetric system.

In the subsections below, sequentially more realistic features of the trapping fields are brought in.

6.1 Basic Molecular Structure

We begin by considering in detail the relevant molecular structure in zero electric and magnetic fields, thus quantifying the qualitative discussion of the experiment given in Chapter 2. Although the molecular structure cannot be calculated in detail from *ab initio* structure calculations, nevertheless its analytic structure is well known. Because the measurements will take place in nominally a single electronic, vibrational, and rotational state, we will employ an effective Hamiltonian within this state, as elaborated by Brown and Carrington [109]. This approach will specify a few undetermined numerical coefficients, whose values can be approximated from perturbation theory, but which will ultimately be measured.

Brown [110, 111, 112] and co-workers have done thorough work on deriving an effective Hamiltonian for $^3\Delta$ molecules. The complete Hamiltonian in the absence of d_e is given by

$$H_{\rm struct} = H_{\rm elec} + H_{\rm vib} + H_{\rm SO} + H_{\rm tum} + H_{\rm SS} + H_{\rm SR} + H_{\rm HFS} + H_{\rm LD}, \tag{6.1}$$

listed in rough order of decreasing magnitude. Since we are concerned only with terms acting within the subspace of the $^3\Delta$ manifold, other electronic and vibrational states will enter only as perturbations that help to determine the effective Hamiltonian. Thus we consider eigenstates of $H_{\rm elec}$ and $H_{\rm vib}$.

The remaining terms in Eq. (6.1) are corrections to the Born-Oppenheimer curves. They describe couplings between various angular momenta ($H_{\rm SR}$, $H_{\rm HFS}$), parity splittings ($H_{\rm LD}$, $H_{\rm HFS}$), and spin-dipolar interactions ($H_{\rm SS}$, $H_{\rm HFS}$). In typical Hund's case (a) molecules these interactions are small compared to the rotational energy governed by $H_{\rm tum}$. The relevant interactions that act within the $|\Omega| = 1$ manifold of states take the explicit form

$$H_{\rm SO} = A\Lambda\Sigma \tag{6.2}$$

$$H_{\rm tum} = B_e(\mathbf{J}-\mathbf{S})^2 - D(\mathbf{J}-\mathbf{S})^4 \tag{6.3}$$

$$H_{\rm SS} = \frac{2}{3}\lambda(3\Sigma^2 - \mathbf{S}^2) \tag{6.4}$$

$$H_{\rm SR} = \gamma_{\rm SR}(\mathbf{J}-\mathbf{S})\cdot\mathbf{S} \tag{6.5}$$

$$H_{\rm HFS} = aI_zL_z + b_{\rm F}\mathbf{I}\cdot\mathbf{S} + \frac{c}{3}(3I_zS_z - \mathbf{I}\cdot\mathbf{S}) + \frac{1}{2}e_\Delta(J_+I_+S_+^2 + J_-I_-S_-^2) \quad (6.6)$$

$$H_{\rm LD} = \frac{1}{2}(o_\Delta + 3p_\Delta + 6q_\Delta)(S_+^2J_+^2 + S_-^2J_-^2). \quad (6.7)$$

The constants in the first four terms are as follows: A is the molecular spin-orbit constant, B_e the rotational constant for the electronic level of interest, D the effect of centrifugal distortion on rotation (typically $D \sim B_e(m_e/m_{\rm mol})^2$, with m_e the electron mass and $m_{\rm mol}$ the reduced mass of the molecule), λ governs the strength of the spin-spin dipolar interaction, and $\gamma_{\rm SR}$ determines the strength of the interaction of the spin with the end-over-end rotation of the molecule. These four terms primarily describe an overall shift of the $^3\Delta_1$ J-level, and can be ignored in evaluating energy differences in the states we care about. They can, however, contribute small perturbations to these basic levels, as described below.

Within the $^3\Delta_1$, $J = 1$ manifold of interest, the energy levels are distinguished by the hyperfine and Λ-doubling terms. The hyperfine Hamiltonian $H_{\rm HFS}$ includes the familiar contact (b_F), nuclear-spin-orbit (a) and spin-nuclear spin terms (c). By estimating the parameters in perturbation theory, it is expected that the resulting hyperfine splitting is on the order of 50 MHz [54]. The hyperfine interaction also contains a previously unreported term, with constant denoted e_Δ, that is connected to the Λ-doubling. This term is expected to be even smaller than the already small Λ-doublet splitting itself, however, [113] and will be ignored.

The Λ-doubling Hamiltonian arises from Coriolis-type mixing of states with differing signs of Λ due to end-over-end rotation of the molecule. For a $^3\Delta$ state this interaction is characterized by three constants, of which the parameter o_Δ is the dominant one. These terms describe how the $^3\Delta$ state is perturbed by electronic states with $^{2S+1}\Pi$ and $^{2S+1}\Sigma$ symmetry. Since we are primarily concerned with terms in the Hamiltonian that affect the ground rotational state of the $^3\Delta_1$ electronic level, we only need to keep the term which connects $\Omega = 1$ to $\Omega = -1$. This term has the general form, with numerical prefactors $C_{\Pi,\Sigma,\Pi'}$ that depend on Clebsch-Gordon coefficients and wavefunction overlap, [110]

$$|o_\Delta + 3p_\Delta + 6q_\Delta| = \tilde{o}_\Delta \approx \sum_{\Pi,\Sigma,\Pi'} C_{\Pi,\Sigma,\Pi'}\frac{A^2\,B_e^2}{(\mathrm{E}_\Delta - \mathrm{E}_\Pi)(\mathrm{E}_\Delta - \mathrm{E}_\Sigma)(\mathrm{E}_\Delta - \mathrm{E}_{\Pi'})}, \quad (6.8)$$

where the sum is over all intermediate Σ and Π states of singlet and triplet spin symmetries. For HfF^+ this perturbation leads to a Λ-doublet splitting on the order of 10 kHz. From here on, we shall express the energy difference in parity levels for the $J = 1$ as $\omega_{\rm ef} = 4\tilde{o}_\Delta$, rather than $\tilde{o}_\Delta$ itself.

Thus the basic molecular structure of interest to the $^3\Delta_1$, $J = 1$ state is governed by two constants: the hyperfine splitting $E_{\rm hf}$ (given by $3A_{||}/4$ for $J = 1, I = 1/2$) and the Λ-doublet splitting $\omega_{\rm ef}$. These constants give the structure depicted in Fig. 2.1(a). These basic levels may be perturbed by couplings to other levels, especially rotational or electronic excited states. However, for the $J = 1$ state of interest, some simplifications are possible, namely: (1) Off-diagonal couplings in Ω are zero since $\mathbf{J} \cdot \mathbf{S}$ preserves the value of J (there is no level with $J = 1$ and $\Omega = 2$); (2) Off-diagonal contributions that mix $J = 2$ into the $J = 1$ manifold thus depend solely on the applied fields and the hyperfine interactions. Since the value of the spin-orbit constant is expected to be far larger than the rotational constant and we are concerned with a $J = 1$ state, the operators that connect Ω to $\Omega \pm 1$ will be ignored. The contributions to the ground state characteristics by terms off diagonal in Ω are smaller by a factor of the hyperfine interaction energy to the spin-orbit separation energy, hence a factor of 10^{-6}. This is the value which appears in front of any term connecting Ω to $\Omega \pm 1$ in the ground $J = 1$ state.

6.2 Effect of Non-rotating Electric and Magnetic Fields

The influence of external fields presents new terms in the Hamiltonian of the form

$$H_{\rm Stark} = -\vec{\mathbf{d}}_{\rm mf} \cdot \vec{\mathcal{E}} \tag{6.9}$$

$$H_{\rm Zeeman} = -\vec{\mu} \cdot \vec{\mathcal{B}}. \tag{6.10}$$

Here $\vec{\mathcal{E}}$ and $\vec{\mathcal{B}}$ are the electric and magnetic fields, assumed for the moment to be collinear so that they define the axis along which m_F is a good quantum number; while $\vec{\mathbf{d}}_{\rm mf}$ and $\vec{\mu}$ are the electric and magnetic dipole moments of the molecule.

The electric dipole moment arises from the body-fixed molecular dipole moment, at fields sufficiently small not to disturb the electronic structure. We assume that the field is sufficiently

large to completely polarize this dipole moment, i.e., $d_{\mathrm{mf}}\mathcal{E} \gg \omega_{\mathrm{ef}}$, in which case the Stark energies are given by

$$\mathrm{E}_{\mathrm{Stark}} = -m_F \Omega \gamma_F d_{\mathrm{mf}} \mathcal{E}, \tag{6.11}$$

where γ_F is a geometric factor, analogous to a Landé g-factor, which accounts for the Stark effect in the total angular momentum basis F. In the limit where the electric field is weak compared to rotational splittings, it is given by

$$\gamma_F = \frac{J(J+1) + F(F+1) - I(I+1)}{2F(F+1)J(J+1)}. \tag{6.12}$$

Its numerical values in the $J = 1$ state are therefore $\gamma_{F=3/2} = 1/3$ and $\gamma_{F=1/2} = 2/3$. The electric field therefore raises the energy of the states with $m_F\Omega < 0$ (denoted "upper" states with superscript u), and lowers the energy of states with $m_F\Omega > 0$ ("lower" states with superscript ℓ). This shift in energy levels is shown in Fig. 2.1(b), where $|a\rangle$ and $|b\rangle$ are upper and $|c\rangle$ and $|d\rangle$ are lower states.

The form of the Zeeman interaction is somewhat more elaborate, as the magnetic moment of the molecule can arise from any of the angular momenta $\mathbf{L}$, $\mathbf{S}$, $\mathbf{J}$, and $\mathbf{I}$. Quite generally, however, in the weak-field limit where $\mu_B\mathcal{B} \ll \mathrm{E}_{\mathrm{hf}}$, the Zeeman energies are given by $m_F g_F^{u/\ell} \mu_B \mathcal{B}$, where μ_B is the Bohr magneton and $g_F^{u/\ell}$ are g-factors for the upper and lower states. In general, $g_F^u \neq g_F^\ell$, and this difference can depend on electric field, a possible source of systematic error. We will discuss this in Chapter 6.8.

The leading order terms in the Zeeman energy are those that preserve the signed value of Ω. They are given by

$$H_{\mathrm{Zeeman}} = \left(\gamma_F \left[\left((g_L + g_r)\Lambda + (g_S + g_r)\Sigma\right)\Omega - g_r J(J+1)\right] - g_I \kappa_F\right) m_F \mu_B \mathcal{B}, \tag{6.13}$$

where $\kappa_F = (F(F+1) + I(I+1) - J(J+1))/2F(F+1)$ is another Landé-type g-factor, but for nuclear spin. The orbital and spin g-factors are g_L and g_S , while the rotation and nuclear spin g-factors are g_r and g_I. Both g_r and g_I are small, being on the order of the electron-to-molecular mass ratio $\sim m_e/m_{\mathrm{mol}} \sim 10^{-3}$. Thus for an idealized $^3\Delta_1$ molecule where $g_L = 1$, $\Lambda = \pm 2$, $g_S = 2$,

$\Sigma = \mp 1$, we would expect molecular g-factors on the order of 10^{-3}. In a slightly less ideal situation, g_s differs from 2 by a number on the order of α, the fine structure constant, and a g-factor $\sim 10^{-2}$ might be expected. In heavy-atom molecules such as ours for which spin-orbit effects mix Λ, we may expect instead the difference $2g_L - g_S$ to be as large as ~ 0.1 in magnitude. If we assume the dominant contribution comes from these spin-orbit type effects, we can define the g-factor for the $J = 1$ state as

$$g_{F=3/2} = \gamma_{F=3/2}(g_L\Lambda + g_S\Sigma)\Omega <\approx 0.03, \tag{6.14}$$

while

$$g_{F=1/2} = 2g_{F=3/2}. \tag{6.15}$$

Finally, the effect of the EDM itself introduces a small energy shift

$$H_{\mathrm{EDM}} = -\vec{d_e} \cdot \vec{\mathcal{E}}_{\mathrm{eff}} = d_e \mathcal{E}_{\mathrm{eff}} \vec{\sigma}_1 \cdot \hat{n}, \tag{6.16}$$

where $\vec{\sigma}_1$ is the spin of the s-electron contributing to the EDM signal; and $\hat{n}$ denotes the inter-molecular axis, with $\hat{n}$ pointing from the more negative atom to the more positive one; in our case from the fluorine or hydrogen to thorium, platinum, or hafnium. Also in this convention we take $\mathcal{E}_{\mathrm{eff}}$ as positive if it is anti-parallel to $\hat{n}$. The energy shift arising from this Hamiltonian depends only on the relative direction of the electron spin and the internuclear axis, and is given by

$$\mathrm{E}_{\mathrm{EDM}} = -\frac{d_e \mathcal{E}_{\mathrm{eff}}}{2|\Omega|}\Omega. \tag{6.17}$$

Polarizing the molecule in the external field selects a definite value of Ω, hence a definite energy shift, positive or negative, due to the EDM. This additional shift is illustrated in Fig. 2.1(c).

For a range of field strengths and parameters, the energies of the sublevels within the $J = 1$ manifold are well approximated by a linear expansion in the electric and magnetic fields. We define

$$\vec{\mathcal{B}} = \mathcal{B}_{||}\frac{\vec{\mathcal{E}}}{|\mathcal{E}|} + \vec{\mathcal{B}}_{\perp} \tag{6.18}$$

Taking $\omega_{\mathrm{ef}} \ll d_{\mathrm{mf}}\mathcal{E} \ll \mathrm{E_{hf}}$ and $d_{\mathrm{mf}}\mathcal{E} \gg g_F\mu_B\mathcal{B}_{||}$, and setting $\mathcal{B}_{\perp} = 0$, we get for the non-rotating energies,

$$\mathrm{E}^{u/\ell}_{\mathrm{nr}}(F, m_F, \Omega; \mathcal{E}, \mathcal{B}) \approx \frac{1}{3}(F(F+1) - \frac{11}{4})\mathrm{E_{hf}} - m_F\Omega\gamma_F d_{\mathrm{mf}}\mathcal{E} + m_F g_F^{u/\ell}\mu_B\mathcal{B} - (d_e\mathcal{E}_{\mathrm{eff}}/2|\Omega|)\Omega, \tag{6.19}$$

where Ω is either 1 or -1, and the prefactor in front of $\mathrm{E_{hf}}$ is such that for the $J = 1$ level, $\mathrm{E}(F = 3/2)$ - $\mathrm{E}(F = 1/2) = 3A_{||}/4 = \mathrm{E_{hf}}$. F and Ω are good quantum numbers only to the extent that the electric field is neither too large nor too small, but we will use F and Ω as labels for levels even as these approximations begin to break down.

For notational compactness, we introduce special labels for particular states as follows (see Fig. 2.1(b)):

$$\begin{aligned} |a\rangle &= |F = 3/2, m = 3/2, \Omega = -1\rangle \\ |b\rangle &= |F = 3/2, m = -3/2, \Omega = 1\rangle \\ |c\rangle &= |F = 3/2, m = 3/2, \Omega = 1\rangle \\ |d\rangle &= |F = 3/2, m = -3/2, \Omega = -1\rangle \end{aligned} \tag{6.20}$$

with corresponding energies, E_a, E_b, E_c, and E_d, and identify the energies of two particularly interesting transitions, $W^u = \mathrm{E}_a - \mathrm{E}_b$, and $W^\ell = \mathrm{E}_c - \mathrm{E}_d$ such that

$$\begin{aligned} W^u &= 3g_F^u \mu_B \mathcal{B} + d_e \mathcal{E}_{\mathrm{eff}} \\ W^\ell &= 3g_F^\ell \mu_B \mathcal{B} - d_e \mathcal{E}_{\mathrm{eff}}. \end{aligned} \tag{6.21}$$

The equations of this section have so far been to one degree or another approximate results. But in the absence of exotic particle physics we can invoke time-reversal symmetry and write *exact* relations:

$$\mathrm{E_{nr}}(F, m_F, \Omega; \mathcal{E}, \mathcal{B}) - \mathrm{E_{nr}}(F, -m_F, -\Omega; \mathcal{E}, \mathcal{B}) = \mathrm{E_{nr}}(F, -m_F, -\Omega; \mathcal{E}, -\mathcal{B}) - \mathrm{E_{nr}}(F, m_F, \Omega; \mathcal{E}, -\mathcal{B}) \tag{6.22}$$

which, for $\mathcal{B} = 0$, becomes

$$\mathrm{E_{nr}}(F, m_F, \Omega; \mathcal{E}) = \mathrm{E_{nr}}(F, -m_F, -\Omega; \mathcal{E}). \tag{6.23}$$

This exact degeneracy is, in fact, an example of the Kramers degeneracy that follows from time-reversal invariance [114]. For our purposes, the key result here is that, in the limit of non-rotating fields, zero applied magnetic field, and an electron EDM, the energy of the science transitions

$|m_F, \Omega\rangle \leftrightarrow |-m_F, -\Omega\rangle$ (and in particular, W^u and W^ℓ) are independent of the magnitude of the electric field. This is an important property because we are using spatially inhomogeneous electric fields to confine the ions in the trap, and we want to minimize the resulting decoherence.

This degeneracy in turn means that the energy differences W^u and W^l depend only on the magnetic field and, of course, the EDM term as shown in Eq. (6.21). The magnetic contribution reverses sign upon reversing the direction of $\mathcal{B}$ with respect to the electric field direction (which also sets the quantization axis, since $d_{\rm mf}\mathcal{E} \gg \mu_B\mathcal{B}$). Therefore the science measurement is given by the combinations

$$\begin{aligned} W^u(\mathcal{E},\mathcal{B}) + W^u(\mathcal{E},-\mathcal{B}) &= 2d_e\mathcal{E}_{\rm eff} \\ W^l(\mathcal{E},\mathcal{B}) + W^l(\mathcal{E},-\mathcal{B}) &= -2d_e\mathcal{E}_{\rm eff}, \end{aligned} \tag{6.24}$$

where a + sign on $\mathcal{B}$ denotes that it points in the same direction as $\mathcal{E}$.

6.3 Rotating Fields, Small-Angle Limit

Many EDM experiments over the years have been complicated by the problem of "Berry's phase", the term in this context used as a catch-all to describe a variety of effects related to the motion of the particles in inhomogeneous fields.

The sketch in Fig. 6.1(a) illustrates the classic Berry's phase result: if the field that defines the quantization axis, as experienced locally by a particle (or atom, or molecule), precesses about the laboratory axis at some angle, θ, then, in the limit of slow precession, with each cycle of the precession the wave-function Ψ picks up a phase given by $m_F\mathcal{A}$, where m_F is the instantaneous projection of the particle's total angular momentum on the quantization axis, and $\mathcal{A}$ is the solid angle subtended by the cone. If the precession is periodic with period τ, one can (with provisos, as we will discuss) think of this phase-shift as being associated with a frequency, or indeed energy, $m_F\mathcal{A}/\tau$. In a spectroscopic measurement of the energy difference between two states whose m_F values differ by δm_F, there will be a contribution to the transition angular frequency $\mathcal{A}\delta m_F/\tau$.

In neutron EDM experiments, motional magnetic fields, in combination with uncharacterized

fixed gradients from magnetic impurities, Berry's phase can be a dangerous systematic whose dependence on applied fields can mimic an EDM signal [115]. In Chapter 6.14 we will see that the effects of motional fields in our experiment are negligible.

Neutral atoms or molecules may be confined in traps consisting of static configurations of electric or magnetic fields. These traps are based on the interaction between the trapped species' magnetic or electric dipoles and the inhomogeneous magnetic or electric fields, respectively, of the trap. Especially in cases where the traps are axially symmetric, so that the single-particle trajectory of an atom can orbit many times one way or the other about the axis of the trap, the coherence time of an ensemble of atoms with a thermal distribution of trajectories can be severely restricted [116]. Our system is quite different, because in an ion trap the forces arise from the interaction between the trapping fields and the monopole moment of our trapped ion. Assuming the temperature, size of bias field, and radius of confinement are the same, the trapping fields for an ion are spatially much more homogeneous than would be those for a neutral molecule or atom.

That said, the fact that we can speak of a "bias" electric field at all in an ion trap comes at the cost of having the applied electric field constantly rotating.

6.4 Rotating Fields, Large-Angle Limit (Dressed States)

The basic dressed-state idea is an extension of the more common idea of an energy eigenstate: a system governed by a time-invariant Hamiltonian H will have solutions Ψ such that $\Psi(t+T) = e^{-i\omega T}\Psi(t)$ for all T and t; such a solution Ψ is called an energy eigenstate, with ω being then the corresponding energy. Similarly, a system governed by a periodic Hamiltonian with period τ such that $H(t+\tau) = H(t)$ for all values of t, will have so-called "dressed-state" solutions Ψ such that $\Psi(t+n\tau) = e^{-in\phi}\Psi(t)$ for all t and all integer values of n. The quantity ϕ/τ is sometimes referred to as the dressed state energy.

Operationally, the dressed state energies are derived from the eigenvalues of a formally time-independent Hamiltonian. If H_0 denotes the Hamiltonian in the absence of the field, then the

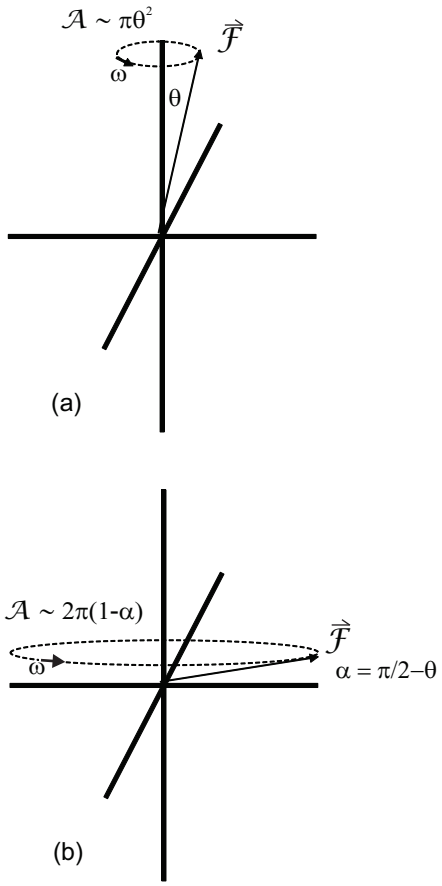

Figure 6.1: a) Small-angle limit. When the quantization axis $\mathcal{F}$ follows a slow periodic perturbation characterized by tilt angle θ, angular frequency ω and enclosed solid angle $\mathcal{A}$, two states whose instantaneous projection of angular momentum along $\mathcal{F}$ differs by δm will have their effective relative energy displaced by a Berry's energy $\omega\mathcal{A}\delta m/2\pi$. b) Large-angle limit. When instead the quantization axis sweeps out a full 2π steradians per cycle (α=0), the differential phase shift between the two levels is indistinguishable from zero, and in the most natural conceptual framework, the Berry's energy vanishes.

appropriate rotation-dressed Hamiltonian is given by

$$H_{\text{dressed}} = H_0 - \vec{d}_{\text{mf}} \cdot \vec{\mathcal{E}}_{\text{rot}} + H_{\text{rot}}, \tag{6.25}$$

H_{rot} is defined as [117]

$$H_{\text{rot}} = -\omega_{\text{rot}} \left(\cos(\theta) F_z - \sin(\theta) F_x\right) \tag{6.26}$$

where $F_z$and F_x are the projections of the total angular momentum $\vec{F}$ into a set of axes where z coincides with the instantaneous direction of the electric field. We now make explicit the rotating electric field with $\vec{\mathcal{E}}_{\text{rot}}$. The $\cos(\theta)$ term thus provides an energy which, when multiplied by the rotational period $\tau = 2\pi/\omega_{\text{rot}}$, gives the ordinary Berry phase,

$$-2\pi \cos(\theta) m_F \rightarrow 2\pi(1 - \cos(\theta)) m_F \tag{6.27}$$

where we have taken the liberty of adding an arbitrary phase $2\pi m_F$ to reveal explicitly the solid angle $2\pi(1 - \cos\theta)$.

In the experiment, the applied electric field should lie very nearly in the plane orthogonal to the rotation axis, i.e., $\theta \approx \pi/2$. It is therefore useful to consider the small angular deviation from this plane, $\alpha = \pi/2 - \theta$ (Fig. 6.1). Then the apparent energy shift arising from the geometric phase is

$$\mathrm{E}_{\text{geo}} = -m_F \omega_{\text{rot}} \sin(\alpha) \approx -m_F \omega_{\text{rot}} \alpha. \tag{6.28}$$

Now consider two states which are, in the absence of rotation, degenerate, say the states $|a\rangle$, with $m = 3/2, \Omega = -1$, and the state $|b\rangle$, with $m = -3/2, \Omega = 1$, indicated in Fig 2.1(b). Rotation breaks this degeneracy, by adding the energies $\sim \pm(3/2)\omega_{\text{rot}}\alpha$, as shown by the dashed lines in Fig. 6.2. These levels cross at $\alpha = 0$, leading to their apparent degeneracy when the electric field lies in the horizontal plane.

In addition, the rotation of the field also incurs coupling between states with different m_F values, arising from the $\sin(\theta)$ term in Eq. (6.26). This perturbation, treated at third-order in perturbation theory, connects the two levels and turns the crossing into an avoided one, as shown

by the solid lines in Fig. 6.2. This has been worked out by Meyer in Ref. [113]. The result, for the $m_F = \pm 3/2$ states in Fig. 2.1(b), is

$$\Delta^{u/\ell} \approx 170\omega_{\rm ef}\left(\frac{\omega_{\rm rot}}{d_{\rm mf}\mathcal{E}_{\rm rot}}\right)^3, \tag{6.29}$$

where Δ is the energy splitting at the level crossing between otherwise degenerate states with $m_F > 0$ and $m_F < 0$. The superscript u refers to mixing between the $|a\rangle$ and $|b\rangle$ states, and the superscript ℓ to mixing between $|c\rangle$ and $|d\rangle$ states. In the absence of the hyperfine interaction, the average value of the numerical prefactor is 170 and the upper and lower states have the same avoided crossing. However, small fractional differences between Δ^u and Δ^ℓ turn out to be significant, and are discussed further below.

The presence of the electric field causes the states with $|F = 1/2, m_F = \pm 1/2\rangle$ and $|F = 3/2, m_F = \pm 1/2\rangle$ to mix. Including the hyperfine interaction into the numerical diagonalization yields

$$\Delta = \frac{1}{2}(\Delta^u + \Delta^\ell) \approx 170\ \omega_{\rm ef}\left(\frac{\omega_{\rm rot}}{d_{\rm mf}\mathcal{E}_{\rm rot}}\right)^3, \tag{6.30}$$

$$\delta\Delta = \frac{1}{2}(\Delta^u - \Delta^\ell) \approx 127\ \omega_{\rm ef}\left(\frac{\omega_{\rm rot}}{d_{\rm mf}\mathcal{E}_{\rm rot}}\right)^3\left(\frac{d_{\rm mf}\mathcal{E}_{\rm rot}}{\mathrm{E_{hf}}}\right)^2. \tag{6.31}$$

It is evident that the average shift is the same, but now the upper and lower levels acquire a different splitting due to the rotation-induced mixing within the sublevels. The difference is suppressed relative to the average value of the splitting by a factor of $(d_{\rm mf}\mathcal{E}/\mathrm{E_{hf}})^2$, reflecting the fact that higher orders of perturbation theory are needed to include the effects of the hyperfine interaction. For $\omega_{\rm ef} = 2\pi\times 10$ kHz, $\omega_{\rm rot} = 2\pi\times 100$ kHz, $d_{\rm mf}\mathcal{E}_{\rm rot} = 2\pi\times 10$ MHz, $\mathrm{E_{hf}} = 2\pi\times 40$ MHz, then $\Delta = 2\pi\times 1.7$ Hz and $\delta\Delta = 2\pi\times 0.08$ Hz.

The magnitude of the rotation-induced mixing within any of the four pairs of otherwise degenerate $m = \pm 1/2$ states is much larger than the mixing within either pair of $m = \pm 3/2$ states, Δ^u or Δ^ℓ. For this reason, the $m = \pm 1/2$ levels are probably not great candidates for precision metrology in rotating fields.

An ion in a trap will feel an axial force pushing it towards the axial position where the axial electric field vanishes, that is, the location at which α is identically zero. This poses a problem,

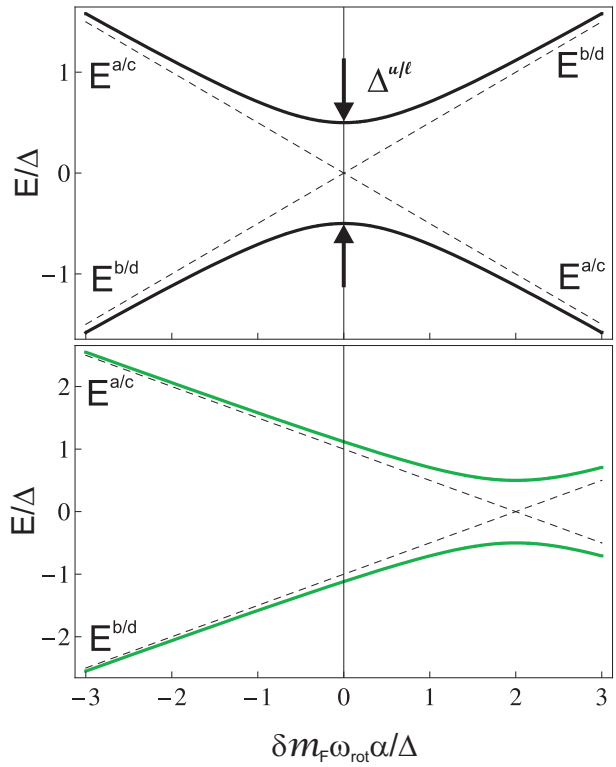

Figure 6.2: The apparent energy shifts between $m_F = +3/2$ and $m_F = -3/2$ states in upper (a,b) and lower (c,d) Λ-doublet levels versus α, the angle of the electric field to the plane orthogonal the rotation axis of $\mathcal{E}_{\rm rot}$ (α is shown in Fig. 6.1(b)). (a) At $\alpha = 0$, there is an avoided crossing that mixes $m_F = \pm 3/2$ states, with an energy splitting at the crossing of $\Delta^{u/\ell}$. (b) Since $\alpha = 0$ at the axial trap center, and since we need m_F to be a signed quantity in order to measure d_e, we will bias away from the avoided crossing using a magnetic field $\mathcal{B}_{\rm rot}$. $\delta m_F g_F \mu_B \mathcal{B}_{\rm rot} > \Delta^{u/\ell}$ is required for m_F to be a quantity of definite sign. This picture is intuitively correct in the limit that $\Delta^{u/\ell} > \omega_{\rm max}$. The experiment will be performed in the opposite limit. However, solving the time dependent Schrödinger equation (Eq. 6.42) gives the same requirement of $\delta m_F g_F \mu_B \mathcal{B}_{\rm rot} > \Delta^{u/\ell}$ in both limits.

because at $\alpha = 0$, each dressed state is an equal mixture of states with $\Omega = 1$ and with $\Omega = -1$. In other words, the dressed states right at the avoided crossing will have vanishing eEDM signal. The solution is to bias the avoided crossing away from $\alpha = 0$ by adding to the trapping fields a uniform, rotating magnetic field which is instantaneously always parallel or anti-parallel to vector $\mathcal{E}_{\rm rot}$.

$$\vec{\mathcal{B}}_{\rm rot} = \frac{\mathcal{B}_{\rm rot}}{\mathcal{E}_{\rm rot}} \vec{\mathcal{E}}_{\rm rot} \tag{6.32}$$

In our convention, $\vec{\mathcal{E}}_{\rm rot}$ defines the quantization axis, so that the number $\mathcal{E}_{\rm rot}$ will always be taken to be positive. The sign of $\mathcal{B}_{\rm rot}$ then determines whether the co-rotating magnetic field is parallel ($\mathcal{B}_{\rm rot} > 0$) or anti-parallel ($\mathcal{B}_{\rm rot} < 0$).

The energy levels are now as shown in Fig. 6.2(b). As derived in Chapter 6.5, in the limit $\mathcal{B}_{\rm rot} g_F \mu_B \gg \Delta^{u/\ell}$, the dressed states near $\alpha = 0$ are once again states of good m_F and Ω. The energy splitting between the two states, as altered by the rotation of the field, are given approximately by

$$W^{u/\ell}(\mathcal{E}_{\rm rot}, \mathcal{B}_{\rm rot}) = \mathrm{E}_{a/c} - \mathrm{E}_{b/d} = -3\alpha\omega_{\rm rot} + 3g_F^{u/\ell}\mu_B\mathcal{B}_{\rm rot} + \frac{(\Delta^{u/\ell})^2}{6g_F^{u/\ell}\mu_B\mathcal{B}_{\rm rot} - 6\alpha\omega_{\rm rot}} \pm d_e\mathcal{E}_{\rm eff}, \tag{6.33}$$

where the + sign corresponds to u states, and the − sign to ℓ states.

Over the course of one axial oscillation of the ion in the trap, α which is approximately proportional to the axial electric field, will average to zero. Unfortunately, the contributions to δW from $\mathcal{E}_{\rm rot}$ and from $\mathcal{B}_{\rm rot}$ are larger than that from the scale of the physics we most care about, $d_e\mathcal{E}_{\rm eff}$, and the spatial and temporal variation in $\mathcal{E}_{\rm rot}$ and in $\mathcal{B}_{\rm rot}$ will reduce the coherence time of the spectroscopy, as discussed in Chapter 6.9 - 6.11. But to the extent that one is able quite precisely to chop $\mathcal{B}_{\rm rot}$ to $-\mathcal{B}_{\rm rot}$ on alternate measurements, the science signal still arises from the same combination as in Eq. 6.24:

$$\langle W^{u/\ell}(\mathcal{E}_{\rm rot}, \mathcal{B}_{\rm rot})\rangle + \langle W^{u/\ell}(\mathcal{E}_{\rm rot}, -\mathcal{B}_{\rm rot})\rangle \approx \pm 2 d_e\mathcal{E}_{\rm eff}, \tag{6.34}$$

where the +/- corresponds to the u/ℓ superscripts respectively, and the brackets denote averaging over the excursions of α, which is assumed to vary symmetrically about zero.

The equation above relies on several approximations. One needs in particular that $d_{\rm mf}\mathcal{E}_{\rm rot} \gg \omega_{\rm ef}$, $3g_F\mu_B B_{\rm rot} \gg 170\omega_{\rm ef}$ $(\omega_{\rm rot}/d_{\rm mf}\mathcal{E}_{\rm rot})^3$, and $d_{\rm mf}\mathcal{E}_{\rm rot} \gg \omega_{\rm rot}$, $\alpha \ll 1$, and $d_{\rm mf}\mathcal{E}_{\rm rot} < {\rm E_{hf}}$. These are all good approximations, but they are not perfect. For example, using values from Appendix A, $\omega_{\rm rot}/(d_{\rm mf}\mathcal{E}_{\rm rot}) \approx 0.01$, a small number, but not zero. To what extent will imperfections in these approximations mimic an eEDM signal?

The driving principle of our experimental design is to measure d_e with as close to a null background as possible. We are not especially concerned if the right hand side of Eq. (6.34) is 1.9 $d_e\mathcal{E}_{\rm eff}$ rather than 2.0 $d_e\mathcal{E}_{\rm eff}$. More important to us is that, if $d_e = 0$, the right-hand side of Eq. (6.34) be as close to zero as possible. As we shall see, as long as we preserve certain symmetries of the system we are guaranteed a very high quality null. A preliminary remark is that the "energy" of a dressed state, or more precisely the phase shift per period τ, is unaffected by an offset in how the zero of time is defined. A second observation is that, in the absence of exotic particle physics (such as nonzero eEDM), the energy levels of a diatomic molecule in external electromagnetic fields are not affected by a global parity inversion.

Under the action of this inversion, all the fields and interactions in the Hamiltonian transform according to their classical prescriptions, whereas quantum states are transformed into their parity-related partners. In a parity-invariant system, parity thus changes quantum numbers, but leaves energies of the eigenstates unchanged. This is true for the dressed states as well, since their eigen-energies emerge formally from a time-independent Hamiltonian.

To formulate the effect of inversion symmetry we write the electric and magnetic fields as

$$\vec{\mathcal{E}} = \mathcal{E}_{\rm rot}\hat{r}' + \mathcal{E}_z\hat{z} \tag{6.35}$$

$$\vec{\mathcal{B}} = \mathcal{B}_{\rm rot}\hat{r}' \tag{6.36}$$

where $\hat{r}' = \cos(\omega_{\rm rot}t)\hat{x} + \sin(\omega_{\rm rot}t)\hat{y}$ and $\alpha = \tan^{-1}(\mathcal{E}_z/\mathcal{E}_{\rm rot})$. The dressed states defined by the rotating field are characterized by the projection m_F of total angular momentum on the axis defined by the rotating electric field, $\vec{\mathcal{E}}_{\rm rot}/\mathcal{E}_{\rm rot}$. Because the magnetic field is not strictly collinear with the electric field, and because of the field rotation, m_F is only approximately a good quantum number.

Nevertheless, considering the effect of parity on all the m_F's simultaneously, we can still map each dressed eigenstate into its parity-reversed partner.

Assuming the ions are "nailed down" in their axial oscillation, at a particular value of $\mathcal{E}_z$ and thus α, our various spectroscopic measurements would give dressed energy differences $\mathrm{E}(\mathcal{E}_{\mathrm{rot}}, \mathcal{B}_{\mathrm{rot}}, \alpha, m_F, \Omega) - \mathrm{E}(\mathcal{E}_{\mathrm{rot}}, \mathcal{B}_{\mathrm{rot}}, \alpha, -m_F, -\Omega)$. Now we invoke the following symmetry argument: if we take the entire system, electric fields, magnetic field, and molecule, and apply a parity inversion, that will leave the energy of the corresponding levels unchanged. If further we then shift the zero of time by $\pi/\omega_{\mathrm{rot}}$, in effect letting the system advance through half a cycle of the field rotation, that also will not change the corresponding energy levels of the dressed state, which are after all defined over an entire period of the rotation. This transformation effectively connects measurements made for $\alpha > 0$, above the mid-plane, to those with $\alpha < 0$, below the mid-plane. The combined transform acts as follows:

$$\begin{aligned}
F &\rightarrow F \\
\vec{\mathcal{B}}_{\mathrm{rot}} &\rightarrow -\vec{\mathcal{B}}_{\mathrm{rot}} \\
\vec{\mathcal{E}}_{\mathrm{rot}} &\rightarrow \vec{\mathcal{E}}_{\mathrm{rot}} \\
\mathcal{E}_z &\rightarrow -\mathcal{E}_z \\
\alpha &\rightarrow -\alpha \\
\vec{\omega}_{\mathrm{rot}} &\rightarrow \vec{\omega}_{\mathrm{rot}} \\
m_F &\rightarrow -m_F \\
\vec{S} \cdot \vec{\mathcal{B}} &\rightarrow \vec{S} \cdot \vec{\mathcal{B}} \\
\hat{d} \cdot \vec{\mathcal{E}} &\rightarrow \hat{d} \cdot \vec{\mathcal{E}} \\
\Omega &\rightarrow -\Omega
\end{aligned} \tag{6.37}$$

The last of these is equivalent to $\hat{n} \cdot \vec{\sigma}_1$, i.e., our symmetry operation would change the sign of the EDM energy shift. However, in the *absence* of this shift we can expect the following exact relations

between the dressed state energies:

$$\begin{aligned}
&\mathrm{E}(\mathcal{E}_{\mathrm{rot}}, \mathcal{B}_{\mathrm{rot}}, \alpha, m_F, \Omega) - \mathrm{E}(\mathcal{E}_{\mathrm{rot}}, -\mathcal{B}_{\mathrm{rot}}, -\alpha, -m_F, -\Omega) = 0 \\
&\mathrm{E}(\mathcal{E}_{\mathrm{rot}}, -\mathcal{B}_{\mathrm{rot}}, \alpha, m_F, \Omega) - \mathrm{E}(\mathcal{E}_{\mathrm{rot}}, \mathcal{B}_{\mathrm{rot}}, -\alpha, -m_F, -\Omega) = 0 \\
&\mathrm{E}(\mathcal{E}_{\mathrm{rot}}, \mathcal{B}_{\mathrm{rot}}, -\alpha, m_F, \Omega) - \mathrm{E}(\mathcal{E}_{\mathrm{rot}}, -\mathcal{B}_{\mathrm{rot}}, \alpha, -m_F, -\Omega) = 0 \\
&\mathrm{E}(\mathcal{E}_{\mathrm{rot}}, -\mathcal{B}_{\mathrm{rot}}, -\alpha, m_F, \Omega) - \mathrm{E}(\mathcal{E}_{\mathrm{rot}}, \mathcal{B}_{\mathrm{rot}}, \alpha, -m_F, -\Omega) = 0.
\end{aligned} \tag{6.38}$$

Summing four equations and rearranging terms, we get that

$$W^{u/\ell}(\mathcal{E}_{\mathrm{rot}}, \mathcal{B}_{\mathrm{rot}}, \alpha) + W^{u/\ell}(\mathcal{E}_{\mathrm{rot}}, -\mathcal{B}_{\mathrm{rot}}, \alpha) + W^{u/\ell}(\mathcal{E}_{\mathrm{rot}}, -\mathcal{B}_{\mathrm{rot}}, -\alpha) + W^{u/\ell}(\mathcal{E}_{\mathrm{rot}}, \mathcal{B}_{\mathrm{rot}}, -\alpha) = 0. \tag{6.39}$$

If we assume that the axial confinement is symmetric (not necessarily harmonic), and that our spectroscopy averages over an ensemble of ions oscillating in the axial motion with no preferred initial phase of the axial motion (we will later explore the consequences of relaxing this assumption) then the ions will spend the same amount of time on average at any given positive value of α as they do at the corresponding negative value of α, and thus the averaged results yield:

$$< W^{u/\ell}(\mathcal{E}_{\mathrm{rot}}, \mathcal{B}_{\mathrm{rot}}) > + < W^{u/\ell}(\mathcal{E}_{\mathrm{rot}}, -\mathcal{B}_{\mathrm{rot}}) >= 0. \tag{6.40}$$

The combined result, in the absence of exotic particle physics, is zero by symmetry. We did not need to invoke the various approximations that went into Eq. 6.34. In particular, this null result is, unlike the traditional Berry's phase result, not based on the assumption of very small $(\omega_{\mathrm{rot}}/d_{\mathrm{mf}}\mathcal{E}_{\mathrm{rot}})$. Also, for conceptual simplicity we have discussed the result as being based on an average over quasi-static values of α, but the symmetry argument does not hinge on the axial frequency being infinitely slow compared to ω_{rot}.

6.5 Frequency- or Phase-Modulation of Axial Oscillation

The trapped ions will oscillate in the axial direction at a frequency ω_z, confined by an approximately harmonic axial trapping potential $U_z = (1/2)M\omega_z^2 z^2$. Upon moving away from the mid-plane $z = 0$, the ions will experience an oscillating axial electric field $\mathcal{E}_z(t) = -M\omega_z^2 z(t)/e$. The

geometric phase correction to the energy is then $-m_F\omega_{\rm rot}\alpha_{\rm max}\cos(\omega_z t)$, where $\alpha_{\rm max} = \mathcal{E}_{z,\rm max}/\mathcal{E}_{\rm rot}$ is the maximum excursion of the tilt angle. Because the product $\omega_{\rm rot}\alpha_{\rm max}$ is again an energy, it is convenient to redefine the geometric energy contribution in terms of a frequency $\omega_{\rm max}$,

$$\mathrm{E}_{\rm geo} = \omega_{\rm max}\cos(\omega_z t), \tag{6.41}$$

with $\omega_{\rm max} = -\delta m_F\omega_{\rm rot}\alpha_{\rm max}$.

For $\omega_z = 2\pi\times 1$ kHz, an ion cloud temperature of 15 K, an ion whose axial energy E_z is twice the thermal value, for $\omega_{\rm rot}$ as shown in Appendix A, and $\mathcal{E}_{\rm rot} = 5$ V/cm, then a transition such as $W^{u/\ell}$ with $\delta m = 3$ will have a maximum frequency modulation $\omega_{\rm max} = 2\pi\times 400$ Hz.

Thus the electric field undergoes two motions, the comparatively fast radial rotation, and the comparatively slow axial wobble. We exploit the different time scales to create, for each instantaneous value of α, the rotation-dressed states worked out in the previous section. The effect of the axial wobble is then described by the time variation of the amplitudes in these dressed states. The time-dependent Schrödinger equation of motion for this is

$$i\frac{\partial}{\partial t}\begin{pmatrix} a \\ b \end{pmatrix} = \begin{pmatrix} \frac{3}{2}g_F\mu_B\mathcal{B}_{\rm rot} + \frac{\omega_{\rm max}}{2}\cos(\omega_{\rm z}t) & \frac{\Delta}{2} \\ \frac{\Delta}{2} & -\frac{3}{2}g_F\mu_B\mathcal{B}_{\rm rot} - \frac{\omega_{\rm max}}{2}\cos(\omega_{\rm z}t) \end{pmatrix}\begin{pmatrix} a \\ b \end{pmatrix}, \tag{6.42}$$

where a and b are the probability amplitudes for being in the $|a\rangle$ and $|b\rangle$ states, respectively. For typical experimental values, $\omega_{\rm z}$ is about $2\,\pi\times 1\,$kHz, $\omega_{\rm max}$ will range as high as $2\,\pi\times 1000\,$Hz, and Δ (given by Eq. 6.29) is perhaps $2\,\pi\times 2\,$Hz, and $3\mu_B g_F\mathcal{B}_{\rm rot}$ is about $2\,\pi\times 10\,$Hz.

Eqn. 6.42 describes a system again governed by a periodic Hamiltonian, and we will therefore follow a similar course to Chapter 6.4 and search for dressed-state solutions Ψ such that $\Psi(t+n\tau) = e^{-in\phi}\Psi(t)$. Of course, this will only be valid in the limit that $\omega_{\rm rot} \gg \omega_{\rm z}$, a necessary condition to write the time-dependent Hamiltonian in Eqn. 6.42. First, we get rid of fast time-dependence by guessing solutions:

$$a(t) = A(t)\sum_{n=-\infty}^{\infty} J_{\rm n}\left(\frac{\omega_{\rm max}}{2\omega_{\rm z}}\right)e^{-{\rm i}\omega_{\rm z}{\rm n}t} \tag{6.43}$$

$$b(t) = B(t) \sum_{n=-\infty}^{\infty} J_{\mathrm{n}}\left(\frac{-\omega_{\mathrm{max}}}{2\omega_{\mathrm{z}}}\right) e^{-\mathrm{i}\omega_{\mathrm{z}}\mathrm{nt}},$$

where J_{n} are Bessel's functions of the first kind and A(t) and B(t) are slowly varying functions. We then substitute our trial solutions into Eqn. 6.42 and use the recurrence relation $(2n/x)J_{\mathrm{n}}(x) = J_{\mathrm{n}-1}(x) + J_{\mathrm{n}+1}(x)$. We multiply through by $\sum_{n'=-\infty}^{\infty} J_{\mathrm{n}'}\left(\frac{\omega_{\mathrm{max}}}{2\omega_{\mathrm{z}}}\right) e^{i\omega_{\mathrm{z}}n't}$ and $\sum_{n'=-\infty}^{\infty} J_{\mathrm{n}'}\left(\frac{-\omega_{\mathrm{max}}}{2\omega_{\mathrm{z}}}\right) e^{i\omega_{\mathrm{z}}n't}$ as appropriate. We then integrate over an axial time period, $2\pi/\omega_{\mathrm{z}}$, and make the approximation that A(t) and B(t) are unchanged over this small time interval. This approximation should be good as long as $\omega_{\mathrm{z}} \gg \omega_{\mathrm{max}}$ and $\omega_{\mathrm{z}} \gg g_F\mu_B\mathcal{B}_{\mathrm{rot}}$. The integration then yields,

$$i\frac{\partial}{\partial t}\begin{pmatrix} A \\ B \end{pmatrix} = \begin{pmatrix} \frac{3}{2}g_F\mu_B\mathcal{B}_{\mathrm{rot}} & \frac{\Delta_{\mathrm{eff}}}{2} \\ \frac{\Delta_{\mathrm{eff}}}{2} & -\frac{3}{2}g_F\mu_B\mathcal{B}_{\mathrm{rot}} \end{pmatrix}\begin{pmatrix} A \\ B \end{pmatrix} \tag{6.44}$$

with

$$\Delta_{\mathrm{eff}} = \sum_{n=-\infty}^{\infty} J_{\mathrm{n}}\left(\frac{\omega_{\mathrm{max}}}{2\omega_{\mathrm{z}}}\right) J_{\mathrm{n}}\left(\frac{-\omega_{\mathrm{max}}}{2\omega_{\mathrm{z}}}\right)\Delta = J_0(\frac{\omega_{\mathrm{max}}}{\omega_{\mathrm{z}}})\Delta. \tag{6.45}$$

This results in dressed-state energies, now as a function of $\mathcal{B}_{\mathrm{rot}}$, and not α, as seen in Fig. 6.3. This clearly shows the requirement of $3g_F\mu_B\mathcal{B}_{\mathrm{rot}} > \Delta_{\mathrm{eff}}$ in order to keep $|a\rangle$ and $|b\rangle$ as the dressed states. This is true despite the fact that an ion will sample the avoided crossing in Fig. 6.2 during its axial oscillation in the trap, as $\omega_{\mathrm{max}} \gg 3g_F\mu_B\mathcal{B}_{\mathrm{rot}}$ in our experiment. Δ_{eff} will have a maximum value of Δ at $\omega_{\mathrm{max}}/\omega_{\mathrm{z}} = 0$ and will oscillate about zero according to $J_0(\omega_{\mathrm{max}}/\omega_{\mathrm{z}})$.

For finite $\omega_{\mathrm{max}}/\omega_{\mathrm{z}}$, the dressed states from Eqn. 6.44 only appear stationary if measured at integer multiples of the axial trapping period, $2\pi/\omega_{\mathrm{z}}$. Consider states $|+\rangle$ and $|-\rangle$, symmetric and antisymmetric combinations of states $|a\rangle$ and $|b\rangle$, respectively. In the limit that $\delta m_F g_F\mu_B\mathcal{B}_{\mathrm{rot}} \gg \Delta_{\mathrm{eff}}$, an ion initially in state $|+\rangle$ will oscillate between $|+\rangle$ and $|-\rangle$ at the precession frequency $\omega_0 = ((3g_F^{u/\ell}\mu_B\mathcal{B}_{\mathrm{rot}} + d_e\mathcal{E}_{\mathrm{eff}})^2 + \Delta_{\mathrm{eff}}^2)^{\frac{1}{2}}$, when measured at integer multiples of the axial trapping frequency. However, if our EDM measurement is made after a non-integer number of axial oscillations, or if the ions have different axial frequencies in the trap, the $|+\rangle$ to $|-\rangle$ oscillation will be frequency modulated at ω_{max} (see Fig. 6.4). For the example parameters, the frequency-modulation index

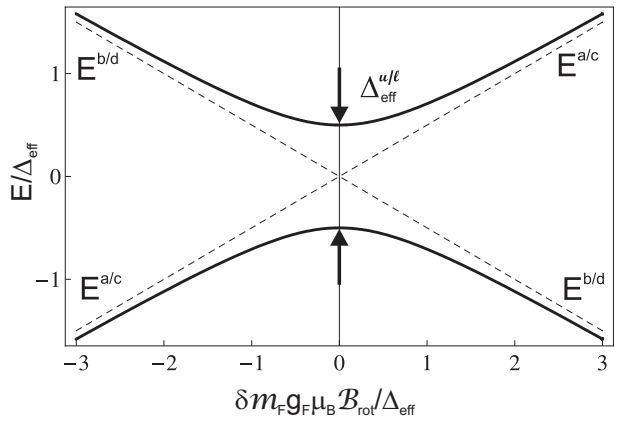

Figure 6.3: The apparent energy shifts between $m_F = +3/2$ and $m_F = -3/2$ states in upper (a,b) and lower (c,d) Λ-doublet levels versus $\mathcal{B}_{\rm rot}$,"dressed" by both the electric field rotation ($\omega_{\rm rot}$) and by the ion's axial trap oscillation (ω_z). At $\mathcal{B}_{\rm rot} = 0$, there is an avoided crossing that mixes $m_F = \pm 3/2$ states, with an energy splitting at the crossing of $\Delta_{\rm eff}^{u/\ell}$. In the limit $\delta m_F g_F \mu_B \mathcal{B}_{\rm rot} \gg \Delta_{\rm eff}$, the dressed states are of good m_F with an energy splitting slightly modified by $\Delta_{\rm eff}$.

$\omega_{\rm max}/\omega_z$ is less than 1, and thus the spectral power of transition is overwhelmingly at ω_0, the quantity which symmetry arguments above show is unaffected by Berry's phase. In an ensemble of ions which have a random distribution of initial axial motions, the sidebands on the transition average to zero, and won't pull the frequency of the measured central transition. If instead the process of loading ions into the trap has left the ions with an initial nonzero axial velocity or axial offset from trap center, the measured frequency can be systematically pulled from ω_0.

Note that increasing $\mathcal{E}_{\rm rot}$ or decreasing $\omega_{\rm rot}$ reduces the value of $\omega_{\rm max}$ and thus the frequency modulation index. On the other hand, these changes also would have the effect of increasing the energy $\mathrm{E_{micro}}$ of the micromotion of the ions in the rotating fields. For harmonic axial confinement, we find the frequency modulation for a $\delta m = 3$ transition obeys the following relation $\omega_{\rm max}/\omega_z = 3(\mathrm{E}_z/\mathrm{E_{rot}})^{1/2}$. Thus to keep the modulation safely under unity for a comfortable majority of an ensemble of ions with an average E_z given by T_z, one needs to choose operating parameters such that $\mathrm{E_{rot}} > 30 k_B T_z$. This inequality in turn places stringent requirements on the spatial uniformity of $\mathcal{E}_{\rm rot}$. On a time-scale slow compared to $1/\omega_{\rm rot}$, $\mathcal{E}_{\rm rot}$ acts like a sort of ponderomotive potential analogous to the effective confining potential in a Paul trap. If $\mathrm{E_{rot}} = 30 k_B T_z$, then a spatial inhomogeneity in $\mathcal{E}_{\rm rot}$ of only 1.5% already gives rise to structure in the ponderomotive potential comparable to T_z.

To summarize the effect of axial motion: in the limit $3 g_F \mu_B \mathcal{B}_{\rm rot} > \Delta$, ions prepared, for instance by optical pumping, in state $|a\rangle$ (or $|b\rangle$) will remain in $|a\rangle$ (or $|b\rangle$). The energy difference between dressed states which are predominantly either $|a\rangle$ or $|b\rangle$ will be slightly modified by the avoided crossing. But the important combined measurement described by Eq. (6.34) will continue to yield zero in the absence of EDM signal, and the sensitivity of that combined measurement to the EDM signal will not be much affected as long as $\omega_{\rm max}/\omega_z <\approx 1$.

6.6 Creating Coherent Mixtures of $m_F = +3/2$ and $m_F = -3/2$

The above discussion reveals a possible way to deal with an experimental issue. The Ramsey-type experiment we wish to perform in order to measure d_e requires a coherent superposition of

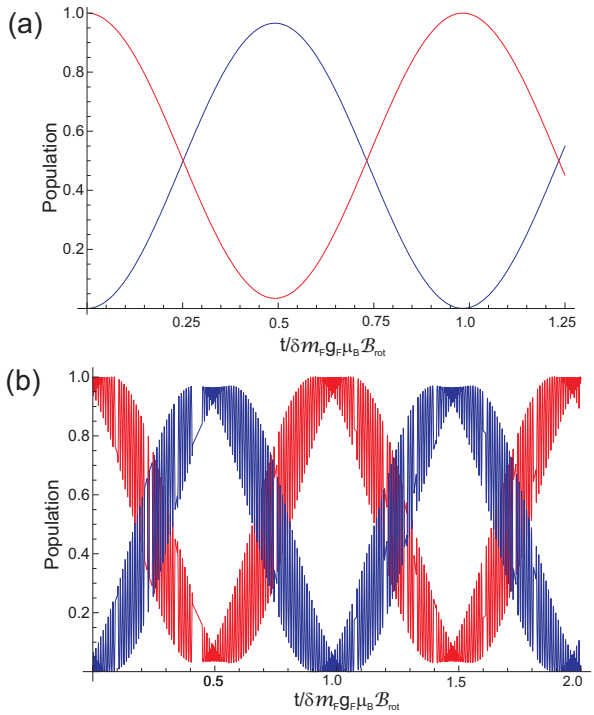

Figure 6.4: Population of states $|+\rangle$ (red) and $|-\rangle$ (blue) with parameters $\omega_z = 2\pi \times 1000\,\mathrm{Hz}$, $\omega_{\max} = 2\pi \times 500\,\mathrm{Hz}$, $\Delta = 2\pi \times 2\,\mathrm{Hz}$, and $\delta m_F g_F^{u/\ell} \mu_B \mathcal{B}_{\mathrm{rot}} = \pi \times 10\,\mathrm{Hz}$. The population is initially prepared in $|+\rangle$ and results were found by numerically integrating Eq. 6.42. (a) Measured at integer periods of ω_z the $|a\rangle$ and $|b\rangle$ states appear stationary, leading to smooth Rabi oscillations if the state is prepared in state $|+\rangle$ or $|-\rangle$. (b) If the measurement cannot be made at integer periods of ω_z, frequency modulation at $\omega_{\max}$ is observed, leading to reduced accuracy when measuring the precession frequency. Note here that $\omega_{\max}/\omega_z = 1/2$. As discussed in Chapter 6.11, similar modulation can arise from static, uniform magnetic fields that are averaged over during a period of ω_{rot}.

electron spin up and spin down states. One possible way of achieving this is to start with ions in the $^1\Sigma$, F = ± 1/2 states and then populate the $^3\Delta_1$, J = 1, m_F = ± 3/2 states using STIRAP, similar to the discussion in Chapter 5.7. The quantum beat signal from the radiative decay could be measured, or another STIRAP could be performed and the transfer percentage measured. As discussed in Chapter 5.7, STIRAP could prove challenging with our weak transitions and large ion clouds.

Typically, when performing a Ramsey measurement between magnetic sub-levels, a $\pi/2$ pulse is performed with rf photons. If the ions can be created directly in the $^3\Delta_1$, J = 1 state through autoionization as described in Chapter 5.7.3, a statistical mixture of m_F levels would exist. Optical depletion of all but the $m_F = +3/2$ level could be done with σ^+ polarized light driving a transition with a small decay branching fraction back to the $^3\Delta_1$ level. For our case of F = 3/2 states, our $\pi/2$ pulse would have to come from a three-photon transition.

A typical JILAn laughs in the face of a challenge such as three-photon rf transitions. However, the preceding section points to another possible solution. The coupling need not be performed by an rf photon field, instead the rotational electric field can create the coupling, as seen by the quantity Δ above. After the other spin levels have been optically depleted, Δ_{eff} can be ramped up to some value much larger than $3g_F\mu_B\mathcal{B}_{\text{rot}}$, by decreasing the value of $\mathcal{E}_{\text{rot}}$. After waiting a time $1/(2\Delta_{\text{eff}})$ and ramping back to $\Delta_{\text{eff}} < 3g_F\mu_B\mathcal{B}_{\text{rot}}$, the m_F= +3/2 population can be coherently transferred to an equal superposition of m_F = ± 3/2 states. The spin is then allowed to precess at the frequency $\omega_0 = ((3\mathcal{B}_{\text{rot}}g_F^{u/\ell}\mu_B + d_e\mathcal{E}_{\text{eff}})^2 + \Delta_{\text{eff}}^2)^{\frac{1}{2}}$ for some time τ, Δ_{eff} is again ramped to perform the second $\pi/2$ pulse of the Ramsey sequence, and the final spin population can be read out as discussed in Chapter 4.

6.7 Structure of the Measurements. What Quantities Matter

In the remainder of this section, the possible effects of various experimental imperfections on our measurement are explored.

The symmetry argument in Chapter 6.2 presupposes the ability to impose a perfect "$\mathcal{B}$-chop",

i.e., to collect data with alternating measurements changing quite precisely only the sign of $\mathcal{B}_{\rm rot}$. If not only the sign but the magnitude of the rotating magnetic field alternates, the situation is more complicated. There will likely be contributions to the rotating magnetic field that are not perfectly reversed in our $\mathcal{B}$-chop, including displacement currents associated with sinusoidally charging the electrodes that create the rotating electric field. These effects can be quantified with a value $\mathcal{B}_{\rm rot}^{\rm stray}$, and to lowest order they would appear as a frequency offset in the chopped measurement:

$$W^{u/\ell}(\vec{\mathcal{E}}, \vec{\mathcal{B}}_{\rm rot} + \vec{\mathcal{B}}_{\rm rot}^{\rm stray}) + W^{u/\ell}(\vec{\mathcal{E}}, -\vec{\mathcal{B}}_{\rm rot} + \vec{\mathcal{B}}_{\rm rot}^{\rm stray}) = 6 g_F^{u/\ell} \mu_B \mathcal{B}_{\rm rot}^{\rm stray} \pm 2 d_e \mathcal{E}_{\rm eff} \tag{6.46}$$

This offset is very nearly the same for the upper and lower states, to the extent that $g_F^u \approx g_F^\ell$, i.e., to the extent that $\delta g_F \equiv 1/2(g_F^u - g_F^\ell) \ll g_F$. The effect of the stray field is reduced by combining measurements from the upper and lower states, in the form of a "four-way chop":

$$\begin{aligned}&\Big[W^u(\vec{\mathcal{E}}_{\rm rot}, \vec{\mathcal{B}}_{\rm rot} + \vec{\mathcal{B}}_{\rm rot}^{\rm stray}) + W^u(\vec{\mathcal{E}}_{\rm rot}, -\vec{\mathcal{B}}_{\rm rot} + \vec{\mathcal{B}}_{\rm rot}^{\rm stray})\Big] \\ &- \Big[W^\ell(\vec{\mathcal{E}}_{\rm rot}, \vec{\mathcal{B}}_{\rm rot} + \vec{\mathcal{B}}_{\rm rot}^{\rm stray}) + W^\ell(\vec{\mathcal{E}}_{\rm rot}, -\vec{\mathcal{B}}_{\rm rot} + \vec{\mathcal{B}}_{\rm rot}^{\rm stray})\Big] = 12 \delta g_F \mu_B \mathcal{B}_{\rm rot}^{\rm stray} + 4 d_e \mathcal{E}_{\rm eff}\end{aligned} \tag{6.47}$$

It may prove to be advantageous to shim the $\mathcal{B}$-chop by deliberately adding a non-chopped rotating magnetic field, $\mathcal{B}_{\rm rot}^{\rm shim}$, and adjusting its value until experimentally we measure

$$W^u(\mathcal{B}_{\rm rot} + \mathcal{B}_{\rm rot}^{\rm stray} + \mathcal{B}_{\rm rot}^{\rm shim}) + W^u(-\mathcal{B}_{\rm rot} + \mathcal{B}_{\rm rot}^{\rm stray} + \mathcal{B}_{\rm rot}^{\rm shim}) = 0. \tag{6.48}$$

Then, a measurement in the lower Λ-doublet state gives

$$W^\ell(\mathcal{B}_{\rm rot} + \mathcal{B}_{\rm rot}^{\rm stray} + \mathcal{B}_{\rm rot}^{\rm shim}) + W^\ell(-\mathcal{B}_{\rm rot} + \mathcal{B}_{\rm rot}^{\rm stray} + \mathcal{B}_{\rm rot}^{\rm shim}) = -2(1 + \frac{g_F^\ell}{g_F^u}) d_e \mathcal{E}_{\rm eff}, \tag{6.49}$$

yielding a still more accurate value for $4 d_e \mathcal{E}_{\rm eff}$.

What we care about most then are: (1) Things that perturb W^u and W^ℓ differently, in particular the quantity δg_F, but also the analogous electrical quantity, $\delta\eta$, to be defined and estimated in Chapter 6.9, and (2) to a lesser extent, we care about effects which affect $W^u(\mathcal{B}_{\rm rot}) + W^u(-\mathcal{B}_{\rm rot})$ the same way as they affect $W^\ell(\mathcal{B}_{\rm rot}) + W^\ell(-\mathcal{B}_{\rm rot})$, because, to the extent that they lead to a measurement

$$W^u(\mathcal{B}_{\rm rot}) + W^u(-\mathcal{B}_{\rm rot}) = +2 d_e \mathcal{E}_{\rm eff} + \delta_{\rm syst}, \tag{6.50}$$

we can mistake a nonzero value for $\delta_{\rm syst}$ as an indicator for a nonzero value of $\mathcal{B}_{\rm rot}^{\rm stray}$. In that case, the shimming procedure discussed above to remove $\mathcal{B}_{\rm rot}^{\rm stray}$ would lead to a combined result from the four-way chop of $4d_e\mathcal{E}_{\rm eff} + (4\delta g_F/g_F)\delta_{\rm syst}$. This is down by a relative factor of $(\delta g_F/g_F)$ compared to the effects that differentially perturb W^u versus W^ℓ, but they could still be troublesome. And (3) to a still lesser extent, we care about imperfections that perturb individual measurements such as $W^u(\mathcal{B}_{\rm rot})$, even if they do not perturb the $\mathcal{B}$-chop measurement, $W^u(\mathcal{B}_{\rm rot}) - W^u(-\mathcal{B}_{\rm rot})$, because, to the extent that they vary over time, or depend on the trajectory of an individual ion in the trap, they can reduce coherence times. This leads not to systematic errors, but to a reduction in the overall precision.

In addition to the $\mathcal{B}$ chop, state chop, and four-way chop discussed above, we can perform a rotation chop, by changing the sign of $\omega_{\rm rot}$. Our hope is to keep experimental imperfections to a level where the four-way chop is by itself already good enough to suppress systematic error below the desired level. Then repeating the entire series of measurements with the opposite sign of $\omega_{\rm rot}$ (rotating the field CW instead of CCW) will to the extent it yields the same final value of $4\mathcal{E}_{\rm eff}d_e$ provide a useful redundant check.

6.8 An Estimate of $\delta g_{F=3/2}$

There are three leading contributions to $\delta g_{F=3/2}$ in our molecule: a zero field difference, a difference due to static electric fields, and a difference due to rotating electric fields. The zero field difference is due to terms omitted in the Zeeman Hamiltonian in Eq. 6.13. For our molecule, these terms give rise to a difference in $g_{F=3/2}$ in terms of the Λ-doubling J = 1 energy splitting $\omega_{\rm ef}$ [113],

$$\frac{\delta g_{F=3/2}}{g_{F=3/2}} \approx \left|\frac{\omega_{\rm ef}}{B_e g_{F=3/2}}\right|. \tag{6.51}$$

This is on the order of 10^{-5} for HfF^+.

The electric field dependent g-factor arises due to the mixing of rotational levels J in the molecule. The levels with $J = 2$, while far away in energy compared to the Stark energy $d_{\rm mf}\mathcal{E}_{\rm rot}$, are perturbers. In the signed Ω basis, the m_F sub-levels in the $J = 2$ level have a smaller γ_F value

than do the m_F sub-levels in the $J = 1$ level. Therefore, the states which go up (down) in energy in the $J = 1$ level "gain" ("run") on (from) the $J = 2$ level. When one includes the effects of Hyperfine interactions, there are multiple connections to each sub-level. In the $J = 1$, $m_F = \pm 3/2$ levels that we are interested in this contribution is [113],

$$\frac{\delta g_{F=3/2}}{g_{F=3/2}}(\mathcal{E}_{\rm rot}) = \frac{9\ d_{\rm mf}\mathcal{E}_{\rm rot}}{40\ B_e}, \tag{6.52}$$

which gives a fractional shift $\delta g_{F=3/2}/g_{F=3/2}$ of a few 10^{-4}. The same approach gives that the electric field "g" factor, γ_F, will shift in the same manner such that $\delta\gamma_F/\gamma_F \approx 10^{-4}$.

For rotating fields, another contribution to δg_F arises from non-vanishing value of $\omega_{\rm rot}/(d_{\rm mf}\mathcal{E}_{\rm rot})$. The states with $\Omega = 1$ and $\Omega = -1$ are equally affected by the rotating field since they have an equal Stark shift in the absence of hyperfine interactions. However, because the levels with $|F = 3/2, m_F = \pm 1/2\rangle$ are repelled by the lower $|F = 1/2, m_F = \pm 1/2\rangle$ states, the effective Stark difference between m_F levels with $\Omega = -1$ (upper levels) is smaller than the same m_F levels with $\Omega = +1$ (lower levels). The scale at which this difference will appear is then determined by how much the lower hyperfine state pushes on the upper due to the coupling induced by the electric field.

$$\frac{\delta g_{F=3/2}}{g_{F=3/2}} = \frac{\sqrt{6}}{\gamma^2_{F=3/2}}\frac{\omega^2_{\rm rot}}{d_{\rm mf}\mathcal{E}_{\rm rot}{\rm E}_{\rm hf}}. \tag{6.53}$$

This fractional shift is of the order a few 10^{-4} and is therefore about the same magnitude as the electric field induced mixing of higher rotational levels.

6.9 Dependencies on $\mathcal{E}_{\rm rot}$

Proximity to the avoided crossing shown in Fig. 6.2(b) means that the transitions W^u and W^ℓ will have residual dependencies on $\mathcal{E}_{\rm rot}$, which in turn may lead to decoherence or systematic errors. We characterize the sensitivity of $W^{u/\ell}$ to small changes in $\mathcal{E}_{\rm rot}$ with the following expansion

$$W^{u/\ell}(\mathcal{E}^0_{\rm rot} + \delta\mathcal{E}_{\rm rot}, \mathcal{B}_{\rm rot}) = W^{u/\ell}(\mathcal{E}^0_{\rm rot}, \mathcal{B}_{\rm rot}) + \eta^{u/\ell}\delta\mathcal{E}_{\rm rot} \tag{6.54}$$

with

$$\eta^{u/\ell} \equiv \frac{\partial W^{u/\ell}}{\partial \mathcal{E}_{\rm rot}}|_{\mathcal{E}^0_{\rm rot},\mathcal{B}_{\rm rot}} = \frac{-(\Delta^{u/\ell})^2}{g_F^{u/\ell}\mu_B \mathcal{B}_{\rm rot}\mathcal{E}_{\rm rot}}, \tag{6.55}$$

using the expressions in Eqs. (6.29) and (6.33). Any spatial inhomogeneity in $\mathcal{E}_{\rm rot}$ that does not average away with ion motion will lead to a decoherence rate given approximately by $\eta\delta\mathcal{E}_{\rm rot}$.

In terms of systematic errors, if chopping the sign of $\mathcal{B}_{\rm rot}$ gives rise to an unintended systematic change in the magnitude of $\mathcal{E}_{\rm rot}$ (call it $\delta\mathcal{E}_{\rm chop}$), for instance due to motional fields discussed later, or due to ohmic voltages generated by the eddy currents, then there will be a frequency shift in a $\mathcal{B}$-chop combination, $2\eta^{u/\ell}\delta\mathcal{E}_{\rm chop}$. To the extent that $\delta\eta = \frac{1}{2}(\eta^u - \eta^\ell)$ is nonzero, some of this shift will survive a four-way chop as well. The dominant contribution to $\delta\eta$ is likely from $\delta\Delta$, rather than from δg_F. Assuming this limit, the systematic error surviving is

$$8\frac{\delta\Delta}{\Delta}\eta\delta\mathcal{E}_{\rm chop} \approx 6\left(\frac{d_{\rm mf}\mathcal{E}_{\rm rot}}{\rm E_{hf}}\right)^2 \eta\delta\mathcal{E}_{\rm chop}. \tag{6.56}$$

For a large but not inconceivable value for $\delta\mathcal{E}_{chop}$ of 100 μV/cm, and for other values as in Appendix A, this works out to comfortably less than 100 μHz, and is therefore not a problem. But this error would scale as $\mathcal{E}_{\rm rot}^{-5}$, and thus could cause trouble if for other reasons we chose to decrease $\mathcal{E}_{\rm rot}$. The science signal is roughly independent of $\mathcal{E}_{\rm rot}$, which should allow for the source of error to be readily identified.

6.10 Perpendicular $\mathcal{B}$-Fields

The quantization axis is essentially defined by $\mathcal{E}_{\rm rot}$. The shift of the various levels $|a\rangle$, $|b\rangle$, $|c\rangle$, $|d\rangle$ due to a component of the magnetic field perpendicular to $\mathcal{E}_{\rm rot}$ is on the order of

$$\pm\frac{3}{4}\frac{(g_F\mu_B\mathcal{B}_\perp)^2}{(\gamma_F d_{\rm mf}\mathcal{E}_{\rm rot})} \tag{6.57}$$

for the upper/lower states. In the absence of rotation, the lowest-order correction to $W^{u/\ell}(\mathcal{B}_{\rm rot})$ goes as

$$-\frac{3}{2}\frac{g_F^3\mu_B^3\mathcal{B}_\perp^2\mathcal{B}_{\rm rot}}{(\gamma_F d_{\rm mf}\mathcal{E}_{\rm rot})^2}. \tag{6.58}$$

For reasonable experimental parameters, this will be a negligible number. The lowest-order correction to the state-chop combination, $W^u(\mathcal{B}_{\rm rot}) - W^\ell(\mathcal{B}_{\rm rot})$ is smaller still and goes as

$$\frac{3}{2}\frac{g_F^3\mu_B^3\mathcal{B}_\perp^2\mathcal{B}_{\rm rot}}{\gamma_F d_{\rm mf}\mathcal{E}_{\rm rot}\ {\rm E_{hf}}}. \tag{6.59}$$

It is similar in form to the difference in g-factors caused by the rotation of the field.

When we turn on rotation, there is an additional larger contribution to $W^{u/\ell}(\mathcal{B}_{\rm rot})$. If we assume (as a worst case) that $\mathcal{B}_\perp$ is purely axial, not azimuthal, then the lowest-order effect of $\mathcal{B}_\perp$ is to tilt the quantization axis by angle given by

$$\frac{\pm g_F\mu_B\mathcal{B}_\perp}{(\gamma_F d_{\rm mf}\mathcal{E}_{\rm rot} \pm \mu_B g_F\mathcal{B}_{\rm rot})}, \tag{6.60}$$

with the +(-) in the numerator corresponding to the upper(lower) states and the +(-) in the denominator corresponding to the Ω = -1(+1) states. This has the leading order effect on $W^{u/\ell}$ of

$$\frac{3\omega_{\rm rot}g_F^2\mu_B^2\mathcal{B}_\perp\mathcal{B}_{\rm rot}}{(\gamma_F d_{\rm mf}\mathcal{E}_{\rm rot})^2} \tag{6.61}$$

even a rudimentary nulling of the Earth's magnetic field, say to below 25 mG, will leave this term negligible, for parameters in Appendix A. Its contribution to the state chop, $W^u(\mathcal{B}_{\rm rot}) - W^\ell(\mathcal{B}_{\rm rot})$, is still smaller by $d_{\rm mf}\mathcal{E}_{\rm rot}/{\rm E_{hf}}$

$$\frac{\omega_{\rm rot}g_F^2\mu_B^2\mathcal{B}_\perp\mathcal{B}_{\rm rot}}{\gamma_F d_{\rm mf}\mathcal{E}_{\rm rot}{\rm E_{hf}}} \tag{6.62}$$

6.11 Stray Contributions to $\mathcal{B}_{||}$: Uniform or Time-Varying $\mathcal{B}$-Fields

In the previous section we've seen that the effects of $\mathcal{B}_\perp$ are small. Spatial or shot-to-shot variation in $\mathcal{B}_{||}$, on the other hand, can limit coherence time through its contribution to $W^{u/\ell}$. The biggest contribution to $\mathcal{B}_{||}$ is of course the intentionally applied rotating field $\mathcal{B}_{\rm rot}$. Let us examine the various other contributions to $\mathcal{B}_{||}$.

Static, uniform fields: $\mathcal{B}$ fields of this nature are relatively harmless. $\mathcal{B}_{||}$ is defined relative to the quantization axis $\hat{\mathcal{E}}_{\rm rot}$. The time-average of $\mathcal{B}_{||}$ is $\langle\mathcal{B}_{||}\rangle = \langle\vec{\mathcal{B}}\cdot\hat{\mathcal{E}}_{\rm rot}\rangle$. Since $\hat{\mathcal{E}}_{\rm rot}$ sweeps out a circle with angular velocity $\omega_{\rm rot}$, the contribution to the time-averaged $\mathcal{B}_{||}$ from a uniform, static

magnetic field averages nearly to zero in a single rotation of the bias electric field, and still more accurately after a few cycles of axial and radial motion in the trap. The average electric field in the ion trap must be very close to zero, or the ions would not remain trapped. In the case of certain anharmonicities in the trapping potential, however, one can find that the average value of $\hat{\mathcal{E}}_{\rm rot}$ is nonzero, even if the average value of $\vec{\mathcal{E}}_{\rm rot}$ is zero. For instance, an electrostatic potential term proportional to z^3, along with a uniform axial magnetic field $\mathcal{B}_z$, will for an ion with nonzero axial secular motion, yield a nonzero $\langle \mathcal{B}_{||} \rangle$. In addition, nonzero $\mathcal{B}_z$ will interact with the tilt of $\vec{\mathcal{E}}_{\rm rot}$ oscillating with an ion's axial motion at ω_z to cause a frequency modulation similar to the one discussed in Chapter 6.5. A uniform magnetic field in the x-y plane will cause a frequency modulation at $\omega_{\rm rot}$. If the modulation index for either of these modulations approaches one, the modulation will begin to suppress the contrast of spectroscopy performed at the carrier frequency. For uniform magnetic fields with amplitude less than 10 mG (achievable for instance by roughly nulling the earth's field with Helmholtz coils), frequency modulation indices will be small, and, barring pathologically large z^3 electrostatic terms, the mean shifts from uniform, static $\mathcal{B}$-fields will be less than 1 Hz and can be can be dealt with by means of an applied $\mathcal{B}_{\rm rot}^{\rm shim}$ as discussed in Chapter 6.7.

Time-varying magnetic fields with frequency near $\omega_{\rm rot}$ can cause more trouble. If the time between the two Ramsey pulses used to interrogate the frequency is $t_{\rm Ramsey}$, then the dangerous bandwidth is $1/t_{\rm Ramsey}$, centered on $\omega_{\rm rot}$. We discuss in order (i) thermally generated fields from the electrodes, (ii) ambient magnetic field noise in laboratory, (iii) magnetic fields associated with the application of $\mathcal{E}_{\rm rot}$, oscillating coherently with $\mathcal{E}_{\rm rot}$, (iv) shot to-shot variation in magnitude of applied $\mathcal{B}_{\rm rot}$, and (v) spatial inhomogeneities in $\mathcal{B}_{\rm rot}$.

(i) Proposed EDM experiments on trapped atomic species such as Cesium are vulnerable to magnetic field noise generated by thermally excited currents in conductors located close to the trapped species [118]. In our case, the effect is less worrisome because, vis-a-vis the trapped atom experiments, our bandwidth of vulnerability is centered at much higher frequency fields, because our molecules are trapped considerably further from the nearest conductors, and because the sensitivity

of our measurement of d_e to magnetic field noise, which goes as $g_F\mu_B/\mathcal{E}_{\rm eff}$ is down by a factor of 10^4. The spectral density of thermal magnetic field noise (which is calculated in reference [119] in the simplified geometry of a semi-infinite planar conductor) will surely be less than 1 pG/Hz$^{1/2}$ in our bandwidth of vulnerability. This effect is negligible.

(ii) Like thermal magnetic noise, technical magnetic noise in our lab arising for instance from various nearby equipment will not so much decohere an individual measurement as generate shot-to-shot irreproducibility between measurements. What level of noise are we sensitive to? As we discuss in Sec 8, the precision of a single trap load is unlikely to be better than 300 mHz, meaning magnetic field noise less than 0.2 μG/Hz$^{1/2}$ won't hurt us, for a 1 s interrogation time. Measurements made in our lab show that there are a number of magnetic field "tones" of very narrow bandwidth, associated with harmonics of 60 Hz power and various power supplies. As long as we choose $\omega_{\rm rot}$ to not coincide with one of these frequencies, in the range of 50 kHz to 300 kHz ambient magnetic frequency noise in our lab has spectral density typically less than 0.02 μG/Hz$^{1/2}$. For this reason, at least for the first generation experiment, there will be no explicit effort to shield ambient magnetic field other than to use Helmholtz coils to roughly null the earth's dc field. The steel vacuum chamber will in addition provide some shielding at 100 kHz.

(iii) In traditional eEDM experiments, one of the most difficult unwanted effects to characterize and bring under control is magnetic fields generated by leakage currents associated with the high voltages on the electrodes that generate the principal electric field. In our case the bulk of the electric field $\mathcal{E}_{\rm eff}$ is generated inside the molecule. The laboratory electric fields are measured in V/cm, not kV/cm, and leakage currents as traditionally conceived will not be a problem for us. On the other hand, the electric field does rotate at hundreds of kHz, and thus the electrode potentials must constantly oscillate. Displacement currents in the trapping volume between the electrodes, and real currents in the electrodes themselves and in the wire leads leading to them, will generate magnetic fields with spatial gradients and strengths that oscillate coherently with $\mathcal{E}_{\rm rot}$ at the frequency $\omega_{\rm rot}$.

The spatial structure of the oscillating magnetic fields will depend on the geometry of the

electrodes and in particular on the layout of the wire leads that provide the current to charge them. In principle, shim coils can be constructed just outside the trap electrodes and driven with various phases and amplitude of current oscillating at $\omega_{\rm rot}$, all in order to further control the shape of the magnetic field. The one immutable fact is the Maxwell equation, $\nabla \times \vec{\mathcal{B}} = c^{-2}\partial\vec{\mathcal{E}}/\partial t$.

The dominant time dependence of the electric field is from the spatially uniform rotating field, and thus for a circular field trajectory, the dominant contribution to the magnetic field structure goes as

$$\nabla \times \vec{\mathcal{B}} = k\hat{y}' \tag{6.63}$$

with

$$\begin{aligned} k &= c^{-2}\mathcal{E}_{\rm rot}\omega_{\rm rot}, & (6.64)\\ &= 350\ \text{nG/cm} \times \left(\frac{\omega_{\rm rot}}{2\pi \times 100\ \text{kHz}}\right)\left(\frac{\mathcal{E}_{\rm rot}}{5\ \text{V/cm}}\right), & (6.65) \end{aligned}$$

where $\hat{y}'$ is the direction in the x-y plane orthogonal to the instantaneous electric field.

The curl determines only the spatial derivatives of $\mathcal{B}$; $\mathcal{B}$ itself only depends on the boundary conditions. An idealized arrangement of current carrying leads and shim coils could in principle force the $\mathcal{B}$ field to be

$$\vec{\mathcal{B}}^{\rm ideal} = kx'\hat{z}. \tag{6.66}$$

where k is given by Eq. 6.64 and x' is displacement in the x-y plane along the direction of the instantaneous rotating electric field. These fields would be perpendicular to the quantization axis provided by the electric field, and would have negligible effect on the transitions of interest.

While realizing such an idealized displacement field would be very difficult, there are relatively simple steps to take to minimize the displacement fields. For instance, each rod-like electrode can be charged up by two leads, one connected to each end of the rod, with the leads running along respective paths symmetric in reflection in the z=0 plane to a common oscillating voltage source outside of the vacuum can, at z=0. It is worth considering a maximally bad electrode layout, to put a limit on worst-case performance. Our electrodes will be spaced by about 10 cm and mounted in

such a way that their capacitance to each other or to ground will be at worst 5 pF. If the charging current is provided entirely by a single lead connected to one end of the rod, the peak current running down the rod near its center will be 80 μA, leading to a worst-case field magnitude at the trap center of about 20 μG, and a contribution to $W^{u/\ell}$ of perhaps 2.5 Hz. Spatial gradients of this effect, and shot-to-shot irreproducibility of this effect will not contribute to decoherence at the 0.1 Hz level. As for its contribution to systematic error, this shift will survive the $\mathcal{B}$-chop, but will be suppressed in the four-way chop by the factor $(\delta g_F/g_F)$, perhaps a factor of a thousand. For still better accuracy the shift should be nulled out of the $\mathcal{B}$-field chop by adjusting $\mathcal{B}_{\rm rot}^{\rm shim}$, as discussed in Chapter 6.7.

(iv)Given that the main effect of $\mathcal{B}_{\rm rot}$ is to apply an offset frequency, $3g_F\mu_B\mathcal{B}_{\rm rot}$ of perhaps 8 Hz, and given that (see Sec 8) the single-shot precision is unlikely to be any better than 300 mHz, the shot-to-shot reproducibility of $\mathcal{B}_{\rm rot}$ need be no better than a part in 30, a very modest requirement on stability. Decoherence then is not a problem, but a potential source of systematic error arises if the the $\mathcal{B}$-chop is not "clean" that is if $\mathcal{B}_{\rm rot}$ before the chop is not exactly equal to $-\mathcal{B}_{\rm rot}$ after the chop. This sort of error could arise for instance from certain offset errors in op-amps generating the oscillating current. Experimentally, one adjusts $\mathcal{B}_{\rm rot}^{\rm shim}$ to cancel these offsets, but even in the absence of that procedure, the four-way chop cleans up these sorts of errors. For a rather egregious fractional deviation from $\mathcal{B}$-chop cleanliness of, for instance, 1%, and for $(\delta g_F/g_F) < .001$, the systematic error remaining after the four-way chop is 10^{-5} of the offset frequency of perhaps 8 Hz. In HfF^+ this is a systematic error on d_e of 10^{-29} e cm. For ThF^+ the error as referred to d_e is smaller still, and of course if we avail ourselves of $\mathcal{B}_{\rm rot}^{\rm shim}$ so as to null the post $\mathcal{B}$-chop signal to <100 mHz, the systematic error on d_e will be considerably less than 10^{-29} e cm for either species.

(v) The largest single contribution to decoherence (with the exception of spontaneous decay of the $^3\Delta_1$ line to a lower electronic state) will likely be due to spatial inhomogeneity in the applied rotating bias field $\mathcal{B}_{\rm rot}$. That is to say, spatial inhomogeneities in $\vec{\mathcal{B}}$ that rotate in the x-y plane at frequency $\omega_{\rm rot}$. First-order spatial gradients in $\mathcal{B}_{\rm rot}$ are not important, because ion secular motion in the trap will average away the effects of these gradients leaving only the value of $\mathcal{B}_{\rm rot}$ at the

center of the trap. Second-order spatial gradients on the other hand will lead to nonzero average frequency shifts whose value will vary from ion to ion in a thermal sample of ions, depending on conserved quantities of individual ion motion like the axial secular energy E_z or radial secular energy E_r, quantities with thermally averaged values of kT_z and kT_r, respectively, and with ion-to-ion variation comparable to their mean values. The $\mathcal{B}_{\rm rot}$ might be generated by current-carrying rods which are of necessity within the vacuum chamber because of the screening effects of a metal vacuum chamber. Unless particular care is taken in the design of these rods, the second-order spatial gradients in $\mathcal{B}_{\rm rot}$ will scale as $1/X^2$, where X is the characteristic size (and spacing) of the current carrying rods. The contribution to the inhomogeneity of the time-averaged value of $\mathcal{B}_{\rm rot}$ experienced by a thermal sample of ions orbiting in a cloud with r.m.s size r is then of order $(r^2/X^2)\mathcal{B}_{\rm rot}$, leading to an ion-to-ion frequency variability of order $(r^2/X^2)3g_F\mu_B\mathcal{B}_{\rm rot}$ For planned parameters of the experiment, (r^2/X^2) is of order 0.01. We've seen from Chapter 6.5 above that the quantity $3g_F\mu_B\mathcal{B}_{\rm rot}$ must be at least about five times larger than Δ in order to make the eigenstates in the rotating fields be states of good m_F. Thus in the absence of explicit apparatus design to null the second-order spatial gradient in $\mathcal{B}_{\rm rot}$ (The rod-like electrodes that bear the charge that generates $\mathcal{E}_{\rm rot}$ are in the second-generation trap the same objects that carry the current that generates $\mathcal{B}_{\rm rot}$ and thus their shape is already subject to multiple design constraints) we may have to live with a decoherence rate from this effect on the order of 0.05Δ, perhaps 0.5 s^{-1}, for the experimental values given in Appendix A.

The inhomogeneity in $\mathcal{B}_{\rm rot}$ should reverse quite cleanly with the $\mathcal{B}$-chop, and residual imperfections there will be cleaned up with the four-way-chop, and thus the effects of the second-order gradients in $\mathcal{B}_{\rm rot}$ are expected to be predominantly a source of decoherence, rather than systematic error on measured d_e.

6.12 Stray Contributions to $\mathcal{B}_{||}$: Static $\mathcal{B}$-Field Gradients

We now return to discussing static magnetic fields, now including the effects of spatial gradients. With the characteristic size of the ion cloud r being smaller than the characteristic distance X

from cloud center to source of magnetic field by a ratio of 0.1 or smaller, it makes sense to expand the field about the uniform value at the trap center. The most general first-order correction to a static magnetic field in the absence of local sources can be characterized by five linearly independent components as follows:

$$\begin{aligned}\vec{\mathcal{B}} &= \mathcal{B}'_{\rm axgrad}(z\hat{z} - \frac{x}{2}\hat{x} - \frac{y}{2}\hat{y}) \\ &\quad +\mathcal{B}'_{\rm trans}(x\hat{x} - y\hat{y}) \\ &\quad +\mathcal{B}'_1(y\hat{x} + x\hat{y}) \\ &\quad +\mathcal{B}'_2(z\hat{x} + x\hat{z}) \\ &\quad +\mathcal{B}'_3(y\hat{z} + z\hat{y}) \end{aligned} \tag{6.67}$$

By far the most important effect of these terms is the "micromotion-axial gradient interaction." As discussed in Chapter 3.9, the displacement of an ion's circular micromotion $\vec{r}_{\rm rot}$ is exactly out of phase with the rotation of its quantization axis $\hat{\mathcal{E}}$, see Eq. 3.30 . Averaged over a cycle of $\omega_{\rm rot}$, this will give rise to a nonzero average contribution to $\mathcal{B}_{||}$ and cause a shift in $W^{u/\ell}$ given by $3g_F\mu_B\mathcal{B}'_{\rm axgrad}r_{\rm rot} = 3g_F\mu_B\mathcal{B}'_{\rm axgrad}e\mathcal{E}_{\rm rot}/(M\omega^2_{\rm rot})$. A guess for a possible value of stray $\mathcal{B}'_{\rm axgrad}$ is 2 mG/cm, which for anticipated experimental parameters would lead to a shift in $W^{u/\ell}$ of order 4 Hz, and this shift would survive the $\mathcal{B}$-chop. As with the effect of displacement currents, one expects the systematic effect of the shift to be reduced after the four-way chop by $(\delta g_F/g_F)$, but for maximum accuracy the effect should be shimmed out of the $\mathcal{B}$-field chop, either by adjusting the value of $\mathcal{B}^{\rm shim}_{\rm rot}$, or by applying (say with anti-Helmholtz coils external to the vacuum chamber) a compensating value of $\mathcal{B}'_{\rm axgrad}$.

A smaller effect arises from the interaction of the magnetic field gradient with the component of the electric fields responsible for providing ion confinement, which after averaging over cycles of $\omega_{\rm rot}$ and $\omega_{\rm rf}$, always point inward, giving rise to a net inward-pointing time average of $\hat{\mathcal{E}}$. If we look at only the component of the first-order magnetic field gradient that points towards or away from the trap center

$$\vec{\mathcal{B}}^{\text{central}} = (\mathcal{B}'_{\text{trans}} - \mathcal{B}'_{\text{axgrad}}/2)x\hat{x} + (-\mathcal{B}'_{\text{trans}} - \mathcal{B}'_{\text{axgrad}}/2)y\hat{y} + \mathcal{B}'_{\text{axgrad}}z\hat{z} \tag{6.68}$$

The net contribution to $\mathcal{B}_{||}$ comes from integrating, along the rf and rotation micromotion trajectories, over first a rotational cycle, and then an rf cycle, and then a secular cycle in a given direction. We assume that the trap is sufficiently harmonic that there is no cross-dimensional mixing of secular energy, and that hard-momentum-changing collisions are rare enough so that, during the duration of a spectroscopic measurement, there is no change in E_i, the sum of the kinetic and potential energy associated with an individual ion's secular motion in the ith direction. The contribution to $\mathcal{B}_{||}$ is then,

$$\delta\mathcal{B}_{||} = ((\mathcal{B}'_{\text{trans}}/2 - \mathcal{B}'_{\text{axgrad}}/4)\mathrm{E}_x + (-\mathcal{B}'_{\text{trans}}/2 - B'_{\text{axgrad}}/4)\mathrm{E}_y + \mathcal{B}'_{\text{axgrad}}\mathrm{E}_z)/(e\,\mathcal{E}_{\text{rot}}). \tag{6.69}$$

The contribution to $\mathcal{B}_{||}$ averaged over a thermal sample of ions is given by the above expression with E_i replaced by T_i. Note that for $T_x = T_y = T_z$, several terms cancel and the thermally averaged contribution to $\mathcal{B}_{||}$ is just $\mathcal{B}'_{axgrad}\mathrm{E}_z/(2e\mathcal{E}_{\text{rot}})$. The decohering effect is comparable because within a thermal sample, E_x, E_y, and E_z will in general differ from one another for a given ion, and between different ions. For $\mathcal{B}'_{\text{axgrad}}$ and $\mathcal{B}'_{\text{trans}}$ each about 2 mG/cm, ion temperatures about 15 K, the mean shift in $\mathrm{W}^{\mathrm{u}/\ell}$ for typical experimental parameters given in Appendix A might be 30 mHz, with a comparable contribution to dephasing.

The three remaining terms in the first-order gradient, $\mathcal{B}'_1$, $\mathcal{B}'_2$ and $\mathcal{B}'_3$, will contribute to a shift in $\mathcal{B}_{||}$ only when combined with other (usually small) trap imperfections, for instance the plane of rotation of $\mathcal{E}_{\text{rot}}$ being tilted with respect to principal axes of the confining potential. The net effects will be correspondingly smaller than those from $\mathcal{B}'_{\text{trans}}$.

Just as with the second spatial derivative of $\mathcal{B}_{\text{rot}}$, the spatial derivative of $\mathcal{B}'_{\text{axgrad}}$, coupled to a thermal spread in the size of ion orbits, can give rise to decoherence. Of course, $\mathcal{B}_{\text{axgrad}}$ is defined already as a first spatial derivative of a magnetic field, thus the dephasing arises from a third derivative of the field, and its rate should be down from the mean size of the shift (roughly estimated above at 4 Hz) by a factor of order $(r/X)^2$, or a factor of one hundred. Even spatially

uniform $\mathcal{B}'_{\text{axgrad}}$ could give rise to decoherence if there is a spatial dependence in r_{rot}. The fractional change in r_{rot} is the same as the fractional change in $\mathcal{E}_{\text{rot}}$. As discussed in Chapter 3.9, this should be smaller than 0.5% over the typical size of the ion sample.

To sum up Chapter 6.11 and 6.12, we have looked at a range of ways in which various contributions to $\mathcal{B}_{||}$ can shift W^u and W^ℓ. Decoherence due to shot-to-shot fluctuations or spatial inhomogeneity should not be a problem out to beyond 1 s coherence times. Various effects can shift W^u and W^ℓ by as much as a few Hz, and this shift can survive a $\mathcal{B}$-chop. With $\delta g_F/g_F$ on order of 10^{-4}, and $\mathcal{E}_{\text{eff}}$ estimated at 90 GV/cm in ThF^+, after a four-way chop the remaining systematic error will be a few 10^{-29} e cm, but this can be dramatically reduced by tuning away the post-$\mathcal{B}$-chop signal with $\mathcal{B}^{\text{shim}}$. The most dangerous systematic error would be if $\mathcal{B}_{\text{rot}}$ were systematically different between measurements on the upper and on the lower states. Chopping between upper and lower states will be determined by variations in optical pumping, which should be well decoupled from the mechanisms that generate $\mathcal{B}_{\text{rot}}$.

6.13 Alternative Application of $\mathcal{B}_{\text{rot}}$

It is worth considering that applying a very spatially uniform $\mathcal{B}_{\text{rot}}$ may be very challenging because of difficult-to-model eddy currents induced in electrodes and light-gathering mirrors. On the other hand a purposely applied static $\mathcal{B}'_{\text{axgrad}}$ would be perturbed only by the magnetic permeability of trap construction materials, which can be minimized and modeled. One way or another we will need to bias away from the avoided crossing discussed in Chapter 6.4, but it may turn out that this can be accomplished with a lower total decoherence rate by omitting the applied $\mathcal{B}_{\text{rot}}$ altogether, and providing the bias with a deliberately applied $\mathcal{B}'_{\text{axgrad}}$ field. The $\mathcal{B}$-field chop could be accomplished by chopping the sign of $\mathcal{B}'_{\text{axgrad}}$. The parity invariance argument of Chapter 6.4 can readily be modified to describe a chop of $\mathcal{B}'_{\text{axgrad}}$ rather than a chop in $\mathcal{B}_{\text{rot}}$.

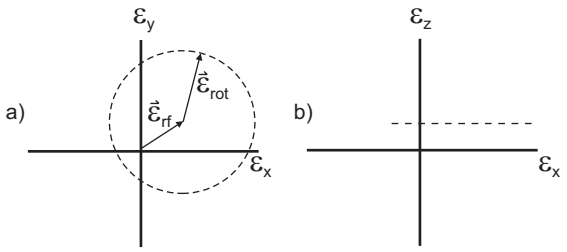

Figure 6.5: Over one rotation of $\mathcal{E}_{\rm rot}$, both $\mathcal{E}_{\rm rf}$ and $\mathcal{E}_z$ are quasistatic. The total electric field is the sum of all three and its trajectory over one cycle of $\mathcal{E}_{\rm rot}$ is plotted as the dotted line projected onto (a) the x-y and (b) the x-z planes. The electric field trajectory is a circle of radius $\mathcal{E}_{\rm rot}$, parallel to and displaced from x-y plane, a circle whose center is offset from the z-axis by $\mathcal{E}_{\rm rf}$. In the limit $\mid \mathcal{E}_{\rm rf} \mid \ll \mid \mathcal{E}_{\rm rot} \mid$, the solid angle subtended from the origin by this circle differs only slighlty from that subtended by a circle with vanishing $\mathcal{E}_{\rm rf}$. The magnitudes of both $\mathcal{E}_{\rm rf}$ and $\mathcal{E}_z$ relative to $\mathcal{E}_{\rm rot}$ are very much exaggerated for clarity.

6.14 Relativistic (Ion-Motion-Induced) Fields

The largest component of the velocity on the ions is that of the micromotion induced by $\mathcal{E}_{\rm rot}$; for reasonable experimental parameters it will be less than 1000 m/s. In typical lab-frame magnetic fields of a few mG, the motion will give rise, through relativistic transformation, to electric fields of order of a few μV/cm, which are irrelevant to our measurement. Conversely, motion at 1000 m/s in typical lab-frame electric fields of 10 V/cm generates a magnetic field of 0.1 μG. This field will be rigorously perpendicular to the electric field, the quantization axis, and thus represents only a negligible modification to the generally unimportant $\mathcal{B}_\perp$.

6.15 Effect of RF Fields

The effects of the rf electric fields providing Paul trap confinement are best understood by putting them in the context of a three-tier hierarchy of electric field magnitudes and frequencies.

(i) $\mathcal{E}_{\rm rot}$, the nominally uniform, rotating electric field, with field magnitude of perhaps 10 V/cm and frequency $\omega_{\rm rot} = 2\pi\times$100 kHz.

(ii) $\mathcal{E}_{\rm rf}$, the Paul-trap fields, are highly inhomogeneous, but at a typical displacement in the x-y plane of perhaps 0.5 cm, the field strength might be 75 mV/cm, or two orders of magnitude less than that of $\mathcal{E}_{\rm rot}$, oscillating at a frequency, $\omega_{\rm rf} = 2\pi\times$15 kHz which is one order of magnitude less

than $\omega_{\rm rot}$. At a fixed point in space, the rf fields average rigorously to zero over time, but averaged instead along an ion's rf micromotion trajectory, the rf fields contribute to

(iii) the inward-pointing trapping electric field, again very inhomogeneous but with typical strength down from peak rf-field values by factor of $(\omega_{\rm rf}/\omega_i)$, another order of magnitude, to perhaps 5 mV/cm. From the ion's perspective, the direction of the trapping fields oscillate with the ion's secular motions in the trap, at frequencies ω_i of perhaps $2\pi\times1$ kHz, the slowest time scale by an order of magnitude.

The effects of the strong, fast $\mathcal{E}_{\rm rot}$ have been discussed extensively throughout Chapter 6, and those of the weak, slow trapping fields were covered in Chapter 6.12. In this subsection we argue that the rf electric fields, intermediate in both frequency and strength, are the least significant of the three categories.

The effects of the rf fields averaged over the rf micromotion trajectory are discussed in Chapter 6.12. The remaining part averages to zero in one rf cycle, but is roughly frozen at a single value over the duration of one cycle of $\omega_{\rm rot}$. The dominant source of the rf fields' time-averaged contribution to transitions $\mathrm{W}^{u/l}$ is in very small corrections to Berry's phase energy associated with the rotation of $\mathcal{E}_{\rm rot}$. See Fig. 6.5. The correction to the solid angle arising from $\mathrm{E_{rf}}$ goes as $(\mathrm{E}_z/\mathrm{E_{rot}})(\mathrm{E_{rf}}/\mathrm{E_{rot}})^2$. If we include a factor of $\omega_{\rm rot}$ to get a Berry's energy shift and evaluate for typical experimental parameters, the magnitude of the resulting frequency shift will be about 20 mHz, and will oscillate in sign with the axial secular motion. The magnitude of radial rf fields scales linearly with the radial secular displacement. If secular freqencies were commensurate, in particular if $\omega_z = 2\omega_r$, then this 20 mHz shift could contribute to a decoherence rate at the negligible level of a few tens of mHz. For incommensurate ratios of ω_z/ω_x or ω_z/ω_y, the rf fields will be still less important.

6.16 Systematic Errors Associated with Trap Asymmetries

The symmetry argument of Chapter 6.4 was based on parity invariance. This argument is only as good as reflection symmetry of the electric and magnetic fields in the region of the trapped

ions. In this section we look, as an example, at the consequences of a symmetry imperfection.

The electrodes used to generate $\mathcal{E}_{\rm rot}$ have been numerically designed to make $\mathcal{E}_{\rm rot}$ as spatially uniform as possible, but imperfections in design and construction of the trap and imperfect drive electronics will lead to some residual field nonuniformity. Suppose that the magnitude of the $\mathcal{E}_{\rm rot}$ was consistently larger in the region of the trap for which z>0, so that the value of $\mathcal{E}_{\rm rot}$ over the z>0 half of an axial secular oscillation is about 0.3% larger than that experienced over the z<0 half. Thus the frequency modulation of perhaps $\pm$ 500 Hz, discussed in Chapter 6.5 will no longer average to precisely zero over an axial cycle but instead a net contribution of about 1.5 Hz to W^u. Such a frequency shift would survive a $\mathcal{B}$-field chop, and, following the protocol discussed in section IV.F, we could very likely incorrectly identify this shift as arising from the presence of a $B_{\rm rot}^{\rm stray}$, and apply a value of $B^{\rm shim}$ to largely null the 1.5 Hz shift. After a complete four-way chop, we would be left with a systematic error on the order of $(\delta g_F/g_F)\times$1.5 Hz, or about 0.4 mHz.

For the value of $\mathcal{E}_{\rm eff}$ estimated for HfF^+, a 0.4 mHz error corresponds to a systematic error on d_e of the order of a few 10^{-29} e cm. For ThF^+, the error on d_e would be about three times smaller. We continue a more general discussion on systematic errors in Chapter 8.2.

Chapter 7

Other Sources of Decoherence, Collisions and Black-Body Radiation [1]

7.1 Ion-Ion Collisions

The overarching strategy of the trapped-ion approach to precision spectroscopy is to accept low count rates in exchange for very long coherence times. In some previous precision measurement experiments with trapped ions, the very best results have come from taking this to the extreme limit of working with only one ion [120, 121, 122, 123, 124, 125, 126, 127], or in some cases a pair of ions [128], in the trap at any given time. More often however, optimal precision is achieved working with a small cloud of trapped ions. In this section various detrimental effects of ion-ion interactions are evaluated.

7.1.1 Mean-Field

With no electrons present to neutralize overall charge, even a relatively low density cloud of ions can have a significant mean-field potential. A spherically symmetric sample of N_{ion} ions confined within a sphere of radius r will give rise to a mean-field potential

$$\frac{U_{\text{mean-field}}}{k_B} \approx 3 \text{ K} \times \left(\frac{N_{\text{ion}}}{1000}\right) \left(\frac{r}{0.5 \text{ cm}}\right)^{-1}. \tag{7.1}$$

At values of the mean-field interaction energy comparable to or larger than $k_B T$, there is a risk of instabilities, viscous heating, and other undesirable effects; even in their absence, systematic errors are more difficult to analyze in the strong mean-field limit. Ion-trap experiments have been performed at much higher mean-field strengths, and indeed there have been precision spectroscopy

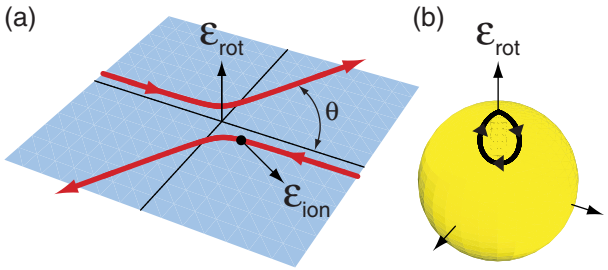

Figure 7.1: Geometric phases accumulated during an ion-ion collision. (a) A typical ion-ion collision trajectory (red), resultant Rutherford scattering angle, θ, and ion-ion interaction electric field, $\mathcal{E}_{\text{ion}}$, are shown in the collision plane (blue). For clarity, the collision plane has been taken perpendicular to the instantaneous direction of $\mathcal{E}_{\text{rot}}$. (b) During an ion-ion collision the molecular axis adiabatically follows the net electric field vector, $\vec{\mathcal{E}}_{\text{rot}} + \vec{\mathcal{E}}_{\text{ion}}$, and traces out the contour (black) on the unit sphere (yellow). The solid angle, $\Delta\mathcal{A}(\theta)$, subtended by this contour gives rise to a geometric phase accumulated by the eigenstates during the collision. This leads to decoherence of the spectroscopic transition, see text.

experiments done in systems for which the interaction potential even between an individual pair of nearest-neighbor ions is much larger than $k_B T$. However, these systems exhibit a high degree of spontaneous symmetry breaking including crystallization [129].

Throughout this thesis it is assumed the experiments will be done in the low mean-field limit, say

$$U_{\text{mean-field}} \lesssim \frac{1}{3} k_B T. \tag{7.2}$$

In this limit, mean-field effects are relatively benign, and can be modeled as a modest decrease in the trap confining frequencies, ω_i, plus the addition of some anharmonic terms to the potential. Crucially for the arguments presented in Chapter 6.4, these additional modifications do not break any of the reflection- or rotation-based symmetries of the trapping fields. Eqns. 7.1 and 7.2 combine to set limits on various combinations of the ion number, N_{ion}, ion temperature, T, cloud radii, $r_i \propto \sqrt{\frac{k_B T}{M\omega_i^2}}$, and mean ion density, $n \propto \frac{N_{\text{ion}}}{r_x r_y r_z}$. This necessitates making various compromises in selecting operating parameters.

In Chapter 6.5, the axial component of the electric field at the ion's location, $\mathcal{E}_z$, was shown to tilt the rotating electric field and give rise to an apparent shift of the energy of our spectroscopic transition, linear in $\mathcal{E}_z$. This energy shift integrated over time in turn gives rise to an oscillatory

phase shift, $\Delta\phi = \frac{\omega_{\rm rot}}{\mathcal{E}_{\rm rot}} \int \mathcal{E}_z dt$. In a one-component ion cloud, the effects of long-range, grazing-angle ion-ion collisions may be thought of as simply a fluctuating component to the local electric field, and the integrated effect of those fluctuations will make a random contribution to the phase shift. We present a simple argument to show that the resulting rms spread in phase does not continue to increase with time but reaches a steady-state asymptote. This is because $\mathcal{E}_z$ not only shifts the transition energy, it also causes an axial force and corresponding acceleration, which, like the shift in transition energy, is linear in $\mathcal{E}_z$. Integrated over time, $\Delta p_z = e \int \mathcal{E}_z dt$, this fluctuating force results in a fluctuating momentum. But we know that the combined effect of a trapping field and a large number of random collisions will not cause the rms momentum to randomly walk without bound but rather to be loosely bounded by a characteristic thermal value, $\sqrt{\langle p_z^2 \rangle} \approx \sqrt{M k_B T_z}$. This is the nature of the thermal equilibration process – once an ion has developed a super-thermal momentum, further collisions are biased to reduce the momentum. Since both the phase excursion and the momentum excursion are linear in the time-integrated axial electric field, we can estimate $\sqrt{\langle \Delta\phi^2 \rangle} \approx \frac{\omega_{\rm rot}}{\mathcal{E}_{\rm rot}} \sqrt{\langle p_z^2 \rangle} \approx \sqrt{\frac{k_B T_z}{2 {\rm E}_{\rm rot}}}$. Again, as discussed in Chapter 6.5, if ${\rm E}_{\rm rot} >\sim 30 k_B T_z$, the phase fluctuations for each ion's spectroscopic transition will be bounded by a value less than one radian, so that there will be no loss in spectroscopic contrast in a Ramsey-type experiment.

The argument in the paragraph above hinges on the assumption that the electric field arising from the ion cloud's mean-field distribution and from grazing-angle collisions is small in magnitude compared to $\mathcal{E}_{\rm rot}$, so that the shift in Berry energy is linear in the axial component of the electric field. For higher values of the ion temperature or lower values of $\mathcal{E}_{\rm rot}$, a pair of colliding ions can get so close to each other that the electric field is, transiently, comparable to or larger than $\mathcal{E}_{\rm rot}$. The consequences are discussed in the next subsection.

7.1.2 Geometric Phases Accumulated During an Ion-Ion Collision

As discussed in Chapter 6.4, when a spin adiabatically follows a time-varying quantization axis it acquires a geometric (Berry's) phase. For the eigenstates in Fig. 2.1(b), the geometric phase factor can be written as $\exp(\pm i m_F \mathcal{A})$, where $\mathcal{A}$ is the solid angle subtended by the contour on the

unit sphere traced out by the time-varying quantization axis. Thus, the relative phase generated between the $|F = 3/2, m_F = \pm 3/2\rangle$ states used for spectroscopy is $\phi = 3\mathcal{A}$. The concern of this subsection is how ion-ion collisions cause uncontrolled excursions of the quantization axis leading to random geometric phase shifts and decoherence between spin states. These uncontrolled phase shifts will be written as $\Delta\phi = 3\Delta\mathcal{A}$ to distinguish them from the calibrated geometric phases in the experiment.

The instantaneous quantization axis for the molecular ion eigensates is defined by the net electric field vector at the location of the ion. During a collision, this axis is defined by the vector sum of the rotating electric field, $\vec{\mathcal{E}}_{\text{rot}}$, and the ion-ion interaction electric field, $\vec{\mathcal{E}}_{\text{ion}}$. Both of these are time-varying vectors, however typical ion-ion collisions have a duration short compared to the rotation period of $\mathcal{E}_{\text{rot}}$ so for the purpose of this discussion $\mathcal{E}_{\text{rot}}$ will be taken as stationary. Thus, the problem is reduced to calculating the excursion of the quantization axis under the time variation of $\mathcal{E}_{\text{ion}}$. A typical ion-ion collision is shown in Fig. 7.1(a) and the effect of this collision on the quantization axis is shown in Fig. 7.1(b).

At the temperatures of our trapped ion samples, no two ions are ever close enough for the details of the intermolecular potential to matter. Only monopole-monopole and monopole-dipole interactions matter. Further, the translational degree of freedom may be treated as purely classical motion in a $1/r$ ion-ion potential, with the initial condition of a given collisional event characterized by an impact parameter and relative velocity. The outcome of the collision depends not only on the magnitudes of the impact parameter and of the velocity, but also on their angles with respect to the ambient electric bias field, $\mathcal{E}_{\text{rot}}$. Each initial condition contributes a particular amount to the variance in the phase between the relevant internal states. These contributions can be converted to partial contributions to a decoherence rate, and a numerical integral over a thermal distribution of collisional initial conditions can yield the total decoherence rate. We've pursued this program to a greater or lesser extent with the decoherence mechanisms discussed in this subsection and the one immediately following, but the results are not especially illuminating and we've used them primarily to confirm that the power-law expressions discussed below represent only overestimates

of the decoherence rate, and that for experimental parameters of interest, the decoherence rate will be conservatively less than 1 s^{-1}.

The main question is whether T is high enough to include significant phase space for collision trajectories for which the peak value of $\mathcal{E}_{\rm ion} > \mathcal{E}_{\rm rot}$ (which is to say, large enough to transiently tip the direction of the total field by more than a radian). If so, then a single collision can cause decoherence and one can get a simple estimate of the cross-section for decoherence simply from the size of the impact parameter that leads to those events. There is a significant probability for collisions with $\mathcal{E}_{\rm ion} >\sim \mathcal{E}_{\rm rot}$ when

$$T \gg 18\ K \left(\frac{\mathcal{E}_{\rm rot}}{5\ {\rm V/cm}}\right)^{1/2}, \tag{7.3}$$

which leads to a decoherence rate

$$\tau^{-1} \approx 0.47 \times \left(\frac{n}{1000\ {\rm cm}^{-3}}\right)\left(\frac{T}{15\ {\rm K}}\right)^{1/2}\left(\frac{\mathcal{E}_{\rm rot}}{5\ {\rm V/cm}}\right)^{-1}\ {\rm s}^{-1}. \tag{7.4}$$

If T is instead so low that the Coulomb barrier suppresses collisions that could lead to a sufficiently large value of $\mathcal{A}$ and cause decoherenc with a single collision, then decoherence will arise only from the combined effects of many collisions each causing small phase shifts that eventually random walk the science transition into decoherence. In this regime, the decoherence rate falls off very fast at low temperatures. For

$$T \ll 18\ K \left(\frac{\mathcal{E}_{\rm rot}}{5\ {\rm V/cm}}\right)^{1/2}, \tag{7.5}$$

typical collisions have $\mathcal{E}_{\rm ion} <\sim \mathcal{E}_{\rm rot}$ and the decoherence rate is

$$\tau^{-1} \approx 0.13 \times \left(\frac{n}{1000\ {\rm cm}^{-3}}\right)\left(\frac{T}{15\ {\rm K}}\right)^{13/2}\left(\frac{\mathcal{E}_{\rm rot}}{5\ {\rm V/cm}}\right)^{-4}\ {\rm s}^{-1}. \tag{7.6}$$

Both Eqns. 7.4 and 7.6 represent conservative estimates of the decoherence rate, and for an intermediate range of temperature, the decoherence rate will be less than whichever estimate gives the smaller value (Fig. 7.2).

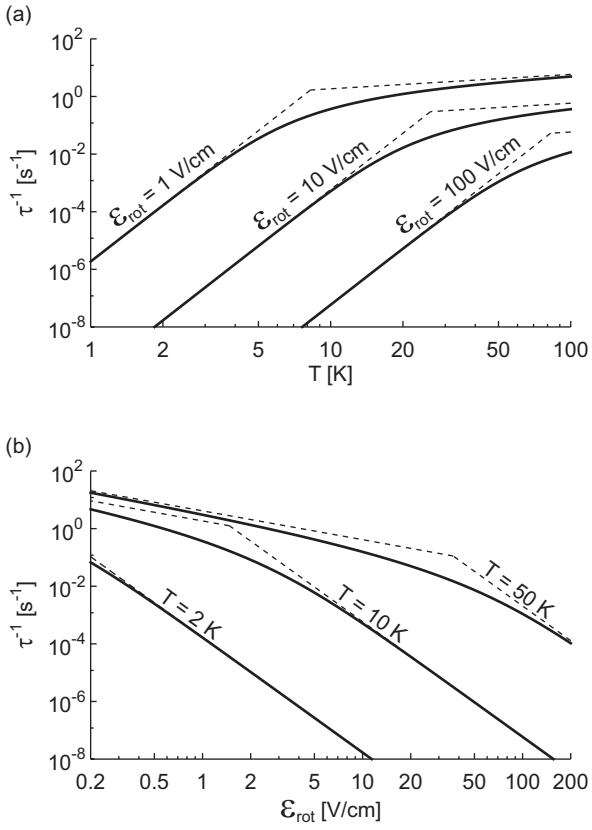

Figure 7.2: Inverse coherence times, τ^{-1}, due to geometric phases accumulated during ion-ion collisions as a function of (a) collision energy in temperature units and (b) $\mathcal{E}_{\rm rot}$. Dotted lines are approximations given in Eqns. 7.4 and 7.6. Solid lines are more involved estimates based on integrals over collision parameters, but are still based on approximations so as to be conservative. The ion density was taken to be $n = 1000$ cm^{-3}.

7.1.3 m-Level Changing Collisions

A second source of decoherence can arise from ion-ion collisions that induce transitions between internal levels of a molecule. The dominant inelastic channel will be transitions between m_F levels induced by a sufficiently sudden tilt in the quantization axis defined by the instantaneous local electric field. There are two conditions for such a transition to occur: (i) the direction of the total field must change by nearly a radian or more, so that there is significant amplitude for, e.g., an $m_F = +3/2$ level in the unperturbed electric field to suddenly have non-negligible projection on an $m_F = +1/2$ level in the collision-perturbed field, and (ii) the time rate of change of the electric field direction must be comparable to or larger than the energy splitting between an $m_F = 3/2$ level and its nearest $m_F = 1/2$ level in the field $\mathcal{E}_{\rm rot}$.

Note that the first requirement is the same as the requirement for picking up an appreciable single collision Berry's phase. However, not all collisions that satisfy the first requirement will satisfy the second requirement. In particular, if the relative velocity in a collision is too low, then the time rate of change of the electric field direction will be too slow to satisfy the second requirement. Thus, given that the first requirement is satisfied, then the second requirement will *not* be satisfied when

$$T < 5\ \mathrm{K} \times \frac{\mathcal{E}_{\rm rot}}{5\ \mathrm{V/cm}}, \tag{7.7}$$

In this limit, the second requirement is more stringent than the first requirement, which means that the rate of m-level changing collisions will be smaller than the rate of single-collision Berry's phase-induced decoherence. In the opposite limit, we expect the second requirement will be met whenever the first requirement is met, and thus we would expect that the two channels of decoherence, m-level changing and single-collision Berry's phase, will be comparable in magnitude.

Looking at particular collision trajectories in more detail, we see that there are trajectories that can cause an m-level change but for which there is no contribution to Berry's phase because the electric field traces out a trajectory with no solid angle (for instance, if the classical impact parameter $\vec{b}$ is parallel to $\vec{\mathcal{E}}_{\rm rot}$). We also note that our formulation of the requirement of sweep

rate for m-level changing collisions neglects the fact that $\mathcal{E}_{\rm ion}$ will not only change the direction of the total electric field ($\vec{\mathcal{E}}_{\rm ion} + \vec{\mathcal{E}}_{\rm rot}$) but also in general will change its magnitude. For most impact parameters, the magnitude of the total electric field will increase, thus suppressing nonadiabatic effects. However, a narrow range of impact parameters exists where the magnitude of the total electric field decreases, thus enhancing nonadiabatic effects. However, the above scaling laws account for the vast majority of collisions.

In the end, we are less interested in the actual rates than we are in putting conservative limits on decoherence rates. For instance, in calculating the curves in Fig. 7.2, we pessimistically took a worst-case geometry, $\mathcal{E}_{\rm rot} \perp \mathcal{E}_{\rm ion}$, which gives an upper limit on the size of the effect. Thus we estimate that:

- For $T < 5\ {\rm K} \times \frac{\mathcal{E}_{\rm rot}}{5\ {\rm V/cm}}$ the *total* collisional decoherence, including both m-level-changing and Berry's-inducing effects, will be less than or equal to the value given by solid curves in Fig. 7.2, while
- For $T > 5\ {\rm K} \times \frac{\mathcal{E}_{\rm rot}}{5\ {\rm V/cm}}$, the *total* collisional decoherence will be no greater than twice as large as the rate indicated by those curves.

7.2 Ion-Neutral Collisions

Ion-neutral collisions are troubling in our experiment due to their potential to change the internal states of our ions as well as their potential to increase our ion temperatures. The electric field of the ion will polarize a neutral atom or molecule giving rise to the attractive helium-ion interaction potential,

$$V_{\rm int}(r) = -\frac{1}{2}\alpha\mathcal{E}_{\rm ion}^2(r) = -\frac{1}{2}\alpha\left(\frac{e}{4\pi\epsilon_0}\right)^2\frac{1}{r^4}, \tag{7.8}$$

where α is the DC electric polarizability of the neutral particle and $\mathcal{E}_{\rm ion}$ is the electric field of the ion. An effective scattering potential can be defined as the sum of the attractive helium-ion interaction potential and the repulsive "angular momentum barrier" associated with the collision

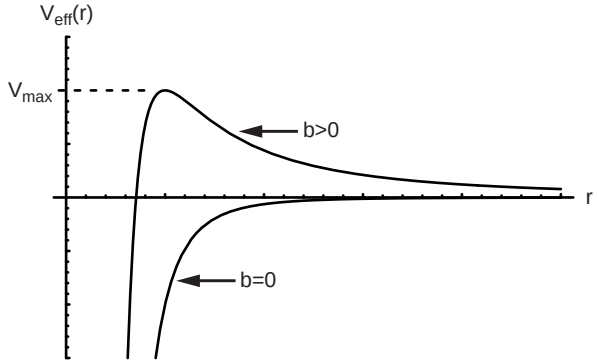

Figure 7.3: The effective helium-ion scattering potential for $b = 0$ and b ¿ 0.

(Fig. 7.3),

$$V_{\text{eff}}(r) = V_{\text{int}}(r) + \frac{L^2}{2mr^2} = -\frac{1}{2}\alpha\left(\frac{e}{4\pi\epsilon_0}\right)^2\frac{1}{r^4} + U_{\text{kin}}\frac{b^2}{r^2}. \tag{7.9}$$

with m the reduced mass of the coliding particles, U_{kin} the kinetic energy of the collision, and L the angular momentum about the center of mass of the colliding particles. The effective neutral-ion scattering potential has a maximum value $V_{\max}(b) = \frac{1}{2}\frac{U_{kin}^2 b^4}{\alpha(e/4\pi\epsilon_0)^2}$. If the kinetic energy of the collision exceeds $V_{\max}$ the particles will approach $r = 0$ until a sharp repulsive potential, due to Fermi repulsion of the electron clouds, is reached. The cross section for these close-range collisions is referred to as the Langevin capture cross section,

$$\sigma_{LC} = \pi b_0^2 = \pi\frac{e}{4\pi\epsilon_0}\sqrt{\frac{2\alpha}{U_{kin}}}. \tag{7.10}$$

The collision rate, $\Gamma_{LC} = n\sigma_{LC}v_{\text{rel}}$, will be independent of temperature since $\sigma_{LC} \propto 1/\sqrt{U_{\text{kin}}}$ while $v_{\text{rel}} \propto \sqrt{U_{\text{kin}}}$.

For argon-ion collisions (using $\alpha_{\text{argon}} = 1.64$ $\mathring{\text{A}}^3$) we obtain,

$$\sigma_{LC}v_{\text{rel}} \approx 4.6 \times 10^{-10} cm^3/s. \tag{7.11}$$

Noble gases have increasing values of α as you move to heavier atoms, with the effects of higher mass and higher α mostly cancelling in the collision rate, therefore our choice of carrier gas is not strongly influenced by this issue. The 1% of SF_6 mixed into our expansion gas will have a similar value of $\sigma_{LC}v_{\text{rel}}$, making it unimportant in this analysis. The cross section for rotation changing

collisions will likely be approximately equal to σ_{LC} [130], giving a limit on our background gas pressure of $\sim 5{\times}10^{-8}$ Torr for a 1 s^{-1} decoherence rate.

Our ultimate limit on background pressure will likely come from another ion-neutral collision issue. The polarized helium atom produces a dipole electric field at the molecular ion given by

$$\vec{\mathcal{E}}_{He}(r) = E_{He}\hat{r} = \frac{1}{4\pi\epsilon_0}\frac{2\alpha}{r^3}\mathcal{E}_{ion}\hat{r} = \frac{2\alpha e}{(4\pi\epsilon_0)^2}\frac{1}{r^5}\hat{r}. \tag{7.12}$$

Large values of $\vec{\mathcal{E}}_{He}$ will lead to Landau-Zener non-adiabatic transitions of our magnetic sub-levels, as the quantization axes is defined by the electric field. A naive estimate involves finding the ion-neutral separation such that $\vec{\mathcal{E}}_{He} = \mathcal{E}_{\text{rot}}$ and assuming this is the critical impact parameter for non-adiabatic transitions. This gives,

$$\sigma_{LZ} \approx \pi\left(\frac{2\alpha e}{(4\pi\epsilon_0)^2}\frac{1}{\mathcal{E}_{\text{rot}}}\right)^{2/5}. \tag{7.13}$$

Increasing $\mathcal{E}_{\text{rot}}$ would seem to mitigate this issue. However, the rotational micro-motion of our ions will begin to dominate v_{rel} as $\mathcal{E}_{\text{rot}}$ is increased. For typical values found in the appendix, the rotational micromotion will have a velocity of ≈ 350 m/s, while the thermal velocity of argon atoms is ≈ 250 m/s at 300 K. The non-adiabatic collision cross section using an argon buffer gas and $\mathcal{E}_{\text{rot}} = 5$ V/cm is ≈ 120 nm^2, limiting our pressure to $\lesssim 1 \times 10^{-9}$ Torr. This is approaching the limit of our turbomolecular pumps and requires significant differential pumping between the source chamber (which will have pressure spikes in the 10^{-4} Torr range when the pulse valve fires) and the ion trapping chamber. The 1/e pumping rate of our vacuum system is on order 10 ms, and some time could be allowed between ion creation and state preparation in order to reduce the differential pumping requirements. If the ions are created in the $^1\Sigma$ state and transferred to the $^3\Delta_1$ state, more wait time could be afforded than if the ions are created directly in the $^3\Delta_1$ level.

7.3 Rotational and Vibrational Excitations from Black-Body Radiation

Our spin coherence time can also be limited by excitations to higher rotational and vibrational states from black-body radiation. The number of photons per mode, $\bar{n}$, in a black-body radiation

field is:

$$\bar{n} = \frac{1}{e^{\frac{h\nu}{kT}} - 1} \tag{7.14}$$

which, in the limit of $h\nu >> kT$ reduces to $\frac{kT}{h\nu}$. The ratio of stimulated to spontaneous emission for a transition is simply $\bar{n}$. The rotational constant for a typical fluoride containing candidate molecule in this experiment is ~ 0.3 cm^{-1}, which gives an ~ 1.2 cm^{-1} splitting between the $J = 1$ and $J = 2$ rotational levels. This means that 300 K black-body radiation will excite the $J = 1$ state to the $J = 2$ state at a rate ≈ 174 times faster than the spontaneous decay rate from $J = 2$ to $J = 1$. Fortunately, radiative decay rates for rotational transitions tend to be quite slow. To estimate this, we take the transition dipole moment,μ_{21}, to equal the molecular frame dipole moment of ≈ 1.2 atomic units [64]. The spontaneous decay time is then given by

$$\tau_{spon} = \frac{3\epsilon_o h c^3}{2\omega_{21}^3 \mu_{21}^2}, \tag{7.15}$$

with ω_{23} being the transition frequency. This gives a spontaneous lifetime of $\approx 1.2\times10^5$ s, and black-body radiation at 300 K should take ≈ 670 s to excite a $^3\Delta_1$ molecule from the $J = 1$ state to $J = 2$.

Given a transition dipole moment, it is interesting to ask at what resonance frequency will black-body radiation have the highest excitation rate. Fig. 7.4 shows a plot of black-body excitation rate versus the dimensionless quantity $h\nu/kT$. We see that the peak rate lies at ≈ 2.82. At 300 K this corresponds to 590 cm^{-1}, which happens to lie near the vibrational transitions of our molecules. For HfF^+ the vibrational constant is ≈ 750 cm^{-1}, with an $\bar{n} \approx 0.028$ for a 300 K black-body. The vibrational decay rate for $v = 2$ to $v = 1$ in the $^3\Delta_1$ state is estimated [64] to be 184 ms. Black-body radiation will therefore limit our coherence time to $\lesssim$ 6 s.

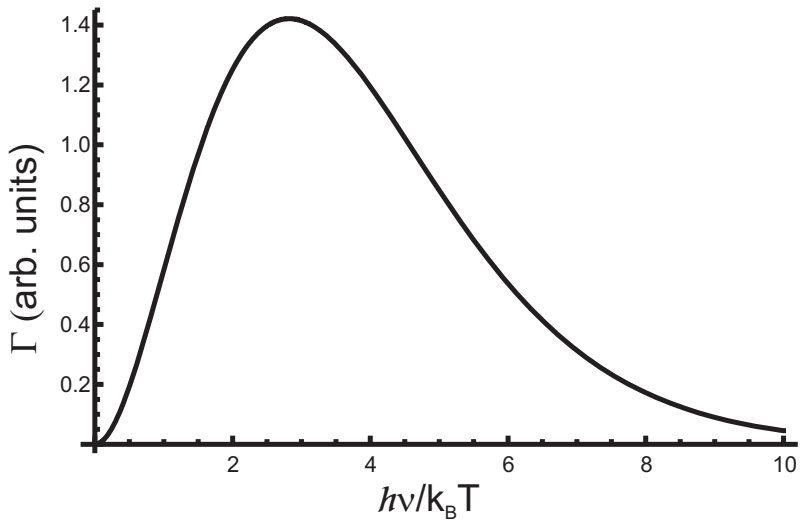

Figure 7.4: Relative black-body excitation rates assuming a constant transition dipole moment versus the dimensionless parameter $\frac{h\nu}{k_B T}$. The peak lies near our vibrational energy spacing for a 300 K black body.

Chapter 8

Conclusions and Sensitivity Estimate [1]

8.1 Precision

Recall from Chapter 1.4 the three components to the sensitivity figure-of-merit: coherence time, $\mathcal{E}_{\text{eff}}$, and count rate. We estimate these three quantities below.

8.1.1 Coherence Time

Conclusions of Chapters 6 and 7: Taking into account only collisional decoherence, and all the questions associated with being in rotating fields and in trapping fields, we would anticipate a coherence time longer than one second. Black-body thermal excitation of the $J = 1$ rotational level will also be well over one second. Vibrational black-body excitation for the $v = 0$ state is estimated at 6 s for HfF^+ in a 300 K environment. Thus the dominant limitation to coherence will likely be the radiative lifetime of the $^3\Delta_1$ state, estimated [64] at 390 ms for HfF^+, and still longer for ThF^+, for which the $^3\Delta_1$ state is predicted to be still lower in energy. Lifetime estimates of the $^3\Delta_1$ level are made difficult by the small transition energy, calculated to be 1600 cm^{-1} in HfF^+ with large relative error, and the uncertain transition dipole moment, due to a large uncertainty in determining the mixture of $^1\Pi$ character into the nominally $^3\Delta_1$ state.

8.1.2 $\mathcal{E}_{\text{eff}}$

$\mathcal{E}_{\text{eff}}$ in HfF^+ is calculated by Meyer and coworkers to be 30 GV/cm [52], and by Titov *et al.* to be 24 GV/cm [54]. For ThF^+, Meyer calculates 90 GV/cm [52]. The uncertainties in these

numbers are hard to assess, but they are very likely accurate to better than a factor of two and, if ongoing spectroscopic studies provide experimental values of hyperfine and fine structure that confirm the ab initio values predicted by the St. Petersburg group, our confidence in the precision of calculated $\mathcal{E}_{\rm eff}$ may be much higher.

8.1.3 Count Rate and Summary of Expected Precision

We are producing HfF^+ ions by photoionization in a relatively narrow range of quantum states, and can estimate yield per quantum level within the desired trapping volume at perhaps 100 ions per shot, but we have just begun to characterize the efficiency of the process and very little optimization has been done. Our efficiency for reading out spin states of trapped ions via laser-induced fluorescence (LIF) is at best 4%, and has not yet been tested. With a large uncertainty, then, we may detect about one ion per shot with four shots per second. Even if we detect as many as four ions in a shot, single shot precision will be no better than 300 mHz, but overall, precision in one hour could be about 10 mHz. For ten hours of data, we anticipate (very roughly) a raw precision at 5×10^{-28} e cm in HfF^+, and 1.5×10^{-28} e cm in ThF^+. We are investigating several alternatives to LIF for spin readout as discussed in Chapter 4.

8.2 Accuracy, Systematic Error

We have not completed a systematic study of the consequences of all possible violations of reflection symmetry in the trapping fields, but work in this direction is ongoing.

For now, we make the following three observations:

i) For the field asymmetries we have analyzed to date, realistic estimates for the magnitude in as-constructed field imperfections lead to systematic errors on the order of a few 10^{-29} e cm or less. While this is not yet as accurate as our ultimate ambitions, it would represent roughly a factor of thirty improvement on the existing best experimental limit.

ii) Asymmetries analyzed to date lead to systematic errors whose signs reverse when the direction of rotation $\omega_{\rm rot}$ reverses. If we combine measurements made with clockwise and coun-

terclockwise field rotation, the errors vanish. Ideally, we'd like to design sufficient accuracy into the experiment so that the chop in field rotation is not needed to achieve desired accuracy, but as a practical matter we will of course run the experiment both ways, averaging the results to get ultimate accuracy, and differencing them to diagnose experimental flaws.

iii) Auxiliary measurements are envisioned to characterize and shim out flaws in the as-constructed trap. For instance, we plan to be able to shim the equilibrium position of the ion cloud up and down along the trap axis, and at each location measure the energy difference E_b-E_d. Unlike E_a-E_b, E_b-E_d is highly electric-field sensitive. The result will be a precise measurement of any spatial gradient in $\mathcal{E}_{\rm rot}$.

iv) All systematic errors we have analyzed to date have strong dependencies on quantities such as $\omega_{\rm rot}$, $\mathcal{B}_{\rm rot}$, $\mathcal{E}_{\rm rot}$, and on the ion-cloud temperature and trap confining frequencies. A true signal from a nonzero value of d_e will be largely independent of all those quantities. We anticipate making a number of auxiliary measurements with the experimental parameters tuned far away from their optimal values to deliberately exaggerate the size of systematic errors and allow us thus to characterize their dependencies in less integration time than that required for ultimate sensitivity. Even so, and as is often the case in precision measurement experiments, sensitivity and accuracy are coupled. To the extent we can measure d_e to high precision at many combinations of experimental parameters, we will better be able to detect and reject false signals.

As an overarching conclusion, the experiment as described here should have the capability to improve the limit on the electron's electric dipole moment to 10^{-29} e cm.

8.3 The Future

Experimentally there are two major ongoing efforts. Sinclair *et al.* are working on measuring excited electronic states of HfF^+ and ThF^+ using novel femto-second comb, cavity enhanced spectroscopy. On the ion trapping side of things, Huanquian is leading the efforts to state-selectively load HfF^+ ions by photoionization and recent progress has been made in measuring the rotational populations of ions produced via photoionization. The construction of the next generation ion trap

is also ongoing. Obviously, I have graciously left much work for my labmates and future generations of students to perform before a measurement of the electron EDM can be made. As Eric might say, it could take weeks of effort after I'm gone to publish a new limit (or value!) on the eEDM. To the younger generations, I say good luck!

Our scientific goal has always been clear, measure the eEDM, while the means to that goal has been the focus of my graduate school efforts. We have been building a highly specialized hammer for a very particular nail. Of course, it has been said that once you have a hammer, every problem looks like a nail. It is therefore tempting to think of possible nails lying around that might suit our particular hammer once we have completed the eEDM work. There has been a proposal [131] that molecules such as HfF^+ could be useful in measuring time variations of fundamental constants. Here near degenerate levels whose energies have very different dependencies on α and m_e/m_p might be found using excited vibrational levels of the $^1\Sigma$ and $^3\Delta_1$ levels. The potential for long interrogation times of our trapped ions could yield sensitive measurements. Molecular ions sympathetically cooled by laser cooled atomic ions have many potential uses as discussed in [132], including studies of cold ion-neutral chemistry. There have also been proposals [133, 134] to use molecules for quantum information processing with the quantum information encoded in the rovibrational eigenstates of the molecule. Such a scheme with trapped molecular ions could have practical advantages over alternative molecular quantum information proposals that involve trapping ultracold neutral molecules and using dipole-dipole interactions for entanglement [135]. Trapped molecular ions, in combination with a superconducting microwave resonator, could also be used in quantum information systems [136].

Bibliography

[1] Material from this chapter will soon appear in print elsewhere in a paper by A.E. Leanhardt, J.L. Bohn, H. Loh, P. Maletinsky, E.R. Meyer, L.C. Sinclair, R.P. Stutz, and E.A. Cornell submitted to PRA.

[2] W. Bernreuther and M. Suzuki. Rev. Mod. Phys., 63:313, 1991.

[3] M.E. Pospelov and I.B. Khriplovich. Sov. J. Nucl. Phys., 53:638, 1991.

[4] E. R. Meyer, J. L. Bohn, and M. P. Deskevich. Phys. Rev. A, 73:062108, 2006.

[5] P.K. Ghosh. Ion Traps. Clarendon Press, 1995.

[6] A. G. Adam, W. S. Hopkins, and D. W. Tokaryk. J. Mol. Spec., 225:1, 2004.

[7] D. Hanneke, S. Fogwell, and G. Gabrielse. Phys. Rev. Lett., 100:120801, 2008.

[8] T. Aoyama, M. Hayakawa, T. Kinoshita, and M. Nio. Phys. Rev. Lett., 99:110406, 2007.

[9] G. W. Bennett *et al.* Phys. Rev. Lett., 92:161802, 2004.

[10] F. Jegerlehner. Nucl. Phys. B-Preceedings Supplements, 181:26, 2008.

[11] J.H. Christenson, J.W. Cronin, V.L. Fitch, and R. Turlay. Phys. Rev. Lett., 13:138, 1964.

[12] B. Aubert *et al.* Phys. Rev. Lett., 87:091801, 2001.

[13] K. Abe *et al.* Phys. Rev. Lett., 87:091802, 2001.

[14] F. Hoogeveen. Nucl. Phys. B, 341:322, 1990.

[15] I.B. Khriplovich and S.K. Lamoreaux. CP Violation Without Strangeness. Springer-Verlag, 1997.

[16] T. Ibrahim and P. Nath. Rev. Mod. Phys., 80:577, 2008.

[17] J.P. Archambault, A. Czarnecki, and M. Pospelov. Phys. Rev. D, 70:073006, 2004.

[18] R.L. Garwin and L.M. Lederman. Nuovo Cim., 11:776, 1959.

[19] L.I. Schiff. Phys. Rev., 132:2194, 1963.

[20] E.M. Purcell and N.F. Ramsey. Phys. Rev., 78:807, 1950.

[21] E. D. Commins, J.D. Jackson, and D. P. DeMille. Am. J. Phys., 75:532, 2007.

[22] B. C. Regan, E. D. Commins, C. J. Schmidt, and D. DeMille. Phys. Rev. Lett., 88:071805, 2002.

[23] E. D. Commins, S. B. Ross, D. DeMille, and B. C. Regan. Phys. Rev. A, 50:2960, 1994.

[24] K. Abdullah, C. Carlberg, E. D. Commins, H. Gould, and S. B. Ross. Phys. Rev. Lett., 65:2347, 1990.

[25] P. G. H. Sandars. Phys. Lett., 14:194, 1965.

[26] P. G. H. Sandars. Phys. Lett., 2:290, 1966.

[27] Energies will be quoted as angular frequencies, in radians/second, or temperatures, in Kelvin, where the factors of $\hbar$ and k_B are omitted from equations, respectively.

[28] Z. W. Liu and H. P. Kelly. Phys. Rev. A, 45:R4210, 1992.

[29] A. C. Hartley, E. Lindroth, and A. M. Martensson-Pendrill. J. Phys. B, 23:3417, 1990.

[30] J.M. Amini, C.T. Munger, and H. Gould. Phys. Rev. A, 75:063416, 2007.

[31] Fang Fang and D.S. Wiess. Opt. Lett., 34:169, 2009.

[32] D. Heinzen (private communication).

[33] S. A. Murthy, D. Krause Jr., Z. L. Li, and L. R. Hunter. Phys. Rev. Lett., 63:965, 1989.

[34] P. G. H. Sandars. Atomic Physics, 4:71, 1975.

[35] J. J. Hudson, B. E. Sauer, M. R. Tarbutt, and E. A. Hinds. Phys. Rev. Lett., 89:023003, 2002.

[36] M. G. Kozlov and V. F. Ezhov. Phys. Rev. A, 49:4502, 1994.

[37] A. V. Titov, N. S. Mosyagin, and V. F. Ezhov. Phys. Rev. Lett., 77:5346, 1996.

[38] M. G. Kozlov. J. Phys. B, 30:L607, 1997.

[39] H. M. Quiney, H. Skaane, and I. P. Grant. J. Phys. B, 31:L85, 1998.

[40] F. A. Parpia. J. Phys. B, 31:1409, 1998.

[41] N. S. Mosyagin, M. G. Kozlov, and A. V. Titov. J. Phys. B, 31:L763, 1998.

[42] D. DeMille *et al.* Phys. Rev. A, 61:052507, 2000.

[43] L. R. Hunter *et al.* Phys. Rev. A, 65:030501, 2002.

[44] D. Kawall, F. Bay, S. Bickman, Y. Jiang, and D. DeMille. Phys. Rev. Lett., 92:133007, 2004.

[45] M. G. Kozlov and D. DeMille. Phys. Rev. Lett., 89:133001, 2002.

[46] T. A. Isaev *et al.* Phys. Rev. A, 69:030501, 2004.

[47] A. N. Petrov, A. V. Titov, T. A. Isaev, N. S. Mosyagin, and D. DeMille. Phys. Rev. A, 72:022505, 2005.

[48] N. E. Shafer-Ray. Phys. Rev. A, 73:034102, 2006.

[49] M. G. Kozlov, V. I. Fomichev, Y. Y. Dmitriev, L. N. Labzovsky, and A. V. Titov. J. Phys. B, 20:4939, 1987.

[50] Y. Y. Dmitriev *et al.* Phys. Lett. A, 167:280, 1992.

[51] A. C. Vutha *et al.* arXiv:0908.2412v1 [physics.atom-ph], 2009.

[52] E. R. Meyer and J. L. Bohn. Phys. Rev. A, 78:010502(R), 2008.

[53] J. Lee, E.R. Meyer, R. Paudel, J.L. Bohn, and A.E. Leanhardt. J. Mod. Opt., 56:2005, 2009.

[54] A. N. Petrov, N. S. Mosyagin, T. A. Isaev, and A. V. Titov. Phys. Rev. A, 76:030501, 2007.

[55] M. R. Tarbutt *et al.* Phys. Rev. Lett., 92:173002, 2004.

[56] S. K. Lamoreaux. Phys. Rev. A, 66:022109, 2002.

[57] B. J. Heidenreich *et al.* Phys. Rev. Lett., 95:253004, 2005.

[58] D. Budker, S.K. Lamoreaux, A.O. Sushkov, and O.P. Sushkov. Phys. Rev. A, 73:022107, 2006.

[59] C.Y. Liu and S.K. Lamoreaux. Mod. Phys. Lett. A, 19:1235, 2004.

[60] B. E. Sauer, H. T. Ashworth, J. J. Hudson, M. R. Tarbutt, and E. A. Hinds. Atomic Physics, 20:44, 2006.

[61] E. R. Meyer and J.L. Bohn (private communication).

[62] This is a good approximation at the 10^{-3} level.

[63] M. V. Berry. Proc. R. Soc. Lond. A, 392:45, 1984.

[64] A. N. Petrov, N. S. Mosyagin, and A. V. Titov. Phys. Rev. A, 79:012505, 2009.

[65] JILA (in preperation).

[66] G. Gräff, E. Klempt, and G. Werth. Z. Phys., 222:201, 1969.

[67] E. Fischer. Z. Phys., 156:1, 1959.

[68] R.F. Wuerker, H.M. Goldenberg, and R.V. Langmuir. J. Appl. Phys., 30:441, 1959.

[69] P.H. Dawson editor. Quadrupole Mass Spectrometry and Its Aplications. American Institute of Physics, 1995.

[70] J.D. Prestage, G.J. Dick, and L. Maleki. J. Appl. Phys., 66:1013, 1989.

[71] L. Spitzer. Physics of Fully Ionized Gases. John Wiley and Sons, 1962.

[72] D.A. Church. Phys. Rev. A, 37:277, 1988.

[73] D. R. Denison. J. Vac. Sci. Technol., 8:266, 1971.

[74] S.R. Jefferts, C. Monroe, E.W. Bell, and D.J. Wineland. Phys. Rev. A, 51:3112, 1995.

[75] A. Drakoudis, M. Söllner, and G. Werth. Int. J. Mass Spec., 252:61, 2006.

[76] M.M. Graff and J.T. Moseley. Chem. Phys. Lett., 105:163, 1984.

[77] C.J. Williams and K.F. Freed. J. Chem. Phys., 85:2699, 1986.

[78] U. Hechtficher *et al.* Phys. Rev. Lett., 80:2809, 1998.

[79] U. Hechtficher *et al.* J. Chem. Phys., 117:8754, 2002.

[80] G. Barinovs and M.C. van Hemert. Chem. Phys. Lett., 399:406, 2004.

[81] F. Bouakline, Andric L. Grozdanov, T.P., and R. McCarroll. J. Chem. Phys., 122:044108, 2005.

[82] G. Herzberg. Molecular Spectra and Molecular Structure, I. Spectra of Diatomic Molecules. Krieger Publishing Company, 1950.

[83] R. Fulton, A.I. Bishop, M.N. Shneider, and P.F. Barker. Nature Phys., 2:465, 2006.

[84] H.J. Metcalf and P. van der Straten. Laser Cooling and Trapping. Springer-Verlag, 1999.

[85] J.M. Doyle, B. Friedrich, Kim J., and D. Patterson. Phys. Rev. A, 52:R2515, 1995.

[86] H. Schaaf, U. Schmeling, and G. Werth. Appl. Phys., 25:249, 1981.

[87] R.B. Blakestad *et al.* Phys. Rev. Lett., 102:153002, 2009.

[88] J.G.E. Harris *et al.* Europhys. Lett., 67:198, 2004.

[89] I.S. Vogelius, L.B. Madsen, and M. Drewsen. Phys. Rev. A, 70:053412, 2004.

[90] I.S. Vogelius, L.B. Madsen, and M. Drewsen. J. Phys. B, 37:4571, 2004.

[91] G. Morigi, P. Pinkse, M. Kowalewski, and R. de Vivie-Riedle. Phys. Rev. Lett., 99:073001, 2007.

[92] B.L. Lev *et al.* Phys. Rev. A, 77:023402, 2008.

[93] E.S. Shuman, J.F. Barry, D.R. Glenn, and D. DeMille. Phys. Rev. Lett., 103:223001, 2009.

[94] K. Molhove and M. Drewson. Phys. Rev. A, 62:011401, 2000.

[95] L. Hornakaer, N. Kjargaard, A. Thommesen, and M. Drewsen. Phys. Rev. Lett., 86:1994, 2001.

[96] A. Bertelsen, S. Jorgensen, and M. Drewsen. J. Phys. B, 39:L83, 2006.

[97] E.R. Hudson. Phys. Rev. A, 79:032716, 2009.

[98] G. Scoles editor. Atomic and Molecular Beam Methods. Oxford University Press, 1988.

[99] E. R. Hudson, Ph.D. thesis, JILA, 2006.

[100] J. Ye and H. Lewandowski groups (private communications).

[101] N.V. Barkovskii, V.I. Tsivel'nikov, A.M. Emel'yanov, and Yu. S. Khodeev. High Temperature, 29:371, 1991.

[102] A. Kuhn *et al.* J. Chem. Phys., 96:4215, 1992.

[103] E.W. Schlag. ZEKE Spectroscopy. Cambridge University Press, 1998.

[104] C.E.H. Dessent and K. Mueller-Dethlefs. Chem. Rev., 100:3999, 2000.

[105] R.W. Field (private communication).

[106] W.C. Wiley and I.H. McLaren. Rev. Sci. Instr., 26:1150, 1955.

[107] H. Loock, B. Simard, S. Wallin, and C. Linton. J. Chem. Phys., 109:8980, 1998.

[108] H. Lefebvre-Brion and R.W. Field. The Spectra and Dynamics of Diatomic Molecules. Elsevier Academic Press, 2004.

[109] J.M. Brown and A. Carrington. Rotational Spectroscopy of Diatomic Molecules. Cambridge University Press, 2003.

[110] J.M. Brown, A.S.-C. Cheung, and A.J. Merer. J. Mol. Spec., 124:464, 1987.

[111] T.C. Steimle, D.F. Nachman, J.E. Shirley, D.A. Fletcher, and J.M. Brown. Mol. Phys., 69:923, 1990.

[112] T. Nelis, S.P. Beaton, K.M. Evenson, and J.M. Brown. J. Mol. Spec., 148:462, 1991.

[113] E. R. Meyer, Ph.D. thesis, JILA, 2010.

[114] R.G. Sachs. The Physics of Time Reversal. Chicago Press, 1987.

[115] J.M. Pendlebury *et al.* Phys. Rev. A, 70:032102, 2004.

[116] M. Rupasinghe and N.E. Shafer-Ray. Phys. Rev. A, 78:033427, 2008.

[117] E. R. Meyer, A.E. Leanhardt, E.A. Cornell, and J. L. Bohn. Phys. Rev. A, 80:062110, 2009.

[118] C.T. Munger. Phys. Rev. A, 72:12506, 2005.

[119] C. Henkel, S. Potting, and M. Wilkens. Appl. Phys. B, 69:379, 1999.

[120] C. Champenois *et al.* Phys. Lett. A, 331:298, 2004.

[121] K. Matsubara *et al.* Appl. Phys. Express, 1:067011, 2008.

[122] M. Chwalla *et al.* Phys. Rev. Lett., 102:023002, 2009.

[123] H.S. Margolis *et al.* Science, 306:1355, 2004.

[124] P. Dube *et al.* Phys. Rev. Lett., 95:033001, 2005.

[125] C. Tamm *et al.* IEEE Trans. Instrum. Meas., 56:601, 2007.

[126] K. Hosaka *et al.* IEEE Trans. Instrum. Meas., 54:759, 2005.

[127] W.H. Oskay *et al.* Phys. Rev. Lett., 97:020801, 2006.

[128] C.W. Chou, D.B. Hume, J.C.J. Koelemeij, D.J. Wineland, and T. Rosenband. Phys. Rev. Lett., 104:070802, 2010.

[129] J.N. Tan, J.J. Bollinger, B. Jelenkovic, and D.J. Wineland. Phys. Rev. Lett., 75:4198, 1995.

[130] G. Buffa, L. Dore, and M. Meuwly. Mon. Not. R. Astron. Soc., 397:1909, 2009.

[131] V.V. Flambaum and M.G. Kozlov. Phys. Rev. Lett., 99:150801, 2007.

[132] S. Willitsch, M.T. Bell, A.D. Gingell, and T.P. Softley. Phys. Chem. Chem. Phys., 10:7200, 2008.

[133] J. Vala, Z. Amitay, B. Zhang, S.R. Leone, and R. Kosloff. J. Mol. Spec., 66:062316, 2002.

[134] D. Babikov. J. Chem. Phys., 121:7577, 2004.

[135] D. DeMille. Phys. Rev. Lett., 88:067901, 2002.

[136] D.I. Schuster, L.S. Bishop, I.L. Chuang, D. DeMille, and R.J. Schoelkopf. arXiv:0908.2412v1 [physics.atom-ph], 2009.

Appendix A

Typical Experimental Parameter Values

$d_e\mathcal{E}_{\rm eff} = 2\pi \times 0.36$ mHz, transition energy between $m_F = +3/2$ and $m_F = -3/2$ states in ThF^+ if $d_e = 1.7$ x 10^{-29} e cm.

$d_{\rm mf} = +1.50$ a.u. $\approx 2\pi \times 2$ MHz/(V/cm), electric dipole moment of HfF^+ in the molecular rest frame.

$\mathcal{E}_{\rm rot} = 5$ V/cm, rotating electric field.

$\omega_{\rm rot} = 2\pi \times 100$ kHz, frequency of rotating electric field.

$\rm E_{rot} = 1800$ K, typical kinetic energy in rotational micromotion.

$r_{\rm rot} = 0.6$ mm, radius of circular micromotion.

$d_{\rm mf}\mathcal{E}_{\rm rot} = 2\pi \times 10$ MHz.

$(3/2)\gamma_{F=3/2}d_{\rm mf}\mathcal{E}_{\rm rot} = 2\pi \times 5$ MHz, Stark shift of $m_F = \pm 3/2$ states of $^3\Delta_1$ levels in rotating electric field.

$\omega_{\rm ef} = 2\pi \times 10$ kHz, Λ-doublet splitting between opposite parity $^3\Delta_1$ J=1 states.

$g_{F=3/2} = 0.03$, magnetic g-factor in $^3\Delta_1$ $m_F = \pm 3/2$ states.

$B_{\rm rot} = 70$ μG, rotating magnetic field.

$3g_F\mu_B\mathcal{B}_{\rm rot} = 2\pi \times 8$ Hz, Zeeman splitting between $m_F = +3/2$ and $m_F = -3/2$ states due to $\mathcal{B}_{\rm rot}$.

$\delta g_{F=3/2}/g_{F=3/2} \approx 3 \times 10^{-4}$, fractional difference of magnetic g-factor for upper and lower levels,.

$\Delta \approx 2\pi \times 2$ Hz, splitting at the avoided crossing between $m_F = +3/2$ and $m_F =$ -3/2 levels.

$\mathcal{B}_\perp = 25$ mG, anticipated scale of transverse magnetic field.

r = 0.5 cm, characteristic rms radius of trapped ion cloud.

T = 15 K, characteristic temperature of trapped cloud.

$\omega_i = 2\pi \times 1$ kHz, typical trap confining frequency.

$\mathcal{E}_z = 5$ mV/cm, typical axial electric field applied for confinement.

$\mathcal{E}_{\rm rf} = 75$ mV/cm, typical Paul trap electric field strength, at typical cloud radius.

$< \mathcal{E}_{\rm rf} > = 5$ mV/cm, typical radial confining electric field, averaged over one Paul cycle.

$\omega_{\rm rf} = 2\pi \times 15$ kHz, typical "rf freq" for Paul trap.

$\rm E_{rf} = 15$ K, typical kinetic energy in Paul micromotion.

$\rm E_{hf} = 2\pi \times 45$ MHz, hyperfine splitting between F = 1/2 and F = 3/2 states of $^3\Delta_1$ J=1 level.